Spring 1-1-2011

An Analysis of Hyperspectral Data of the Greenland Ice Sheet

Francesca Jeanne Lettang
University of Colorado at Boulder, flettang@gmail.com

AN ANALYSIS OF HYPERSPECTRAL DATA OF THE GREENLAND ICE SHEET.

by

FRANCESCA JEANNE LETTANG

B.S., California Polytechnic State University, 2009

A thesis submitted to the University of Colorado

Graduate School in partial fulfillment

of the requirement for the degree of

Master of Science

Department of Aerospace Engineering Sciences

2011

This thesis entitled:

An Analysis of Hyperspectral Data of the Greenland Ice Sheet

written by Francesca Jeanne Lettang

has been approved for the degree

Master of Science

Department of Aerospace Engineering Sciences

University of Colorado, Boulder

_____

Dr. William J. Emery

_____

Dr. James Maslanik

_____

Dr. Cora Randall

Date April 6, 2011

The final copy of this thesis has been examined by the signatories, and we find that both the content and the form meet acceptable presentation standards of scholarly work in the above mentioned discipline.

Abstract

Lettang, Francesca Jeanne (M.S., Aerospace Engineering Sciences)

An Analysis of Hyperspectral Data of the Greenland Ice Sheet

Thesis directed by Professor William J. Emery

Supraglacial melt ponds are common features of ice sheets and valuable parameters in the mass budget of the cryosphere. In addition, melt ponds are a useful proxy for monitoring global climate change as they are influenced by both the temperature of the surrounding ice and the incident radiation, which itself is influenced by the atmosphere. This document will describe an investigation of supraglacial melt ponds in a small region of the southwestern coast of the Greenland Ice Sheet, which was surveyed using an unmanned aerial vehicle in July of 2008. The data gathered during this expedition will be mined for melt ponds using Iterative Self-Organizing Data Analysis Technique, Adaptive Boosting, and Maximum Likelihood methods, and this information will be used to estimate the size and volume of the melt ponds using the known attenuation properties of water and the Beer-Lambert-Bouguer Law. Comparisons of the lake location data from UAV and satellite observations indicates that the results of the Adaptive Boosting and Maximum Likelihood algorithms are accurate to within 300 meters, or approximately ten pixels in the satellite data. The results of the lake depth analysis were inconclusive due to disagreements in the outcome when the calculations were made with different observing wavelengths and because of a lack of ground truth data. The most likely error source is the presence of suspended sediment in the lake,

floating ice crystals on the lake, either of which would affect the attenuation coefficient of the water, or settled sediment on the lake bottom, which would affect the lake bottom reflectivity. Finally, attempts to develop methods to detect drained supraglacial lakes led to the promising possibility that texture analysis or observation band ratio analysis could reveal drained lake locations without the advantage of change detection. However, texture analysis proved useful only in the UAV data, which has an extremely high spatial resolution, and no correlation between lake depth and observation band ratio was observed.

Acknowledgements

Several people were instrumental in the creation of this thesis. I would like to thank my advisor, Dr. Bill Emery, and thesis committee Dr. James Maslanik and Dr. Cora Randall for the expertise they lent me, Phillip Corcoran for providing the MUSCOX data, Casey Smith for his insight into the instrument used during the mission, and Ian Crocker for sharing his first hand knowledge of the mission. I would also like to thank my current and former office mates, Andrea, Eldad, Nathan, Trevor, Romain, Waqas, and Dan for convincing me to step away from my computer from time to time. Finally, I would like to thank my siblings, parents, and grandparents for their encouragement and support.

Contents

List of Tables

List of Figures

List of Acronyms

ASTER	Advanced Spaceborne Thermal Emission and Reflection Radiometer
BRDF	Bidirectional Reflectance Distribution Function
ENVI	Environment for Visualizing Images
ETM+	Enhanced Thematic Mapper Plus
IDL	Interactive Data Language
ISODATA	Iterative Self-Organizing Data Analysis Technique
MODIS	Moderate-Resolution Imaging Spectroradiometer
MUSCOX	Multisensor Cryospheric Observation Experiment
NOAA	National Oceanic & Atmospheric Administration
SZA	Solar Zenith Angle
UAV	Unmanned Aerial Vehicle

I. Introduction

One extremely important task in this day and age is learning about the impact of human activities on Earth's radiation budget and determining if it is a significant cause of global climate change. This is also a daunting undertaking, given the extreme complexity of the Earth system as a whole. Many satellites have been launched and many field campaigns waged in the attempt to answer this very question by gathering enough data to create an accurate model of the Earth system. Whether they have succeeded is a matter of debate, so the quest for more data and better models continues.

The Arctic Multisensor Cyrospheric Observation Experiment (MUSCOX) was one such enterprise. During July of 2008, a team of scientists and engineers traveled to western Greenland intending to image supraglacial lakes using an Airborne Imaging Spectrometer, made by Resonon, flying aboard a Manta UAV, made by BAE Systems, and compare the hyperspectral imagery to in situ depth measurements of the same lakes. Unfortunately, this mission demonstrated an important drawback of using supraglacial lakes as a method for measuring global climate change: by the time the mission began, the target lakes had already drained. As a result, while the drained lakes and an additional nearby filled lake were imaged using the UAV, no corresponding in situ depth measurements were taken. In spite of this, the MUSCOX data is an extremely valuable collection of information about the Greenland Ice Sheet in its area of study. In particular, its spatial resolution, which is on the order of tens of centimeters, is unachievable using current satellite technology

and may provide unprecedented accuracy in the estimation of the size and volume of glacial lakes. This feature will be used to its full advantage in the analysis to follow.

A. Supraglacial Lakes as a Proxy for Global Climate Change

The mechanism that forms glacial lakes is summarized in figure 1. Energy from the sun that is not attenuated by the atmosphere reaches Earth's surface, where it can be reflected or absorbed. When the surface is covered in ice, the majority of the light is reflected because ice has a high albedo. However, the energy that is not reflected is absorbed by the ice, which converts it into heat. If the temperature of the ice is raised to its melting point, then the ice begins to melt and the liquid water collects in melt ponds. Like ice, the liquid water absorbs or reflects the energy from the sun, but liquid water has a much lower albedo. Therefore, the water absorbs more energy than ice, becoming warmer itself and also transferring energy to the surrounding ice. The ice then melts faster, creating a positive feedback loop (*Perovich et. al.*, 2002).

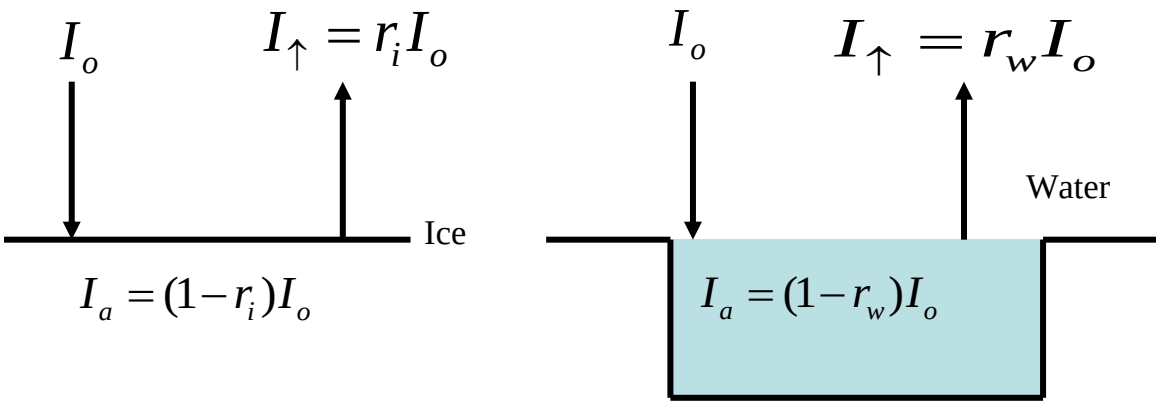

Figure 1: The radiative transfer of melt ponds.

Several experiments on sea ice have shown that the reflectivity of first year ice is 0.6 and the reflectivity of multiyear ice is 0.65, whereas the presence of melt ponds on the ice reduces the reflectivity in the area to 0.2 to 0.4 (*Eicken et. al.*, 2004). Though freshwater ice and liquid water have slightly different albedos, the trend of water reducing the average reflectivity in the area is the same. When ice and water absorb incoming radiation, their temperatures increase as given by equation (1) where ΔT is the change in temperature, Δt is the change in time, I_a is the absorbed radiation, c_p is the specific heat capacity, ρ is the density of the material, and d is the thickness of the ice-covered surface. The specific heat capacity of pure ice at -10°C is 2.02 J/g/K at standard atmospheric pressure, and the specific heat capacity of pure water at 0.01°C is 4.2170 J/g/K at 1 bar (*CRC Handbook of Chemistry and Physics*, 2010). This indicates that, if the same quantity in mass of ice and water absorb the same amount of heat, the temperature of the ice will increase faster. The ice will increase in temperature until it reaches its melting point, at which point it will begin to melt.

$$\frac{\Delta T}{\Delta t} = \frac{I_a}{c_p \rho d} \qquad (1)$$

Equation (2) gives the rate of melting of ice at its melting point. In this equation, Δd is the amount of melted ice, measured in terms of its depth, and ΔH_{fus} is the heat of fusion, which is 6.01 kJ/mol (333.61 kJ/kg) for water (*CRC Handbook of Chemistry and Physics*, 2010). The heat transfer of the ice-water system is completed by the second law of thermodynamics, which states that a system will seek equilibrium through energy transfer from the hot substance to the cold substance.

Therefore, energy transfer by convection and conduction will occur between the liquid water and the ice, attempting to equalize the temperature between the two substances, which will cause additional ice to melt.

$$\frac{\Delta d}{\Delta t} = \frac{I_a}{\Delta H_{fus} \rho} \qquad (2)$$

Supraglacial lakes are not a new feature of ice sheets, but changes in their frequency of occurrence and average volume can be used as an indicator of global climate change. Two features of global warming can influence the size of glacial lakes. The greenhouse effect, the mechanism by which long wave radiation is absorbed and re-emitted by aerosols in the atmosphere to back Earth's surface and the current leading theory for the cause of global warming, can increase supraglacial lakes because radiation from the sun can interact with the ice multiple times, causing the ice to absorb more heat each time. Secondly, increases in the mean ambient temperature of Earth can increase the frequency of occurrence of melt ponds because the ice sheets would have a higher temperature as well, reducing the amount of heat they need to absorb before reaching their melting point.

One of the mechanisms for draining melt ponds is for the water to find moulins, paths through cracks in the ice (*Box and Ski*, 2007). During one in situ experiment in Greenland in 2006, a supraglacial lake with a volume of 0.044 ± 0.01 km^3 was observed as it drained, most likely through a moulin, in approximately 1.4 hours (*Das et. al.*, 2008). During and after the drainage event, a nearby GPS station also observed changes in the height and velocity of the ice sheet in the area. Thus, the

presence of melt ponds has important implications in the mechanics of ice sheets, particularly the movement and dynamics of glaciers (*Zwally, et. al.*, 2002).

The flow of glaciers is at least partially defined by the friction between the ice and the underlying bedrock. According to *Boulton* (2006), ice can be modeled as a plastic solid with a yield strength of 100 kPa. In order for the ice to move, the average shear stress between the glacier and the bedrock, which is given in equation (3) for the case of strong coupling between the two surfaces, must be larger than 100 kPa. In this equation, τ is shear stress, ρ_i is the density of ice, g is the acceleration due to gravity, d is the ice thickness, and α is the slope of the surface beneath the ice.

$$\tau = \rho_i g d \sin\alpha \qquad (3)$$

The presence of liquid water between the ice and the bedrock can act as a lubricant and significantly reduce the friction between the two surfaces, meaning that forces sufficient to cause the glacier to deform can occur for ice with a lower density, height, and slope than would be required without the presence of water. As a result, water between the ice and the bedrock can cause glaciers to become more mobile and travel to low lying regions, including surrounding seas and oceans, more quickly, which in turn affects the salinity and temperature of the oceans and can change the water budget of the planet.

Georgiou et. al. (2009), undertook a study of melt ponds in images of a small region of the Greenland ice shelf observed by the Advanced Spaceborne Thermal Emission and Reflection Radiometer (ASTER) instrument and correlated the volume of supraglacial lakes to the number of positive degree days, days when the

temperature is above 0°C, preceding the observation. They discovered that lake volume increases slowly from positive degree days 10 to 80 due to the contributions of snow melt, then lake volume increases more rapidly until approximately positive degree day 125 due to ice melt. After positive degree day 125 the lakes begin to drain. This study shows that the water budget of the Greenland Ice Sheet is strongly affected by the temperatures in the region.

An additional study by *Sundal et. al.* (2009), using MODIS (Moderate-resolution Imaging Spectroradiometer) data of the Greenland Ice Sheet in the years 2003, 2005, 2006, and 2007, produced lake and runoff areas in three separate regions. This study indicates a high level of variability in supraglacial lake area by day and year and that supraglacial lakes form later in the melt season in locations at higher elevations and latitudes, and that years with large lake areas tend to have high temperatures during the melt season.

Of course, the presence of melt water at the interface between glacial ice and the bedrock is not a recent development: glaciers and ice sheets at various locations have frequently been influenced by liquid water from both subglacial and supraglacial sources. The important question is if the frequency and volume of liquid water on ice sheets has increased and, if it has, is that increase a response to human activity and what are the long term consequences to the ice sheets.

B. Summary of Analysis

This document will describe the analysis of very high spatial resolution hyperspectral data of a small area of the Greenland Ice Sheet in the visible and near

infrared regime, which was gathered by an unmanned aerial vehicle in July of 2008. The data will be mined for the locations and depths of supraglacial lakes with the objective of determining the volume of the lakes. Several methods of separating lake pixels from ice pixels will be used. Additionally, the data will be searched for evidence of drained supraglacial lakes with the intention of developing a method to determine the size of these former lakes. For verification, the above analysis will also be performed on Landsat 7 ETM+ and the results compared.

This analysis will be beneficial because the prevalence of glacial lakes is a useful proxy for global climate change and an important parameter in the study of the mass balance of ice sheets. Developing a method of very accurately determining the volume of filled glacial lakes will be beneficial because glacial lakes play an important role in the water budget of ice sheets and the Earth system as a whole. Developing a method of detecting drained glacial lakes will be valuable because lakes often have short and unpredictable life spans, meaning that it is possible for satellite observations, such as Landsat with its 16 day repeat period, to miss them, especially if clouds interfere with an observation. Learning the unique properties of drained lake locations will allow inferences to be made about glacial lakes for longer periods of time, reducing the probability that a lake will be missed.

Figure 2 shows a map of the study area.

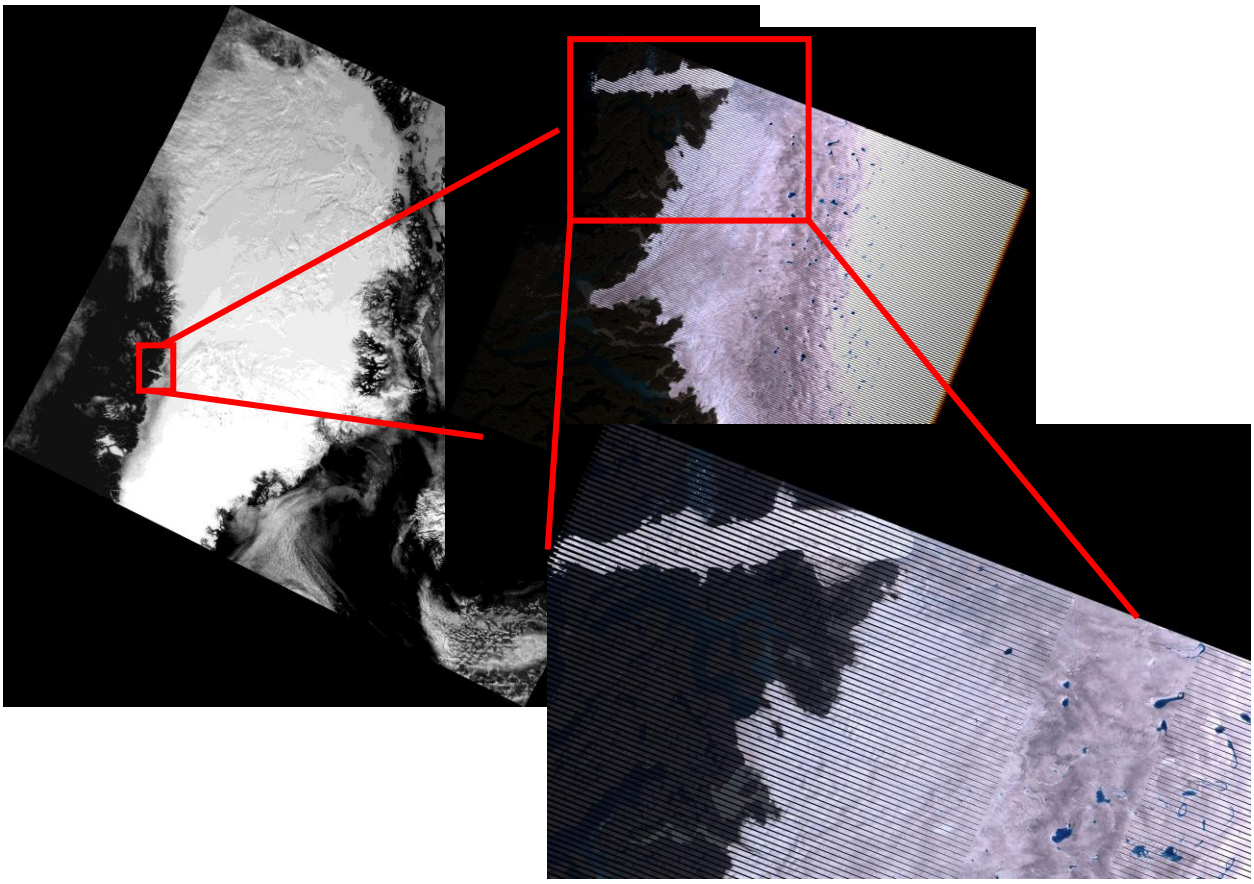

Figure 2: Study area.

II. Data Specification

Two data sources will be used for this analysis. The primary data source is the MUSCOX mission. The secondary data source is the Landsat 7 ETM+ (Enhanced Thematic Mapper Plus). The Landsat data sets will be chosen to coincide in time and location with the MUSCOX data sets.

A. MUSCOX

The MUSCOX mission took place in July 2008, with the first mission flown on July 9 and the last on July 24. In all, 26 data sets were collected, as summarized in table 23 in the appendix. The data is uncalibrated and will be thought of in units of

photon counts. Spectral data will be given in units of normalized photon counts.

One target the MUSCOX mission is the Ilulissat Airport, on the south west coast of Greenland, where the UAV took off and landed. It was imaged during tests of the UAV and spectrometer hardware. These images will be used to verify the performance of the ground type detection software. An example of a runway image in true color is given in figure 3. This image corresponds to data set 26 as given in table 23.

Figure 3: True color MUSCOX image of the runway at Ilulissat Airport.

The ice and supraglacial lake images are located near Davis Strait. Figure 4 shows an example of an ice image, including a portion of a supraglacial lake, in true color. This image corresponds to data set nine in table 23.

Figure 4: True color MUSCOX image of ice and a supraglacial lake.

The spectrometer used on the MUSCOX mission imaged the targets in 60 spectral bands in the visible and near infrared as summarized in table 24 in the appendix. It uses a pushbroom scanning technique with 320 cross track pixels for a total angular field of view of 12.2^{o}. Of course, the size of the ground pixel varies based on the altitude and orientation of the UAV.

The MUSCOX data was provided by Phillip Corcoran from BAE Systems, who was involved in the MUSCOX project.

B. Landsat 7 ETM+

Landsat 7 was launched on April 15, 1999 and has been gathering science data ever since. Table 1 gives the important features of the Landsat 7 orbit and the ETM+ sensor summarized from *NASA: Landsat 7 Science Data User's Handbook* (2009).

Table 1: Important features of Landsat 7 operations.

Orbit Altitude	705
Orbit Type	Sun Synchronous
Inclination	98.2^{o}
Orbital Period	98.89 minutes
Ground Track Repeat	16 days
Scan Method	Whisk Broom
Swath Width	185 km

The bands of the ETM+ sensor and the spatial resolution of each band are given in table 2, summarized from *Scaramuzza et. al.* (2004). Only the 30 meter resolution bands will be used in this analysis.

Table 2: Landsat 7 ETM+ bands.

Channel	Spectral Range	Spatial Resolution (m^2)
1	441-514 nm	30
2	519-601 nm	30
3	631-692 nm	30
4	772-898 nm	30
5	1.547-1.748 μm	30
6	10.31-12.36 μm	60
7	2.064-2.346 μm	30
8	515-896 nm	15

Landsat 7 imaged the same area of Greenland approximately concurrently with the MUSCOX experiment, creating images such as that shown in figure 5. The inlaid regions are the areas which were imaged by the UAV. The outflow region pictured is the Jakobshavn Isbrae, a glacier which empties into Disko Bay. In this image, red corresponds to the 631 to 692 nm band, green corresponds to the 519 to 601 nm band, and blue corresponds to the 441 to 514 nm band. The image was taken on July 19, 2008.

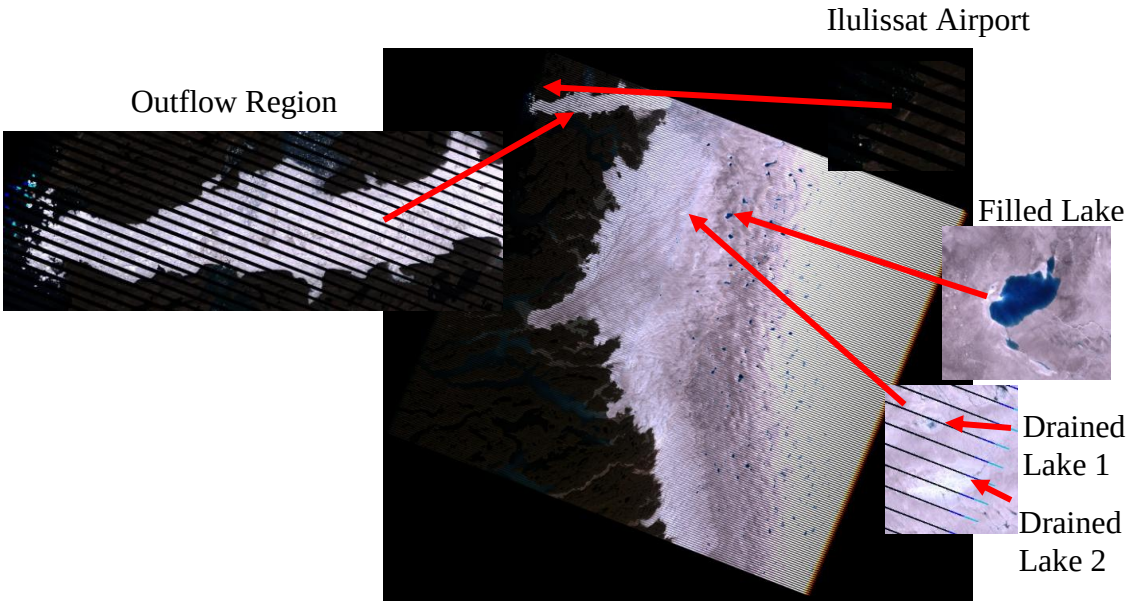

Figure 5: Sample Landsat imagery from July 19, 2008.

Two Landsat data sets will be used for the majority of this analysis. The first was taken on July 3, 2008 and will be referred to as Landsat 1. The second data set was taken on July 19, 2008 and will be referred to as Landsat 2.

The Landsat data was retrieved using the Earth Explorer online tool provided by the United States Geological Survey. As with the MUSCOX data, the Landsat data is provided in uncalibrated photon counts and will be presented here in normalized photon counts.

III. Method

This research has four objectives:

1. Use various methods to distinguish supraglacial lakes from the surrounding ice.
2. Determine the volume of the supraglacial lakes.
3. Determine a method to distinguish drained supraglacial lakes from the

surrounding ice.

4. Use the information gathered from the previous three objectives to draw conclusions about the status of the Greenland Ice Sheet.

The primary data source for this analysis will be the MUSCOX mission. Data gathered by LANDSAT 7 will be used for comparison and long-term analysis. The primary analysis tools will be the Interactive Data Language (IDL) and the Environment for Visualizing Images (ENVI). Both software tools were created by ITT Visual Information Solutions.

A. Preprocessing

Before analysis can begin, several factors which influence the data must be taken into account or corrected. These factors include the spatial location of the data, atmospheric attenuation, solar zenith angle, refraction of light, observation angle, and spatial resolution. Conveniently, the MUSCOX data already has location data associated with each pixel, so geolocation is not necessary. Similarly, the Landsat data has position information associated with it that is intended to be extracted using ENVI, so determining the locations of the Landsat data is a simple matter. These locations will be assumed to be accurate for the purposes of this analysis.

1. Atmospheric Attenuation

In order to make corrections for atmospheric attenuation, knowledge of the properties of the atmosphere and the path the radiation takes through the atmosphere is required in order to apply Beer's law to each channel of data. However, atmospheric attenuation at the visible and near infrared wavelengths used by

MUSCOX and Landsat is small, as discussed in *Petty* (2006) chapter 7. As a result, within a single MUSCOX image or a small area of a Landsat image, it is valid to assume that any pixel to pixel differences in the atmospheric attenuation are negligible. Therefore, no corrections for attenuation though the atmosphere will be applied.

Clouds are one exception to this rule. The MUSCOX observation height is below the level of most clouds, avoiding the issue, but if a visual inspection of the Landsat data reveals clouds in the area of interest, then that image will not be used for analysis. Another exception is aerosols in the atmosphere. Aerosols can vary greatly in concentration and no in situ measurements were taken at the time of the MUSCOX mission. However, in the Arctic regions, the influence of aerosols is generally small (*Stroeve, et. al.*, 1997). Additionally, like the properties of the rest of the atmosphere, the effect of aerosols can be assumed not to vary widely within a small area in a single observation. Data on the concentration of aerosols in the area at the times of interest may have been observed by another satellite, but the application of that data is left to a future investigator.

2. Solar Zenith Angle

Similar to the effects of atmospheric attenuation, solar zenith angle does not change significantly during the short observation times for each data set. However, knowledge of the solar zenith angle is still required, particularly for calculations of water depth, because path length through the water is dependent upon the angle of the radiation when it reaches the water. This is especially important in high latitude

locations such as Greenland, where the sun is always low in the sky.

Solar zenith angle (SZA) was calculated for each observation using the Solar Calculation tools created by the Earth System Research Laboratory Global Monitoring Division, a part of the National Oceanic & Atmospheric Administration (NOAA), which is in turn based on equations in *Astronomical Algorithms* by Jean Meeus.[1] Table 3 shows these solar zenith and azimuth angles, which include corrections for refraction through the atmosphere. Since these angles do not change significantly in the course of a single observation, the solar angles were calculated for the time and location in the middle of each image. For MUSCOX, the center location is the average of the latitudes and longitudes of each pixel in the image, since the maneuvers of the UAV could potentially cause the pixels which were in the middle of the observation temporally to be placed near the edge of the image spatially. Solar elevation and azimuth information was included in the Landsat metadata, so it was not recalculated using the method described except for verification purposes.

[1] http://www.esrl.noaa.gov/gmd/grad/solcalc/calcdetails.html

Table 3: Sun location of all observations.

Instrument	Observation Number	Center Date and Time (UT)	Center Location	Sun Zenith Angle (degrees)	Sun Azimuth Angle (degrees)
MUSCOX	1	7/9/2008 00:03:59.02	69°14’33.66” N 51°3’30.05” W	81.23	313.04
MUSCOX	2	7/9/2008 00:05:22.58	69°14’33.39” N 51°3’30.29” W	81.34	313.44
MUSCOX	3	7/9/2008 00:07:29.03	69°14’33.37” N 51°3’30.73” W	81.45	313.83
MUSCOX	4	7/9/2008 00:09:14.75	69°14’32.98” N 51°3’31.02” W	81.56	314.22
MUSCOX	5	7/9/2008 00:10:57.99	69°14’35.14” N 51°3’40.10” W	81.67	314.61
MUSCOX	6	7/16/2008 01:08:08.97	69°9’31.67” N 50°51’20.16” W	85.82	327.31
MUSCOX	7	7/16/2008 01:16:15.46	69°9’31.91” N 50°51’20.06” W	86.19	329.17
MUSCOX	8	7/17/2008 02:58:29.55	68°44’49.11” N 49°31’43.72” W	89.50	353.99
MUSCOX	9	7/17/2008 03:09:29.94	68°43’6.90” N 49°2’3.68” W	89.61	357.02
MUSCOX	10	7/17/2008 03:12:39.51	68°42’29.33” N 49°1’21.61” W	89.63	357.76
MUSCOX	11	7/18/2008 01:41:50.52	68°42’35.54” N 49°1’31.00” W	88.15	336.64
MUSCOX	12	7/18/2008 02:22:51.47	68°45’7.50” N 49°30’59.68” W	89.15	345.68
MUSCOX	13	7/18/2008 02:24:41.97	68°43’28.84” N 49°30’59.99” W	89.21	346.11
MUSCOX	14	7/18/2008 02:33:48.18	68°43’42.20” N 49°31’57.43” W	89.37	348.21
MUSCOX	15	7/18/2008 02:34:08.76	68°43’24.15” N 49°31’57.11” W	89.38	348.29
MUSCOX	16	7/19/2008 02:05:09.06	68°42’35.33” N 49°1’31.36” W	88.99	341.99
MUSCOX	17	7/19/2008 02:08:34.57	68°42’29.47” N 49°1’57.45” W	89.08	342.78
MUSCOX	18	7/19/2008 02:56:49.54	68°42’59.71” N 49°30’13.49” W	89.81	353.58
MUSCOX	19	7/19/2008 03:00:02.04	68°43’20.46” N 49°30’1.00” W	89.83	354.33

Table 3 continued: Sun location of all observations.

Instrument	Observation Number	Center Date and Time (UT)	Center Location	Sun Zenith Angle (degrees)	Sun Azimuth Angle (degrees)
MUSCOX	20	7/19/2008 03:02:58.54	68°43'39.68" N 49°30'14.26" W	89.85	355.01
MUSCOX	21	7/19/2008 03:09:07.54	68°44'19.68" N 49°30'16.12" W	89.88	356.45
MUSCOX	22	7/19/2008 03:12:17.04	68°44'49.50" N 49°30'2.56" W	89.89	357.19
MUSCOX	23	7/19/2008 03:15:17.04	68°44'59.69" N 49°30'16.87" W	89.89	357.89
MUSCOX	24	7/19/2008 04:25:42.92	69°14'41.97" N 51°3'45.48" W	89.02	12.88
MUSCOX	25	7/19/2008 04:26:41.41	69°14'26.21" N 51°3'45.46" W	89.00	13.10
MUSCOX	26	7/19/2008 04:28:27.64	69°14'28.77" N 51°3'39.37" W	88.97	13.52
Landsat	1	7/3/2008 11:44:22.28	68°16'53.04" N 49°48'39.24" W	45.79	167.36
Landsat	2	7/19/2008 11:44:10.34	68°17'42.36" N 49°47'20.76" W	48.03	166.97

Night is a relative term when applied to locations at extreme latitudes, such as Greenland, during the summer, because the sun does not set. However, it is important to note that all of the MUSCOX observations took place when the sun was extremely low in the sky and the Landsat observations took place closer to mid day. Scheduling the MUSCOX missions for this time of day has the benefit of avoiding the possibility of imaging sun glint from the ice and water and also prevented the UAV from imaging its own shadow, and may have been a logistical necessity because of allowed flight plans. However, this attribute of the data also causes problems for lake depth calculations, as will be discussed shortly.

3. Refraction

The refraction of light through the air/water interface will also influence the path the light takes through the water. Snell's law, shown as equation (4), gives the angle of transmitted light through an interface, θ_t, for any angle of incident light, θ_o. In this equation, N_1 is the real index of refraction of the initial medium and N_2 is the index of refraction of the medium that the light moves into. Thus, in the case of light passing from air to water, the index of refraction of air would be N_1 and the index of refraction of water would be N_2. The angles are measured relative to a line which is perpendicular to the interface.

$$\frac{\sin\theta_t}{N_1} = \frac{\sin\theta_o}{N_2} \qquad (4)$$

The index of refraction of air is approximately 1 for all wavelengths and the index of refraction of water is approximately 1.33 for all wavelengths (*Petty*, 2006). Figure 5 shows the angle of transmittance for angles of incidence between 0 and 90^o for the air to water and water to air interfaces. As figure 6 indicates, Snell's law is invalid for the water to air interface for angles of incidence above 48.75^o. If light reaches a water to air interface at an angle of incidence above 48.75^o, all of the light will be reflected inside the water instead of changing mediums to the air.

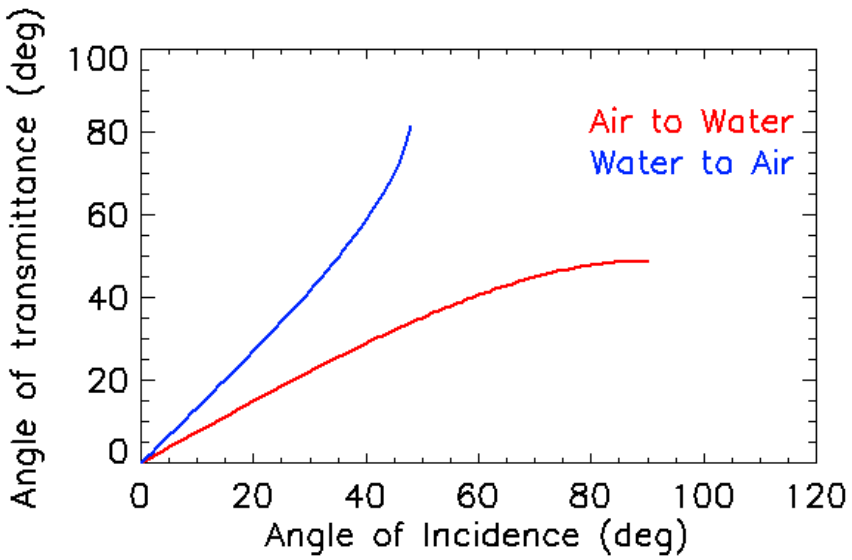

Figure 6: Refraction of light through air to water and water to air interfaces.

Using this information, figure 7 shows the path the light takes from the sun, through a glacial lake, to the Landsat satellite. This analysis assumes that the lake bottom is a Lambertian reflector and that for each pixel the satellite receives only light from that pixel which is reflected directly upward, meaning that refraction does not occur on the light's journey from the lake bottom to the satellite. Though it is not strictly true, the Lambertian reflector assumption is necessary because no information about the angle of the lake bottom compared to the horizontal is available. With the benefit of multiple channels of data it may be possible to partially separate decreases in signal due to attenuation by the water from decreases in signal due to anisotropic reflection by the lake bottom, but that effort will not be undertaken in this analysis.

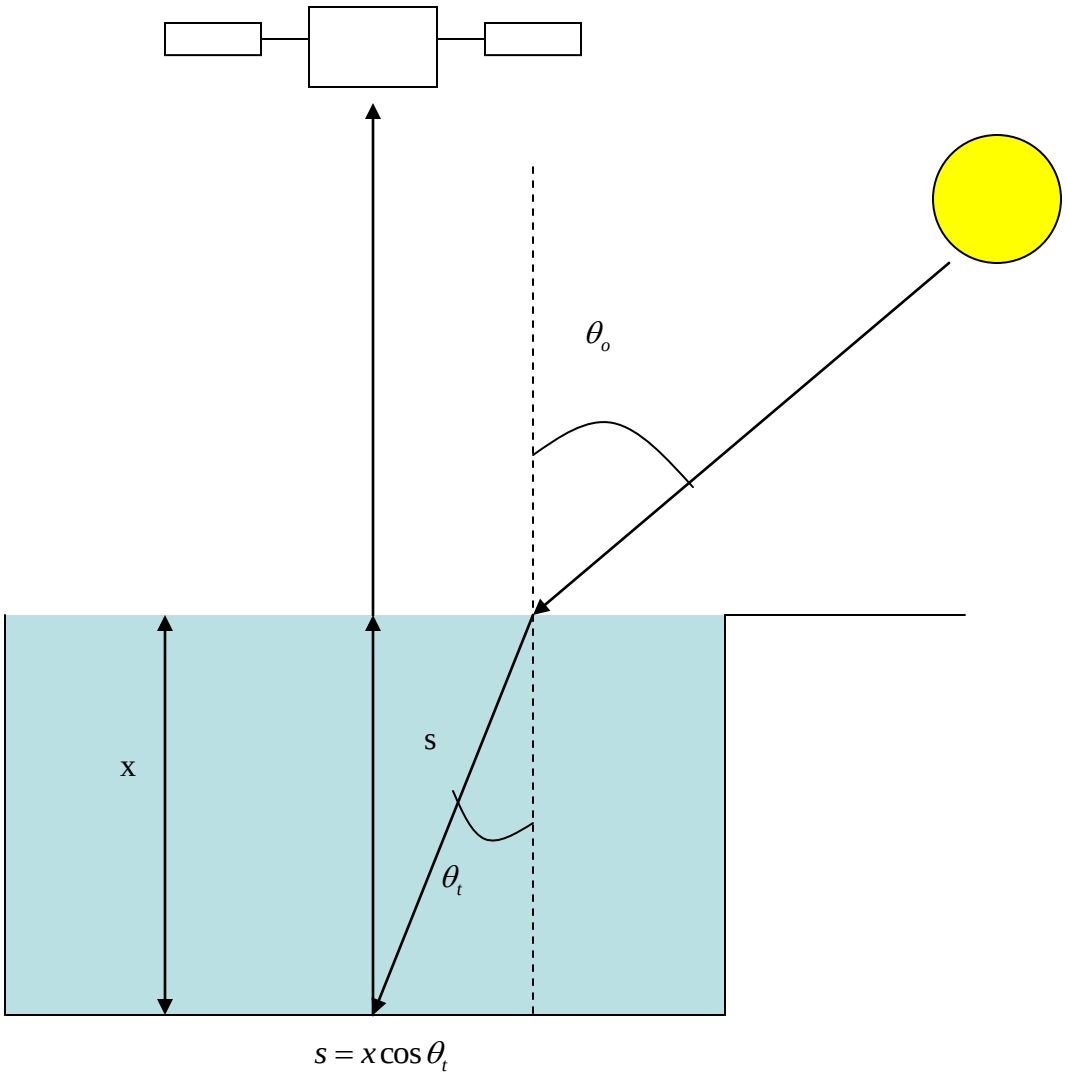

Figure 7: Refraction for Landsat observations.

Refraction in the case of the MUSCOX observations is complicated by the fact that the height of the UAV is low enough that it is not valid to assume that the light which reaches the instrument has a 0^o incidence angle at the water to air interface. Instead, the path is dependent upon the view angle of the UAV, as summarized for a single pixel in figure 8. As with the Landsat observations, the lake bottom will be assumed to be a Lambertian reflector.

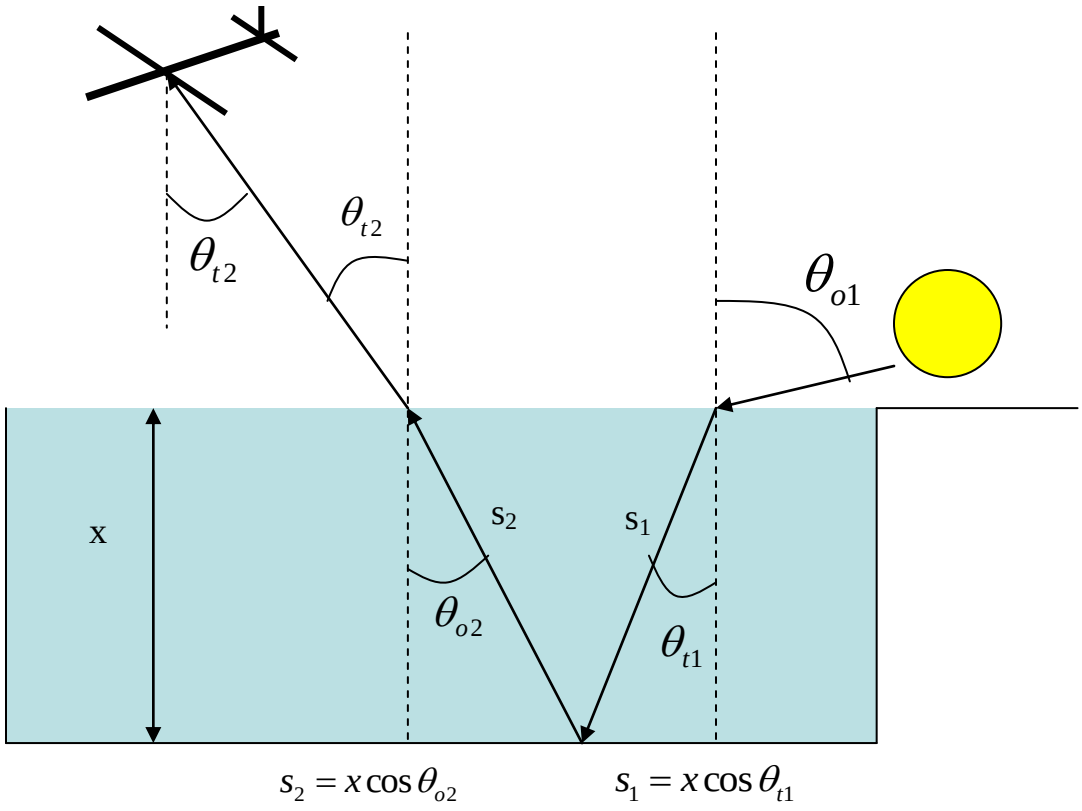

Figure 8: Refraction for MUSCOX observations.

4. Spatial Resolution

The spatial resolution of each pixel in the Landsat data is well known because the instrument has known optical characteristics and orbits at a nearly constant altitude. However, in the MUSCOX data, spatial resolution varies based on the height of the aircraft and its roll and pitch angles. Additionally, the angular resolution of the instrument was unknown and so had to be inferred based on measurements of the runway. In situ measurements placed the width of the center stripe of the runway at 46 cm. As shown in figure 9, which gives first several lines of data of data set 1, a runway image, this region is seven pixels wide, meaning that these ground pixel have

widths of 6.57 cm.

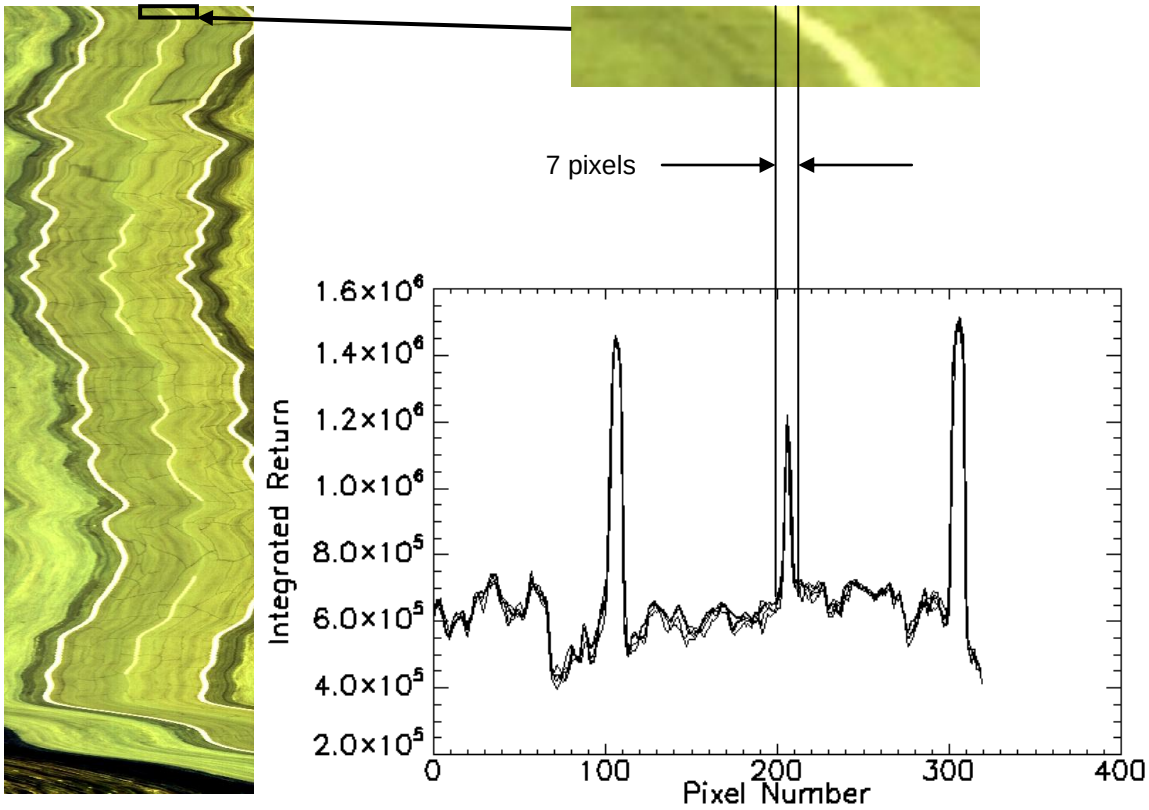

Figure 9: Derivation of the MUSCOX spatial resolution.

At the time of this observation the height of the UAV was 265.03 m, the roll angle was -1.736^{o}, and the pitch angle was 4.647^{o}. Additionally, since the center stripe pixels are not at the center of the image, there is a slight angular offset of 1.82 degrees from nadir in the cross track direction. Figure 10 shows the direction of each of these angular offsets.

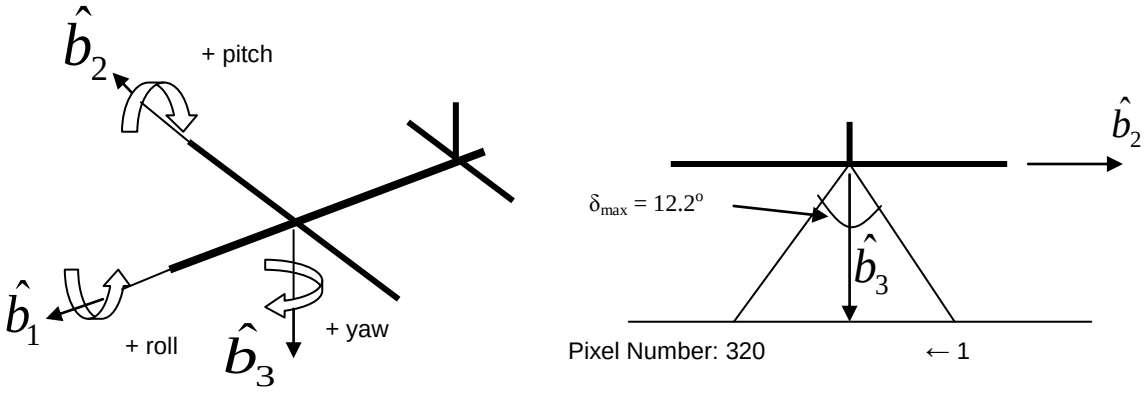

Figure 10: Angular offsets of the UAV.

The range from the imager to the ground pixel is calculated using equation (5), where δ is the angular offset of each pixel, φ is the roll angle, and θ is the pitch angle. The yaw angle of the aircraft is not included in this formulation because yaw does not influence the range from the instrument to the ground pixels. Equation (5) gives the unit $\hat{b}_3$ vector in terms of a coordinate frame which is attached to the UAV but does not rotate. Multiplying this vector by a factor which makes the nadir component equal the height of the UAV then calculating the magnitude of the vector gives the slant range to the pixel. Thus, the range from the UAV to the stripe pixels in the image above is 266.405 meters.

$$\vec{z} = \begin{bmatrix} 1 & 0 & 0 \\ 0 & \cos(\phi+\delta) & \sin(\phi+\delta) \\ 0 & -\sin(\phi+\delta) & \cos(\phi+\delta) \end{bmatrix} \begin{bmatrix} \cos\theta & 0 & -\sin\theta \\ 0 & 1 & 0 \\ \sin\theta & 0 & \cos\theta \end{bmatrix} \begin{bmatrix} 0 \\ 0 \\ 1 \end{bmatrix} \qquad (5)$$

The final step is to apply equation (6), where X' is the size of the ground pixel, s is the path length, and θ_r is the angular resolution. Using the 6.57 cm width of the ground pixels and the path length found above reveals that the angular resolution of

each pixel is 0.007067^{o}.

$$X' = 2s\tan\theta_r \qquad (6)$$

5. Anisotropic Reflection

All ground types will be assumed as Lambertian reflectors for the majority of the analysis. This is necessary because ground type categorization begins without a priori information about the locations of the ground types in the image. Additionally, this study is not attempting to derive the albedo of the various ground types, only to distinguish them from one another. Therefore, the bidirectional reflectance distribution functions (BRDFs) of the likely ground types will only be considered if ambiguities in the categorization results are discovered or for correction factors in the calculation of the depth of supraglacial lakes.

Painter and Dozier (2006) published their observations of the BRDF of snow at two observation wavelengths and snow grain sizes using an Automated Spectro-Goniometer on February 23, 2001 at Mammoth Lakes, CA. Their study indicates that the BRDF of snow depends strongly upon the observation wavelength and the grain size of the snow, and that snow reflects light most strongly in the forward direction, but a non-negligible amount of light is also reflected in a fashion which is better described as Lambertian.

Greuell and de Ruyter de Wildt (1999) performed reflectivity measurements on melting glacier ice in Switzerland. Their observations indicate that the BRDF of melting glacier ice is much more specular than the BRDF of snow.

According to *Petty* (2006), smooth water experiences specular reflection. Thus, unless the surface of the water is disturbed by wind, the angle of the reflected light will equal the angle of the incident light. Another consideration is the reflectivity of water at grazing angles, which is particularly important considering the extreme solar zenith angles of the MUSCOX observations. The reflectivity of an interface at various angles of incidence is given by the Fresnel relations, reproduced as equations (7), (8), and (9) for the case of unpolarized light, such as the sun, where r is the reflectivity. These equations are reproduced from *Petty* (2006).

$$m = \frac{N_2}{N_1} \tag{7}$$

$$\cos\theta_t = \sqrt{1 - \left(\frac{\sin\theta_o}{m}\right)^2} \tag{8}$$

$$r = \frac{1}{2}\left[\left|\frac{\cos\theta_t - m\cos\theta_o}{\cos\theta_t + m\cos\theta_o}\right|^2 + \left|\frac{\cos\theta_o - m\cos\theta_t}{\cos\theta_o + m\cos\theta_t}\right|^2\right] \tag{9}$$

The results of the Fresnel relations for the air/water interface are given in figure 11.

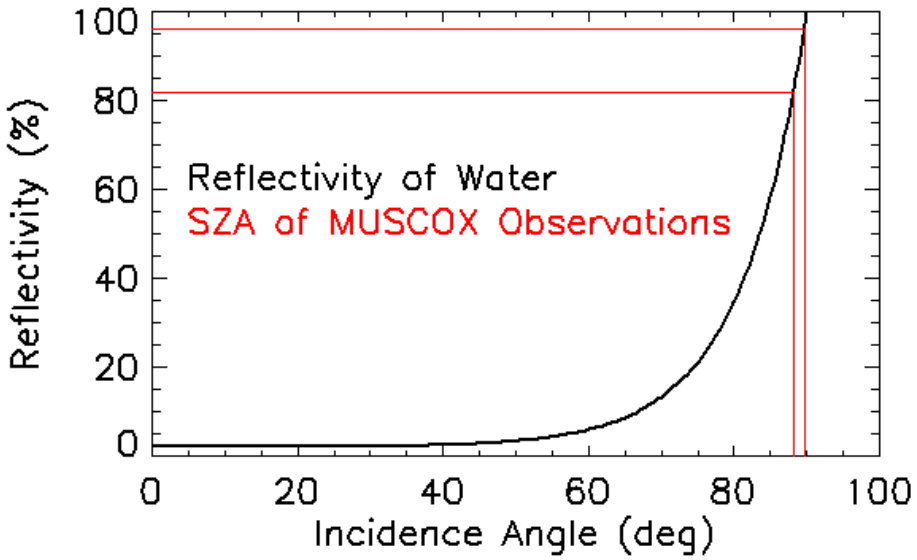

Figure 11: Fresnel relations of the air/water interface with the reflectivity for the MUSCOX observations highlighted.

Figure 11 highlights a significant issue with the MUSCOX lake observations if any attempt to determine the water depth is to be made: depending on the observation, only 3.99 to 18.32% of the light which is incident on water will actually penetrate the surface. In this situation, the levels of light which reach the water after being scattered at least once by the atmosphere are no longer negligible compared to the amount of light which is not scattered and must be taken into account in order to obtain an accurate result. No methods of accounting for the effects of skylight in the calculation of water depth could be located, so instead the calculations of water depth in the MUSCOX data will assume that all light originates from a zenith angle of zero degrees which the knowledge that the resulting depths will be slightly too large.

6. Summary of Preprocessing and Sources of Error

Table 4 summarizes the preprocessing undertaken for this analysis and the remaining sources of uncertainty.

Table 4: Error sources and likely impacts.

Consideration	Mitigation	Remaining Error Impact
Atmospheric Attenuation	Ignored	Negligible
Aerosol Attenuation	Ignored	Negligible
Sun Location	Calculated for each data set	Pixel to pixel differences ignored, but are negligible
Refraction	Calculated for each pixel	Negligible differences due to index of refraction varying as a function of wavelength
Spatial Resolution	Calculated for each pixel	Possible errors due to ground height differences from datum
Reflection	BRDFs for likely ground types located	Uncertainties possible due to variable snow grain size, not melting, or mismatch of solar zenith angles with observations
Scattering by Atmosphere	Ignored	Likely overestimation of lake depth in MUSCOX observations
Difference between height of observed locations and datum	Ignored	Possible large under and over estimation of pixel area

B. Detection of Supraglacial Lakes

Figure 12 shows a filled supraglacial lake as imaged by Landsat 7 and MUSCOX.

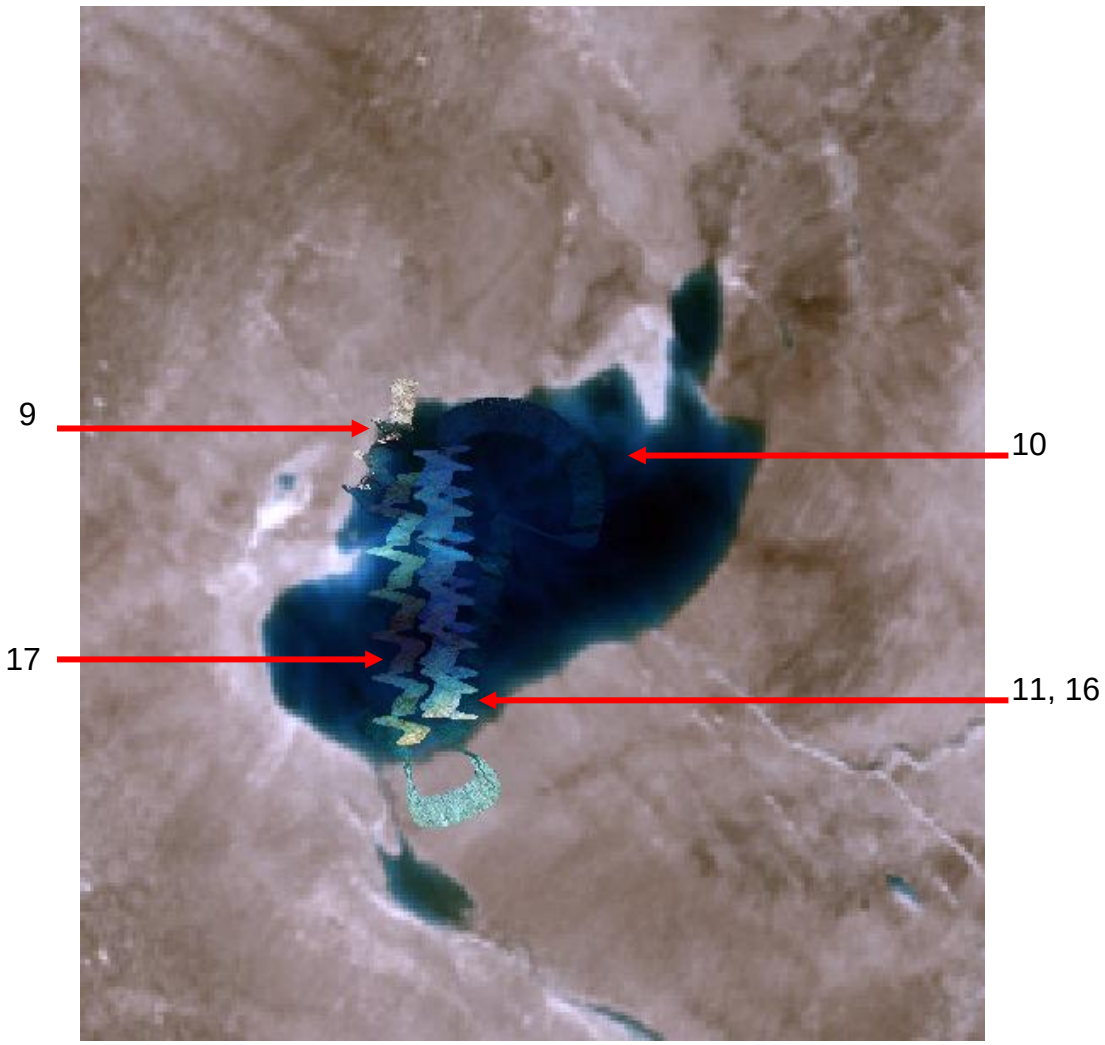

Figure 12: Mosaic of MUSCOX and Landsat 7 filled lake data.

While it is a simple matter for a person to look at an image such as figure 12 and immediately recognize some of the features in it, training a computer to do the same is a much more involved task. Several algorithms and methods have been developed to determine ground types in remote sensing data, all of which start with the reflective properties of the possible ground types. This project will use three methods of ground type detection and compare the results.

1. Spectral Signatures

All ground classification methods require some a priori knowledge of the spectral properties of the ground types in the image. The data used in this project is most likely to contain the following ground types: snow, ice, dirt, clear water, dirty water, and dirty ice. The spectral signatures of snow, ice, water, and inorganic materials have been measured as described in *Satterwhite et. al.* (2003). All of the measurements in this study were taken by viewing samples in the nadir direction. The results of this study indicate that glacial ice is highly reflective in the visible wavelengths, but dirty ice looses its reflectivity. Fresh and old snow are more reflective and have more constant reflectivity over visible wavelengths. Meanwhile, inorganic materials such as scree left by avalanches or glaciers are less reflective and that reflectivity is highly dependent on the amount of sediment present. The reflectivity of water is, of course, entirely dependent upon the water depth and the Fresnel equations discussed above.

2. ISODATA

Iterative Self-Organizing Data Analysis Technique, or ISODATA, is an unsupervised iterative clustering algorithm, which attempts to create subsets of data based on sample means (*Tou and Gonzalez*, 1974). In brief, the ISODATA algorithm takes the samples of a data set and arranges each sample according to its proximity to a number of cluster centers. In the case of remotely sensed image data, each pixel is an individual sample and the term "proximity" refers to the similarity of the magnitude of each spectral band to the cluster center, not to the locations of the

pixels. By comparing the mean and standard deviation of the distance of each sample from its cluster center to threshold parameters, the number of cluster centers and "locations" of the cluster centers in the spectral domain are adjusted. The procedure is repeated for a set number of iterations and results in a number of subsets of the original data set, grouped by similar spectral characteristics. Figure 13 shows an operational flow chart of the ISODATA algorithm. For this analysis, the ISODATA tool built in to ENVI will be used.

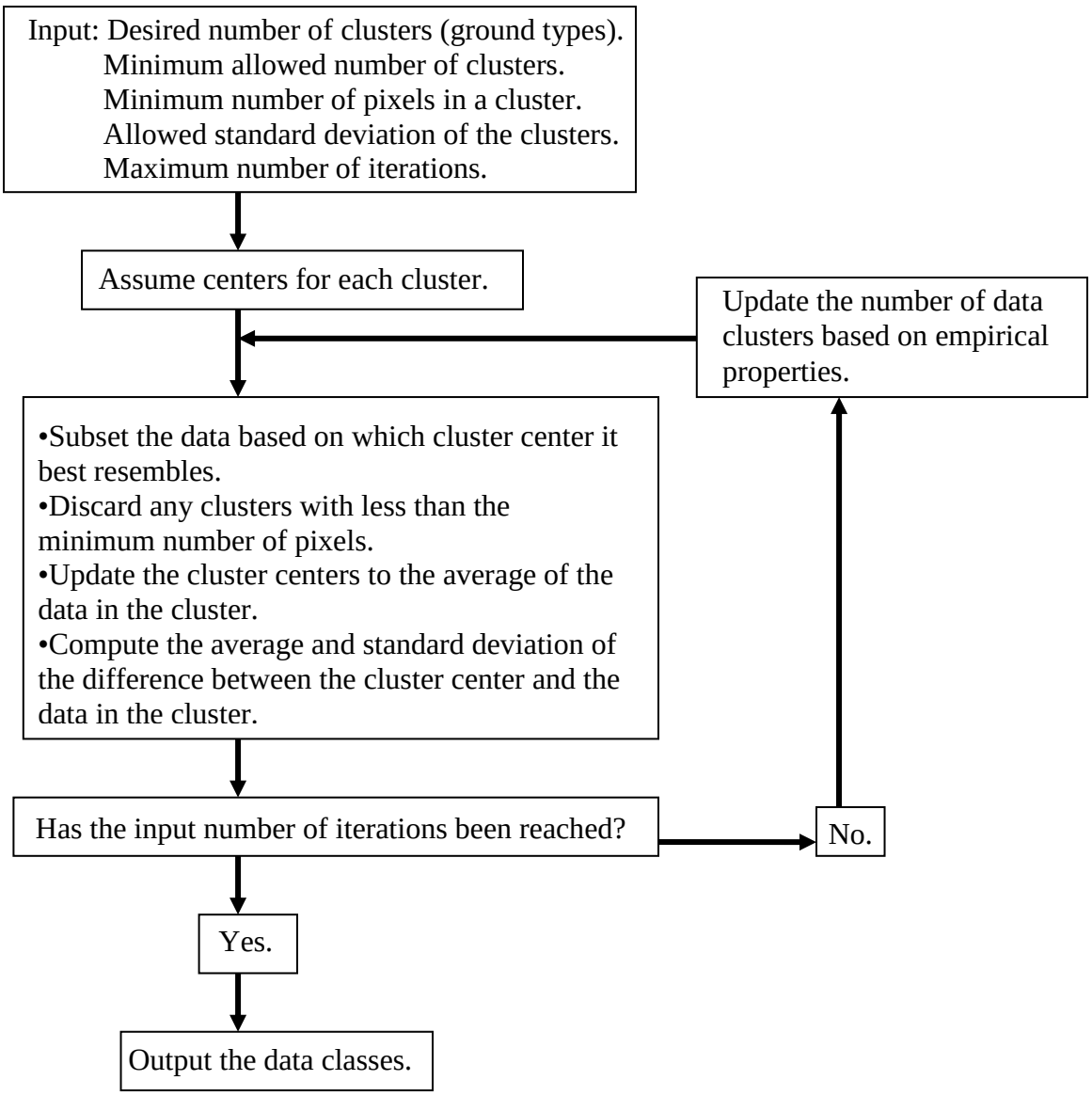

Figure 13: Flow chart of the ISODATA algorithm.

Figure 14 shows the results of applying the ISODATA algorithm to a runway image, size by side with the original image in grayscale. The colors in this image correspond to the five different features that the algorithm isolated.

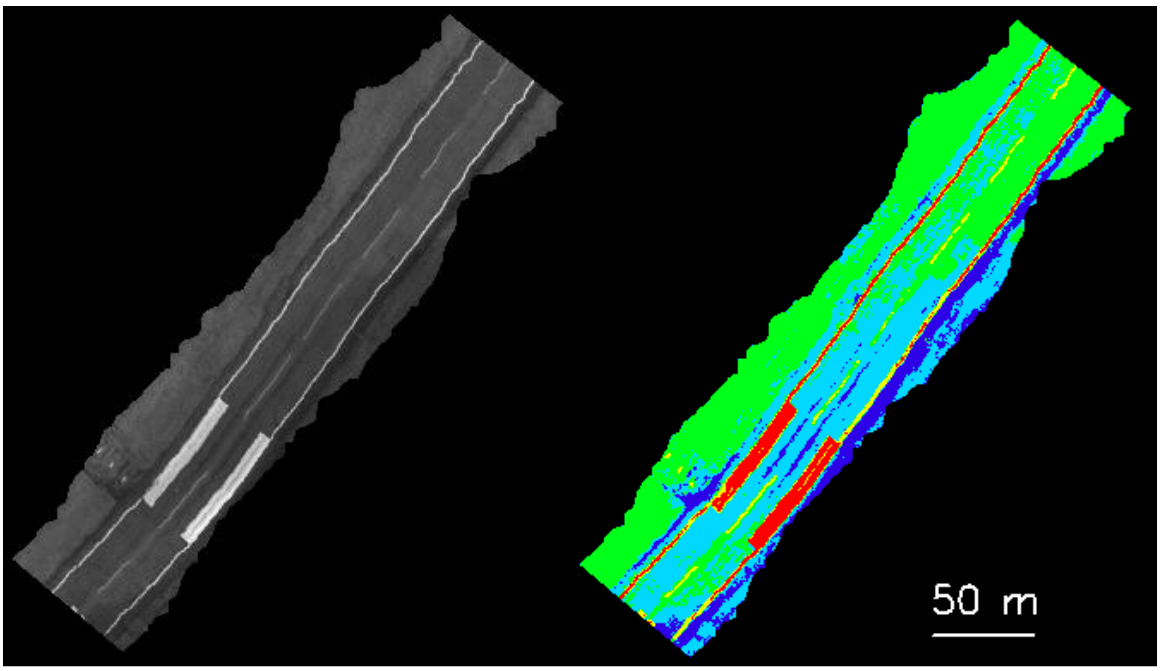

Figure 14: Results of ISODATA on a runway image.

By comparing the two runway images, it is possible to infer that the red and yellow pixels are paint, though the locations in yellow are slightly darker than the areas in red. The light blue pixels are primarily runway. The green pixels are the slightly darker area beside the runway, although some of the darker regions of the runway are also labeled in this same data class. The dark blue pixels are runway or areas in shadow. The average returns from each data class are given in figure 15.

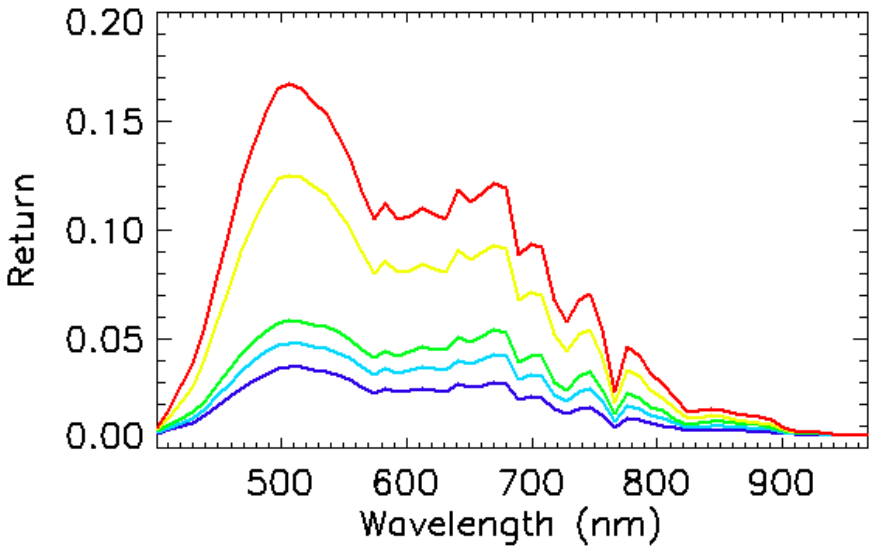

Figure 15: Spectral returns from each data class isolated by ISODATA.

As figure 15 indicates, the data classes labeled in red and yellow have very similar signatures, as do the data classes labeled in green, light blue, and dark blue. With additional tuning of the input parameters to the ISODATA algorithm, it may be possible to refine the classifications and make them more accurate. The quantitative results from the ISODATA algorithm are given in table 5.

Table 5: Results of ISODATA.

Class	Number of Pixels	Percent of Total	Likely Ground Type	Total Number of Pixels for Ground Type	Percent of Total
Red	19285	3.18%	Paint	36989	6.11%
Yellow	17704	2.92%			
Light Blue	254988	42.09%	Runway	361170	59.62%
Dark Blue	106182	17.53%			
Green	207601	34.27%	Beside Runway	207601	34.27%

3. Adaptive Boosting

Adaptive boosting is a machine-learning algorithm, which combines many weak classifiers into a single strong classifier. The algorithm is described in detail in *Freund and Schapire* (1997) and *Nishii and Eguchi* (2008). In general terms, when applied to remote sensing, adaptive boosting is a supervised classifier which makes a series of guesses about the ground type of the pixels in the image based on given parameters, in this case, the intensity of the light in each channel. After each guess, the algorithm re-calculates the weight of the input pixels based on whether or not the weak classifier was correct in its guess. Pixels which are incorrectly classified are given higher weights for the next iteration. After several iterations, the algorithm combines all of its guesses into a single strong classifier, which is more accurate than any of the weak classifiers alone. Figure 16 shows an operational flow chart of the adaptive boosting algorithm summarized from *Freund and Schapire* (1997). For this analysis, the adaptive boosting algorithm was hand coded using IDL.

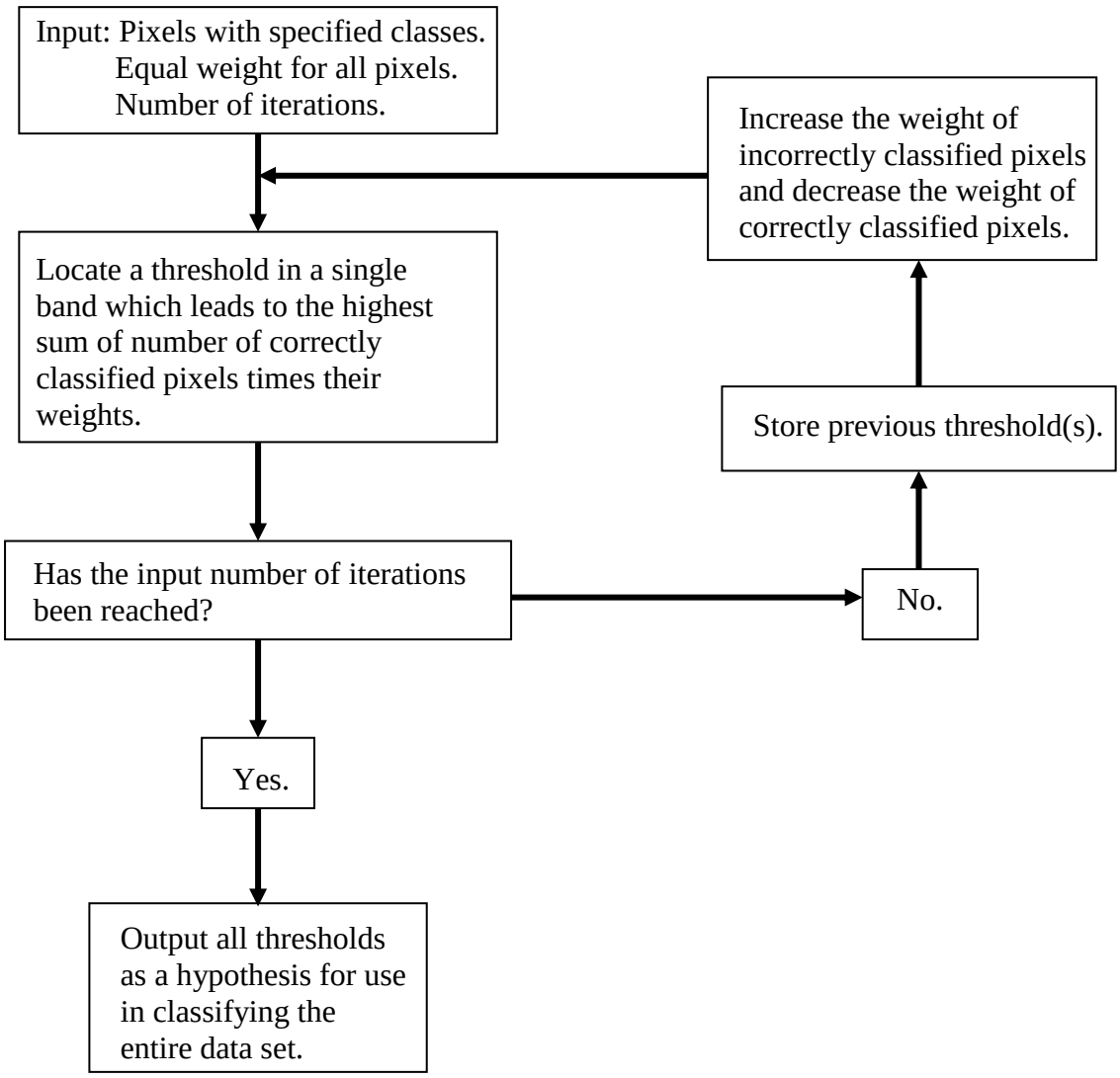

Figure 16: Flow chart of the adaptive boosting algorithm.

The results of adaptive boosting on the simple case of separating the painted stripes on a runway from the asphalt and surrounding ground are given in figure 17. The first image shows the original image and highlights the training data given to the adaptive boosting algorithm. In all three images, red indicates the stripes painted on the runway and blue indicates the runway surface and surrounding ground. The second image shows the spectral information from the training data, averaged by

pixel, and the threshold results from the adaptive boosting algorithm. In this case, the algorithm determined that all of the training data could be accurately classified by using a single threshold: all pixels with normalized returns higher than 0.065 in the 468.41 nm band are paint pixels, the rest are not paint pixels.

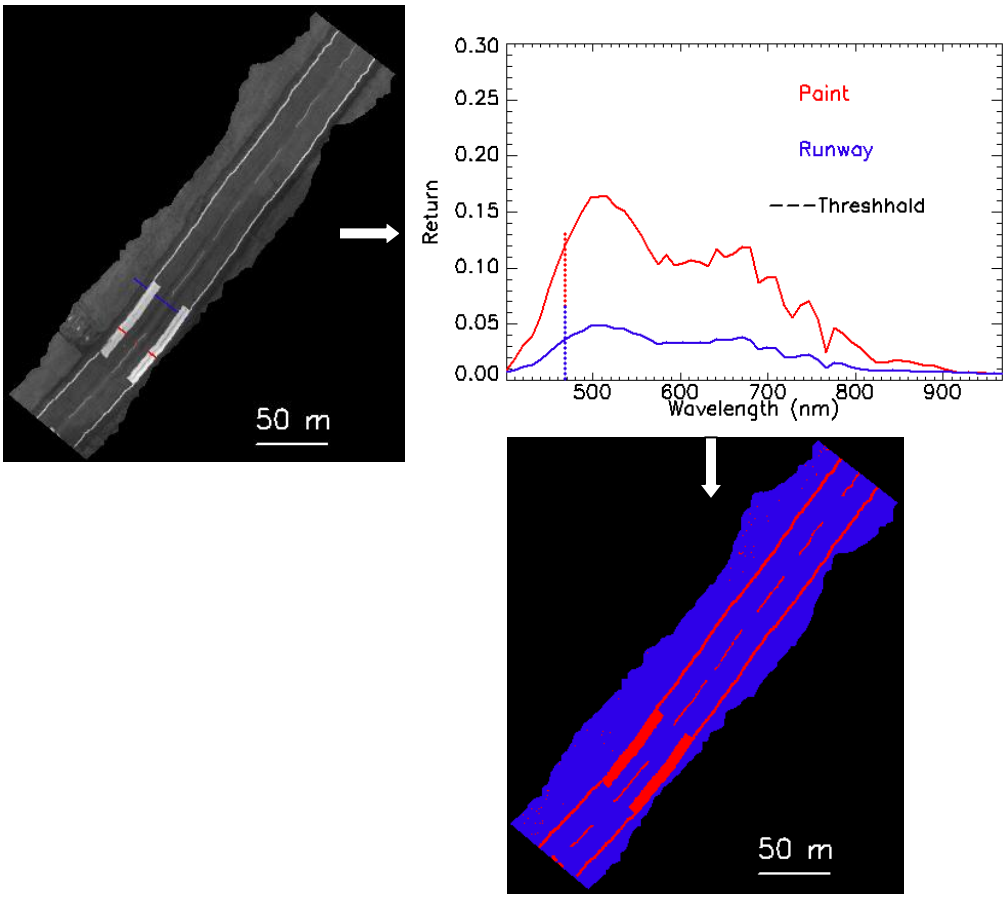

Figure 17: Results of adaptive boosting on a runway image.

The next step in the analysis of the runway image using adaptive boosting is to take the pixels that were determined not to contain paint and separate them based on whether they are runway or ground beside the runway. Figure 18 shows the results of this effort.

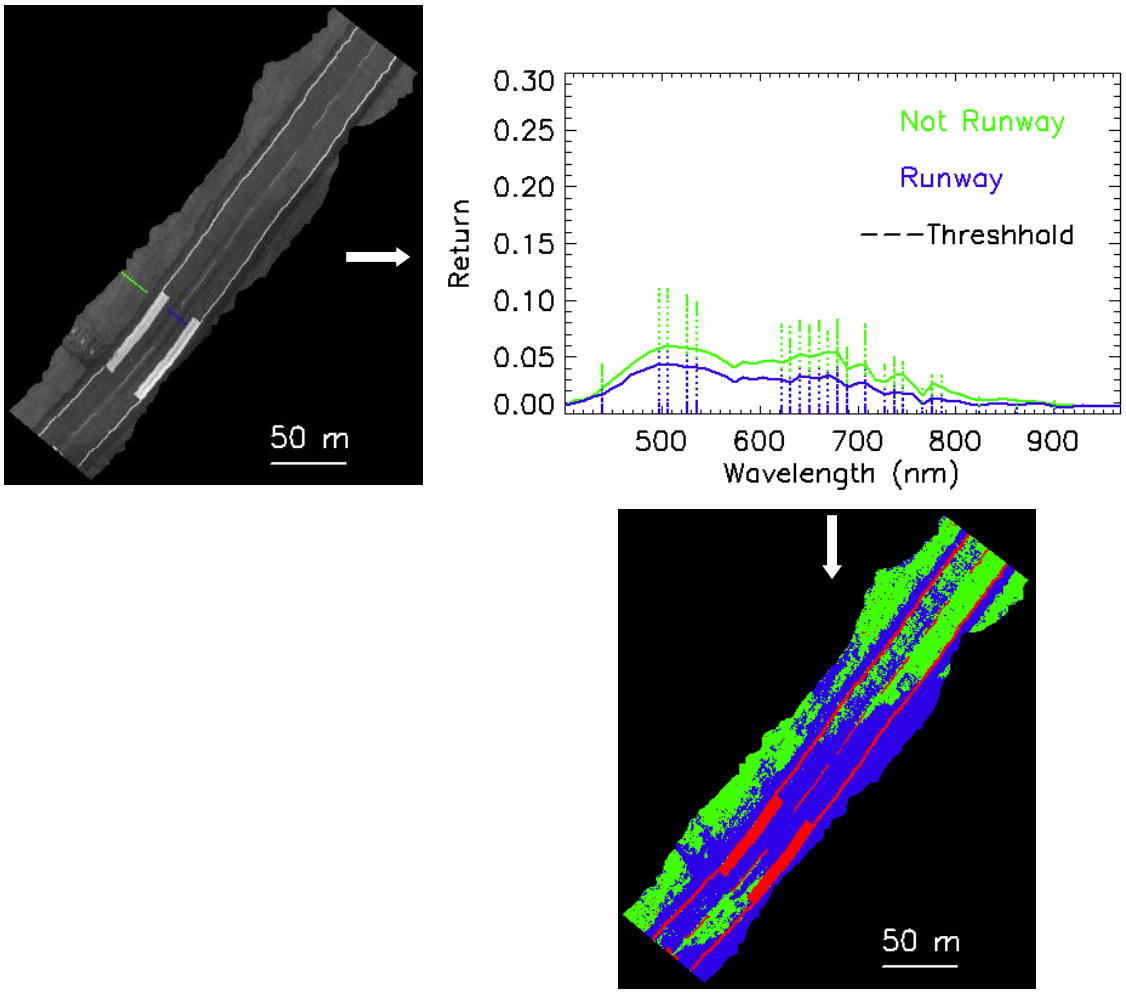

Figure 18: Adaptive boosting to separate road from dirt on a runway image.

A qualitative analysis of these results indicates that adaptive boosting was not completely successful at separating runway pixels from not runway pixels, though it appears to be approximately as accurate as the ISODATA method. Also, like the ISODATA method, these results could be improved by making adjustments to the inputs to the algorithm. In the case of adaptive boosting, the best adjustment would be to choose pixels that were previously misclassified when the model was applied

and ensure that they are used as teaching data for the creation of the model. The number of pixels assigned to each class using adaptive boosting is given in table 6.

Table 6: Results of adaptive boosting.

Class	Number of Pixels	Percent of Total Area
Paint	37209	6.14%
Runway	225727	37.26%
Not Runway	342824	56.59%

4. Maximum Likelihood

The maximum likelihood algorithm is a supervised classification algorithm. It is described in full in *Richards and Jia* (2006). In short, the maximum likelihood algorithm classifies data by calculating the probability that an unclassified pixel belongs to one of the training data sets by using equation (10). In this equation, g_j is called the discriminant function, j is the data class, $\vec{x}$ is the spectral data of each individual pixel in vector form, $p(\omega_j)$ is the a priori probability that a pixel belongs to class ω_j, Σ_j is the covariance matrix of the data in class j, and m_j is the average of each band of data in class j. The discriminate function for each pixel is calculated for each data class and the pixels are classified with the class which gives the largest discriminant function. For this analysis, the maximum likelihood facilities built into ENVI will be used.

$$g_j(\vec{x}) = \ln p(\omega_j) - \frac{1}{2}\ln\left|\Sigma_j\right| - \frac{1}{2}(\vec{x} - m_j)^t \Sigma_j^{-1}(\vec{x} - m_j) \qquad (10)$$

Figure 19 gives an operational flow chart of the maximum likelihood algorithm.

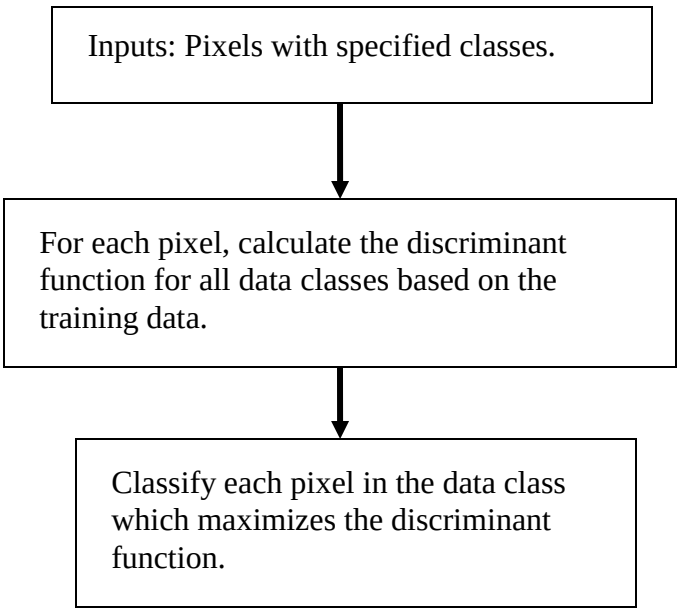

Figure 19: Flow chart of the maximum likelihood algorithm.

Figure 20 shows the results of applying maximum likelihood to the runway image.

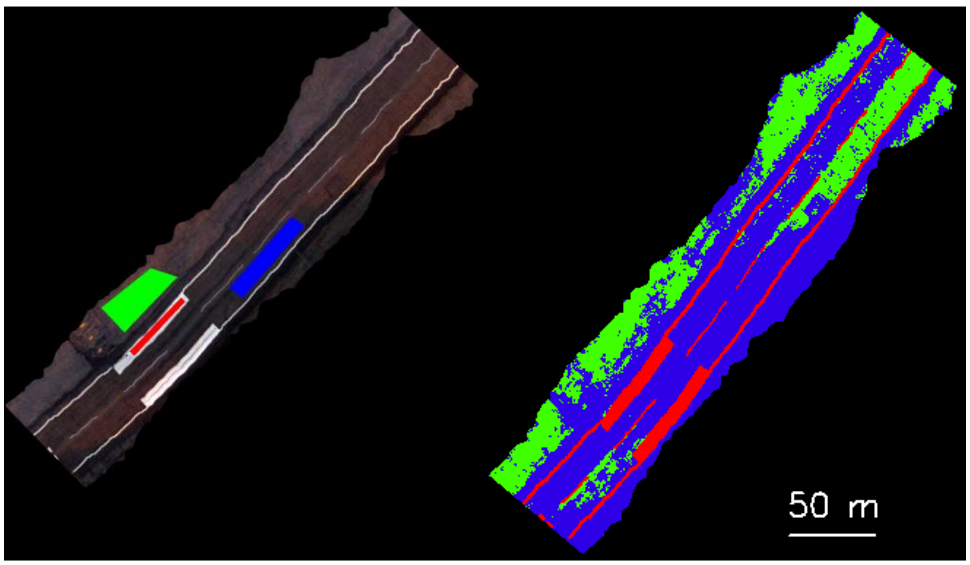

Figure 20: Results of classification of a runway image with maximum likelihood.

Like ISODATA and adaptive boosting, the maximum likelihood method does not accurately distinguish the runway from the ground beside the runway. Table 7 summarizes the results.

Table 7: Results of maximum likelihood.

Class	Number of Pixels	Percent of Total Area
Paint	37805	6.24%
Runway	288990	47.71%
Not Runway	278965	46.05%

Maximum likelihood does have one significant advantage over the other two methods: it is a simple matter to add more pixels to the training data. The maximum likelihood algorithm with additional training data was used to create figure 21. Comparison of figures 20 and 21 shows that additional training data is important in the successful use of the maximum likelihood algorithm.

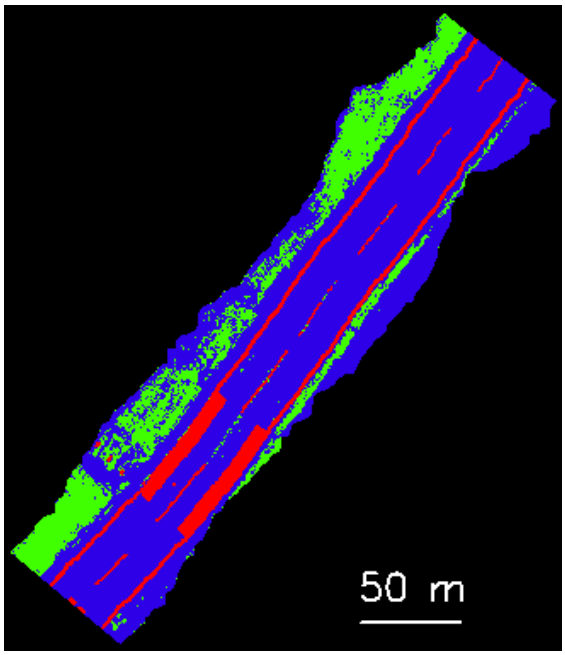

Figure 21: Runway classification using maximum likelihood with additional training data.

The quantitative results of using maximum likelihood with additional training data are given in table 8.

Table 8: Results of maximum likelihood with additional training data.

Class	Number of Pixels	Percent of Total Area
Paint	36858	6.08%
Runway	321744	53.11%
Not Runway	247158	40.80%

5. Comparison of Classification Algorithms

All three algorithms give similar estimates in their classifications of the different ground types. This is particularly significant in the separation of runway pixels from pixels which are not runway. Figure 22 gives another view of the runway, as taken by a video camera onboard the UAV during the flights. From this image, it is immediately clear that the material beside the runway is not very different from the material that makes up the runway itself; they may even be identical. It is possible that the boundaries of the runway are only obvious because the stripes painted on the runway make them so. It is therefore impressive that all three algorithms, which only examine the data on a pixel by pixel basis, were able to make some distinction between the two very similar ground types.

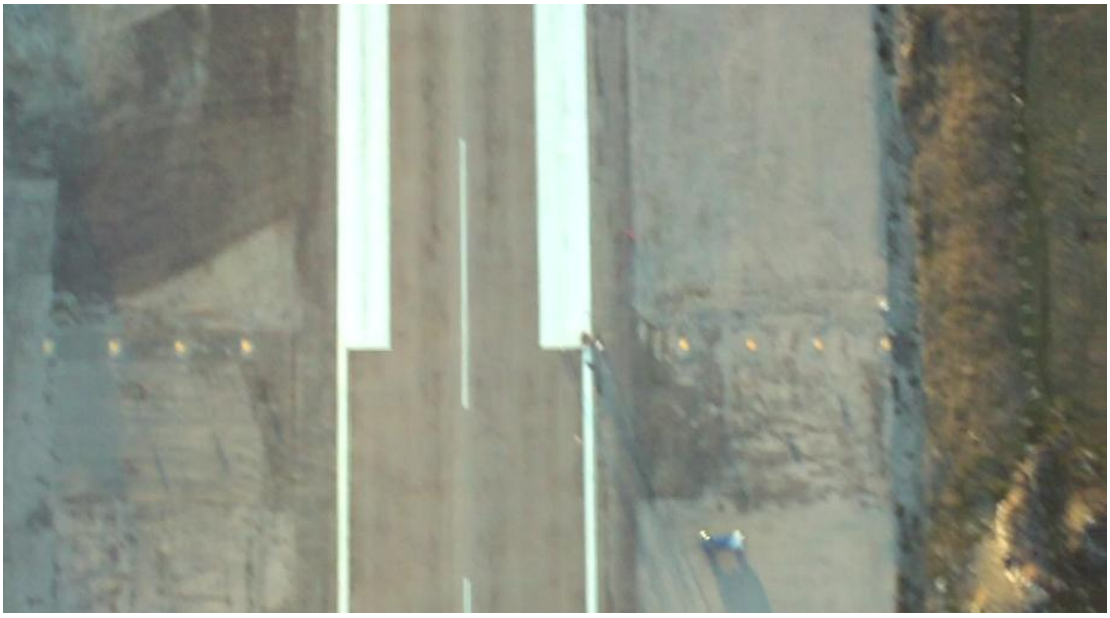

Figure 22: The runway as imaged by an onboard video camera.

For comparison, figure 23 shows a low fidelity hand analysis of the same runway image, estimating the percent of the image occupied by the three ground types.

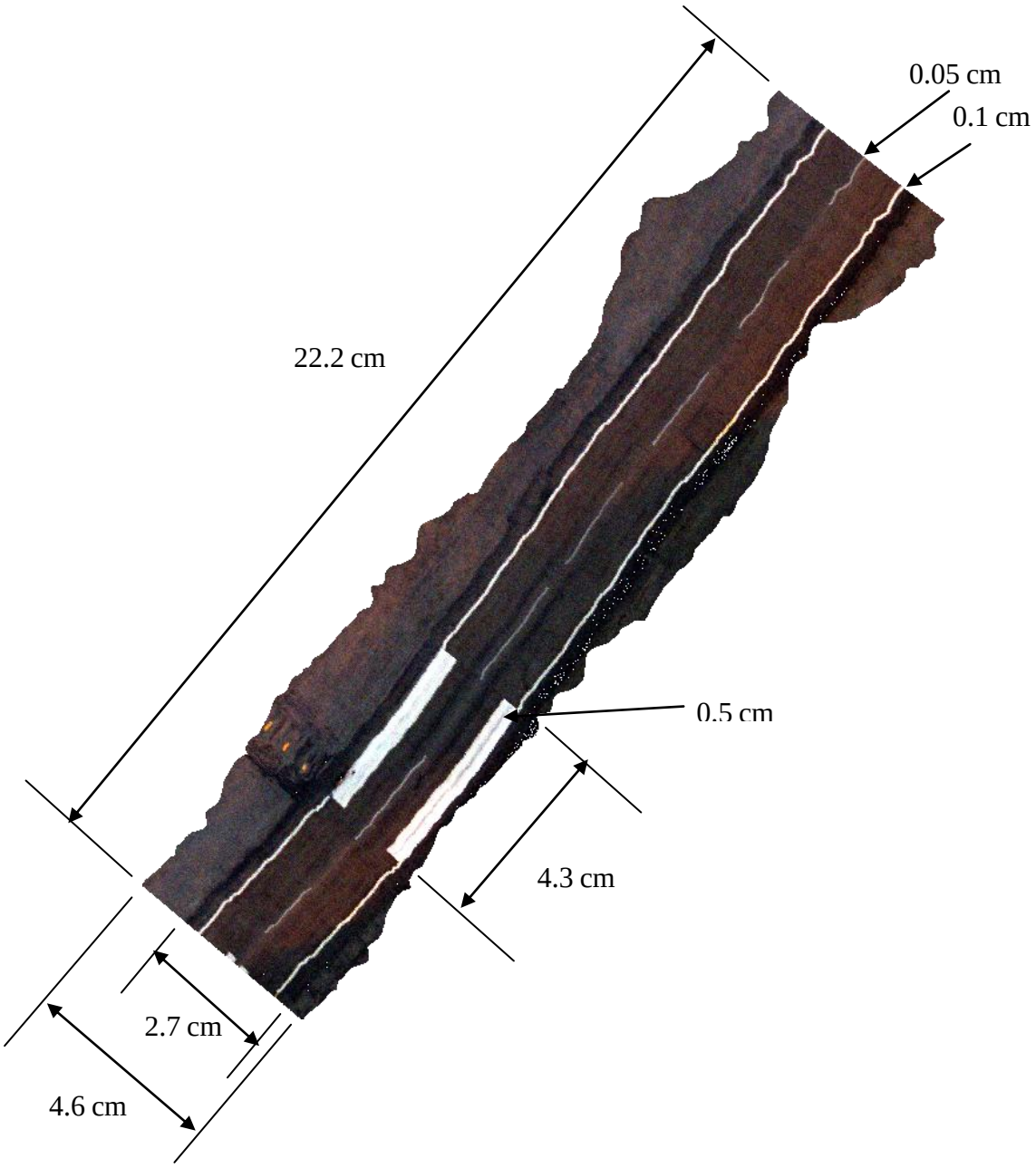

Figure 23: Hand analysis of areas in the runway image.

Table 9 compares the results of the hand analysis to the three ground categorization algorithms.

Table 9: Comparison of hand analysis of the runway image to the ground classification algorithm results.

Ground Type	Percent of Total Area			
	Hand Analysis	ISODATA	Adaptive Boosting	Maximum Likelihood
Paint	7.12 %	6.11 %	6.14 %	6.08 %
Runway	51.58 %	59.62 %	37.26 %	53.11 %
Not Runway	41.30 %	34.27 %	56.59 %	40.80 %

Consistent with the qualitative analysis above, these results indicate that all three ground classification results were very accurate in separating paint pixels from non-paint pixels. They were less successful in their attempts to separate the runway pixels to the pixels which were beside the runway, though maximum likelihood was the most accurate.

C. Determination of Lake Depth

Determination of lake depth will make use of two similar methods. The first is the Beer-Lambert-Bouguer law, commonly shortened to Beer's law, which is given as equation (11) where x is the depth of the water, t is the transmittance, I(x) is the intensity at depth x, I_o is the intensity at the surface, λ is the wavelength of the light, and n_i is the imaginary component of the index of refraction of the water, which is a function of wavelength.

$$t(x) = \frac{I(x)}{I_o} = \exp\left[\frac{-4\pi n_i x}{\lambda}\right] \qquad (11)$$

The basic radiative transfer model used for lake depth measurements is shown in figure 24. The equations in this figure must be adjusted if the path of light through

the water to the instrument contains any slant angle.

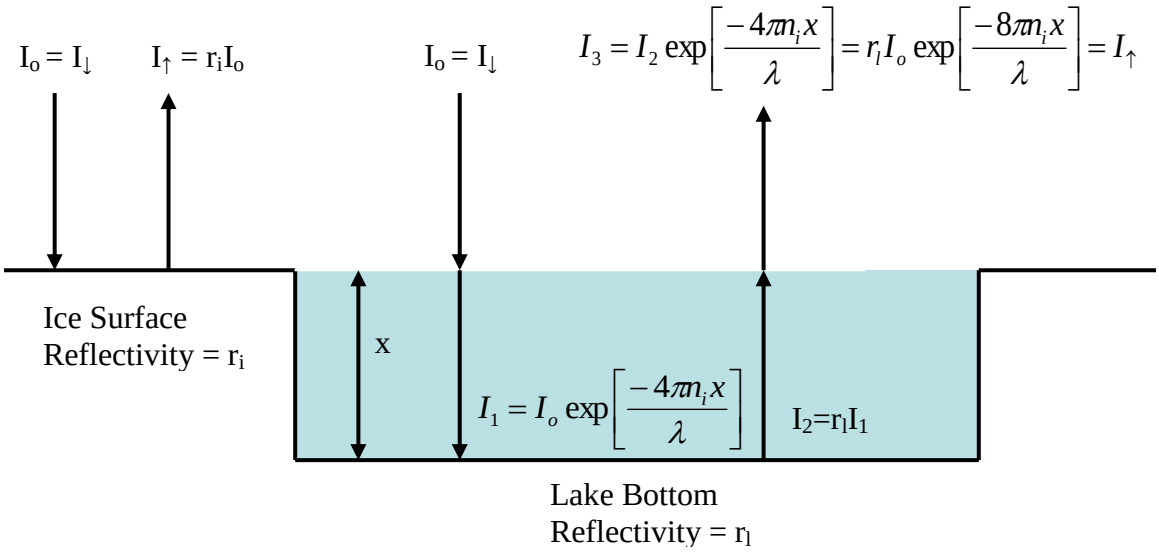

Figure 24: Schematic of lake depth measurements.

An alternative method of calculating lake depth based on two wavelengths is described in *Lyzenga* (1978) and will be denoted the ratio method for the remainder of this paper. This method is based on the constraint that the two wavelength bands used in the calculation must have a constant ratio of reflectances for all bottom types in a given scene. Since the only expected bottom type in the supraglacial lake data is ice, this constraint is ideally already fulfilled. Equations (12), (13), and (14) give the ratio method for determining lake depth. In these equations, subscript 1 refers to band 1, subscript 2 refers to band 2, r is reflectivity, β is the absorption coefficient of water, k is a constant which accounts for solar radiance, transmission through the atmosphere, and refraction at the surface of the water, f is a geometric factor which accounts for the slant angle through the water, I is observed radiance of each pixel,

and I_s is the observed radiance of water which is optically deep, meaning that it is deeper than approximately 40 meters.

$$R_b = \frac{r_1}{r_2} \tag{12}$$

$$R = \frac{I_1 - I_{s1}}{I_2 - I_{s2}} \tag{13}$$

$$x = \frac{1}{(\beta_1 - \beta_2) f}\left[\ln\left(\frac{k_1}{k_2}\right) - \ln\left(\frac{R}{R_b}\right)\right] \tag{14}$$

The input parameters of radiance from optically deep water bare some discussion. This term is intended to correct for light which is scattered back to the instrument by the water itself instead of being reflected by the lake bottom. However, supraglacial lakes do not typically reach depths of 40 meters, and, since the MUSCOX images are very limited in area, they do not contain any open water data. Additionally, the Landsat images used in this analysis do not contain data which stretches far enough into the ocean to be confidently called optically deep, and it is the judgment of this analyst that looking for this data in Landsat images which are adjacent in either time or space would incur unacceptable errors due to differences in sun angle and atmospheric conditions. Therefore, the deep water radiance terms will be set to zero in all calculations with the knowledge that some loss of accuracy will result.

The process of solving for the lake depth in both equations is hindered by several unknowns. The first unknown is the downwelling radiance. The MUSCOX and Landsat data do not give downwelling radiance explicitly, so the value will have

to be inferred. One method of inferring the downwelling radiance is to use a theoretical model of the radiance of the sun based on Planck's law and correct these values based on the distance between the sun and the Earth and the probable attenuation due to the atmosphere. However, this method has two significant sources of error. First, the sun closely approximates a blackbody but is not exact. Second, the attenuation through the atmosphere varies based on several parameters with may not be accounted for in any one empirical or analytical model. Since these two sources of uncertainty have the potential to create very large errors in the depth calculation results, the blackbody estimate of the sun's radiation will not be used for the lake depth calculations.

Another method of determining the downwelling radiance is to make estimates based on other pixels in the image, either by choosing bright pixels and assuming that the reflectivity at that location is approximately one or by choosing pixels with known ground types and using the known reflectivity to calculate the downwelling radiance. This method has the advantage of eliminating the need to consider the atmosphere in the calculations because it is generally valid to assume that all pixels within a small area of the same image have the same attenuation due to the atmosphere. A modification of this method that will be used to infer the downwelling radiation, as discussed below.

The second source of uncertainty in the lake depth calculations is the reflectivity of the lake bottom. Since there is no available data about the type of surface on the lake bottoms in these images, the reflectivity will have to be estimated

based on the reflectivity of the pixels in the scene, with the assumption that the reflectivity of the lake bottom is constant throughout the lake. This assumption may not be valid because of the possible presence of silt on the lake bottoms.

Following the technique of *Sneed and Hamilton* (2007), the unknown parameters of downwelling radiation and lake bottom reflectivity will be combined into a single variable in this analysis. Again assuming that lake bottom reflectivity is constant throughout the lake, pixels which are visually judged to contain very shallow water will be chosen to represent the downwelling radiance times the lake bottom reflectivity.

Lastly, the attenuation coefficient or imaginary coefficient of refraction of water are required in order to use both methods for calculating lake depth. This is a property of water which is dependent upon the salinity of the water and the presence of suspended particles. For this analysis, the water in the supraglacial lakes will be assumed to be fresh and have no suspended sediment. The absorption coefficient of pure water has been the subject of several investigations, such as that described in *Smith and Baker* (1981), which gives the absorption and backscattering coefficients of clear water at wavelengths between 200 and 800 nm. According to *Smith and Baker* (1981), total attenuation coefficient is related to the absorption and backscattering coefficients through equation (15), where a is the absorption coefficient and b is the backscatter coefficient. The coefficient of 0.5 applied to the backscattering coefficient represents Rayleigh scattering, so additional attenuation can occur depending on the properties of the water. However, without in situ data of

the lake depth, the lake bottom reflectance, and the properties of any suspended particles, the true attenuation coefficient of the water will remain a source of uncertainty.

$$\beta \geq a + 0.5b \qquad (15)$$

Since the observation band wavelengths extend as high as 2346 nm (with the longest center wavelength being 2205 nm), complex index of refraction data from *Petty* (2006) will be used to augment the data set from *Smith and Baker* (1981). The resulting absorption coefficients for the observation bands are shown in figure 25.

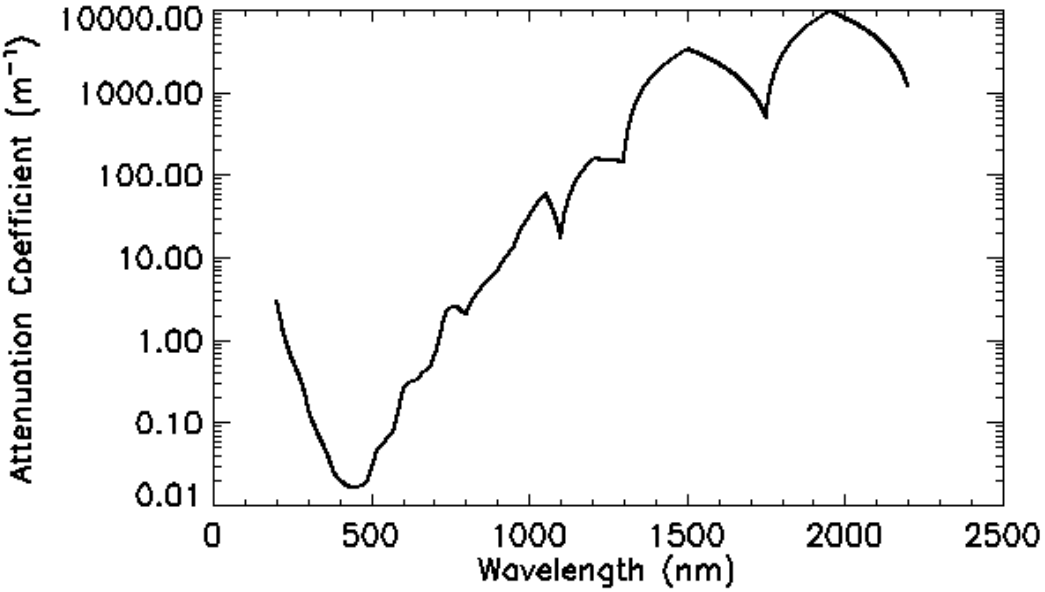

Figure 25: Absorption coefficient of water at the observation wavelengths.

D. Detection of Drained Supraglacial Lakes

A search of the literature produced few methods of detecting drained supraglacial lakes. *Box and Ski* (2007) resorted to a manual examination of a small area of the Greenland Ice Sheet in MODIS imagery. An identical change detection

method will be used as a starting point for locating drained glacial lakes, and then the lake location information will be used to attempt to find spectral signatures or textures unique to drained supraglacial lakes. These efforts will be discussed in detail in section V*B*. The changes during the month of July in the two drained lakes observed during the MUSCOX expedition are shown in figure 26, as imaged by Landsat 7.

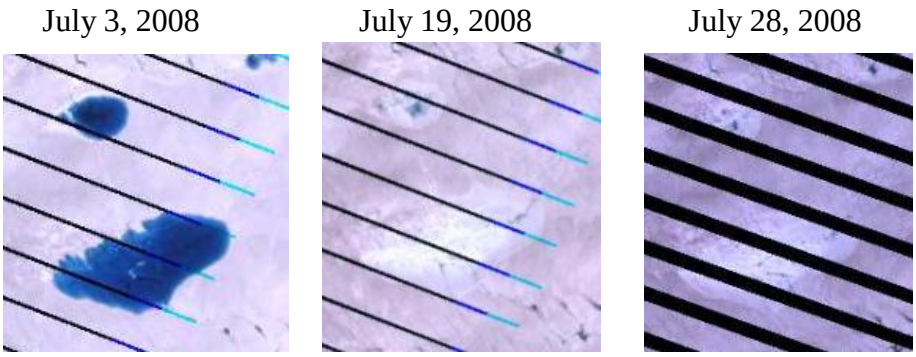

Figure 26: Evolution of two supraglacial lakes in July, 2008.

Many sections of the region shown in figure 26 were imaged during the MUSCOX mission, as shown in a mosaic in figure 27.

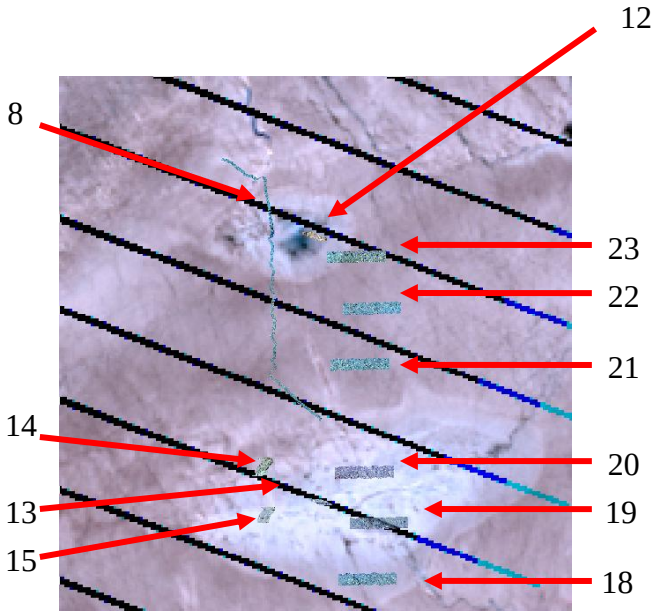

Figure 27: Mosaic of MUSCOX and Landsat dry lake data.

Using the data from image 20 as representative of a dry lake and data from image 21 as representative of unaltered ice, figure 28 shows the reflectivities of the two ground types.

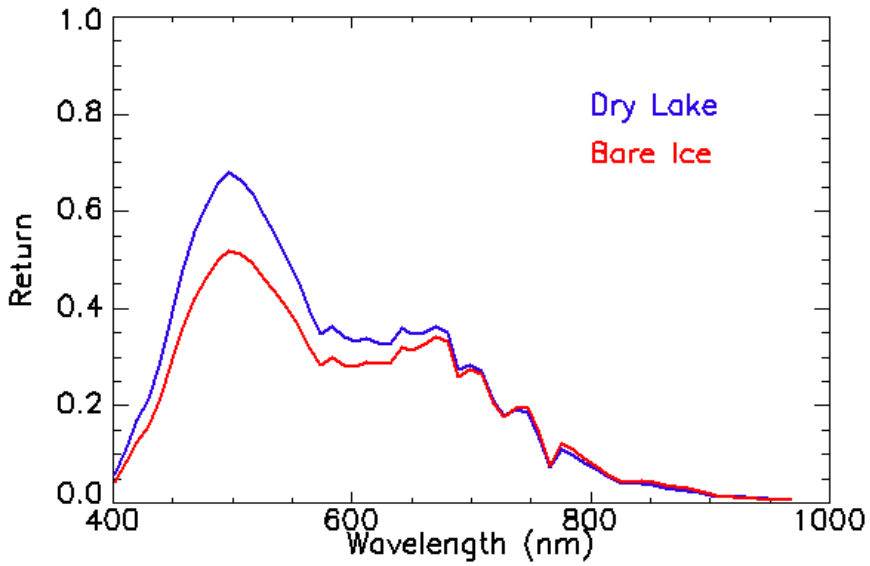

Figure 28: Returns of dry lake and bare ice.

E. Great Circle Distance

In cases where the distance between two pixels must be calculated, the great circle method will be used to create a result which accounts for the curvature of the Earth, though it neglects the flattening of the planet at the poles. The formula used to determine the distance is given in equation 16, which was taken from *Sinnott* (1984). In this equation, D is the distance between two points, R_E is the radius of Earth, ψ is latitude, γ is longitude, and subscripts 1 and 2 refer to the two locations.

$$D = 2R_E \sin^{-1}\left(\sqrt{\sin^2\left(\frac{\psi_1 - \psi_2}{2}\right) + \cos(\psi_1)\cos(\psi_2)\sin^2\left(\frac{\gamma_1 - \gamma_2}{2}\right)}\right) \quad (16)$$

IV. Analysis

The following section will describe the analysis and preliminary results.

A. Detection of Supraglacial Lakes

The first step in the analysis is to separate lake pixels from ice pixels in the MUSCOX and Landsat images of filled glacial lake. As figure 29 indicates, when applied to MUSCOX lake data from July 17, data set nine, the lake detection results from the ISODATA, adaptive boosting, and maximum likelihood algorithms are qualitatively similar. For reference, the orientation of the raw image and the processed images is difference because the raw image was graphed by ENVI in UTM coordinates while the processed images were graphed in IDL using an orthographic coordinate frame.

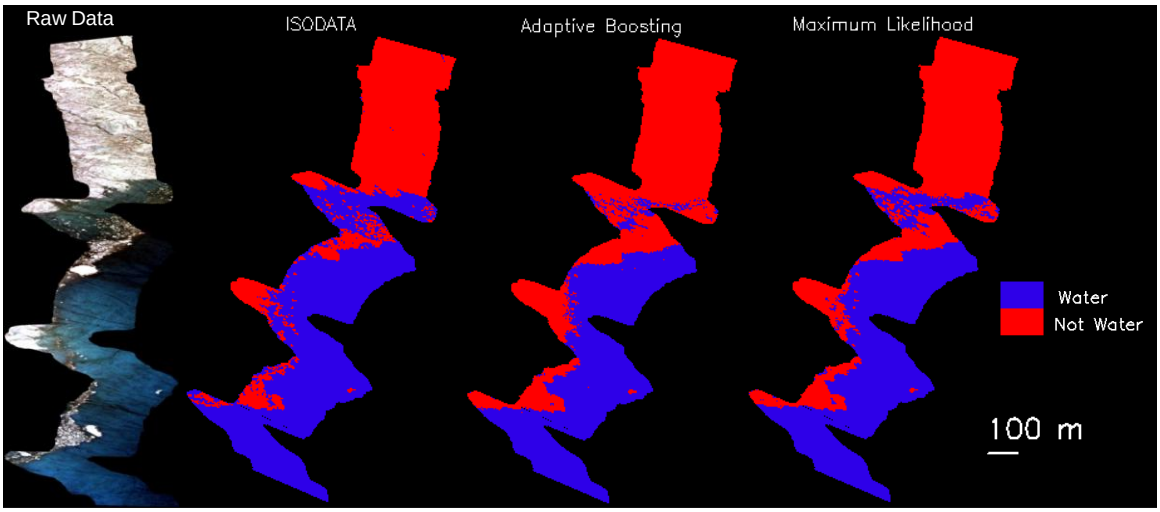

Figure 29: Results of classification algorithms on MUSCOX lake data.

Table 10 summarizes the qualitative results of the classification algorithms. It is immediately obvious that the two supervised algorithms, adaptive boosting and maximum likelihood, match each other with far more accuracy than ISODATA matches either of them, but the question still remains: which algorithm most accurately characterizes the boundaries of the lake in the image?

Table 10: Comparison of classification results from the three algorithms.

Algorithm	Number of Water Pixels	Water Area (m^2)	Number of Not Water Pixels	Not Water Area (m^2)	Water Area % Difference from ISODATA	Not Water Area % Difference from ISODATA
ISODATA	219422	27831.20	131618	16678.62	-	-
Adaptive Boosting	179638	22786.79	171402	21723.03	19.93 %	26.27 %
Maximum Likelihood	192091	24896.49	158949	19613.33	11.13 %	16.17 %

In the attempt to answer the question of which classification method is most accurate, a single row of data, marked in green in figure 30 has been chosen for closer

analysis. This row was chosen because it contains both ice and liquid water data, and all three algorithms disagree on the precise boundary between the two ground types.

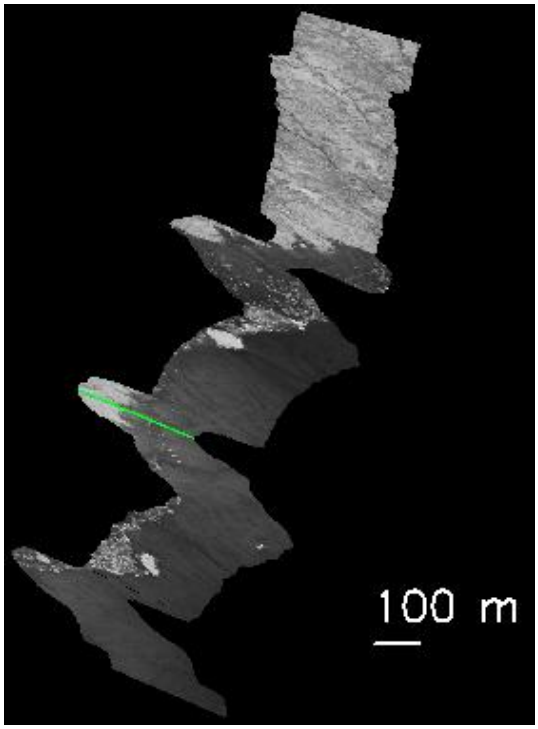

Figure 30: Data used for close analysis of classification algorithms.

As shown in figure 31, it is the judgment of this analyst that this row of data contains an ice feature, a small width of shallow water, a ridge, and finally the lake. Figure 31 also indicates the pixels where the three classification algorithms located water. The results of the ISODATA algorithm differs from the visual assessment on 50 pixels, or 15.63% of the row, adaptive boosting differs by 111 pixels or 34.69% of the row, and maximum likelihood differs by 57 pixels or 17.81% of the row. Clearly, though none of the algorithms is completely accurate, ISODATA and maximum likelihood correctly categorized significantly more of the data than adaptive boosting.

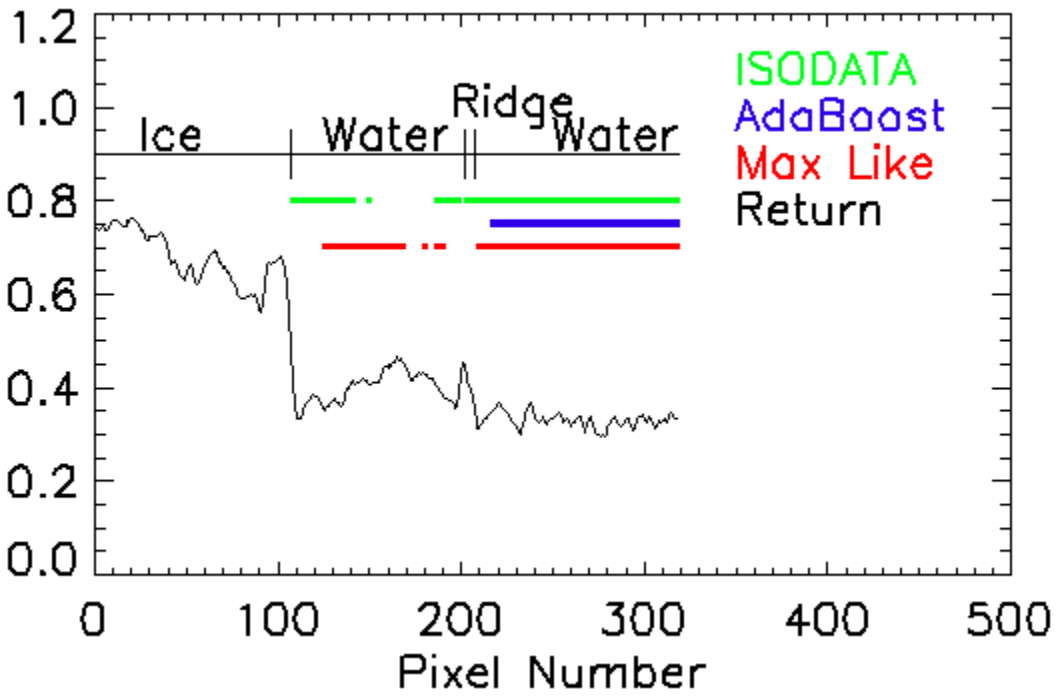

Figure 31: Location of actual and predicted water pixels for one row of data.

In an attempt to understand why a significant amount of the data from this row of the image was misclassified, figure 32 depicts the spectral data, using ice and water data from where the visual analysis and the three categorization algorithms are in agreement as a basis of comparison for pixels where the different analysis methods are in contention. Upon examination of figure 32, it immediately becomes clear why the pixels which were classified as a ridge by visual inspection were classed as water by the computer algorithms: the spectral data is similar in magnitude to the data corresponding to pure water pixels. The ridge shows the same double peak pattern in the specular data as the pure ice pixels, but the lower magnitude was probably enough to confuse the algorithms. The misclassification of the water pixels is more troubling,

because the misclassified water pixels have very similar spectral data to the known water pixels.

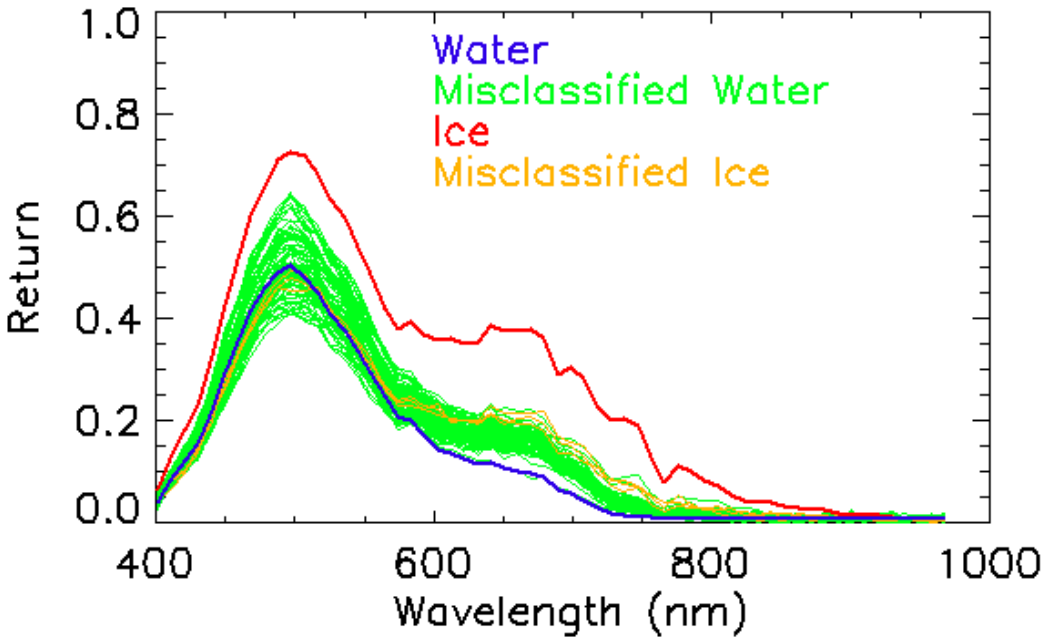

Figure 32: Spectral data for comparison of correctly and incorrectly classified ice and water data.

The most likely reason that the water pixels in question were misclassified by the supervised algorithms is because they were not provided with shallow water as part of their training data. Figure 33 gives the results of the adaptive boosting and maximum likelihood algorithms with this deficiency corrected. With the additional input data, adaptive boosting only differs from the visual analysis of the row of data on 4 pixels, or 1.25% of the data and maximum likelihood only differs from the visual analysis by 14 pixels or 4.38% of the data. This example demonstrates the importance of careful selection of input data to supervised classification algorithms, because the training data can influence the results dramatically. Additionally, since the unsupervised

classifier ISODATA only allows modification of its results via its statistical filters, there is a large potential for uncorrectable errors in its results. Therefore, ISODATA will be used only as a check on the results of the adaptive boosting and maximum likelihood algorithms and not for scientific analysis.

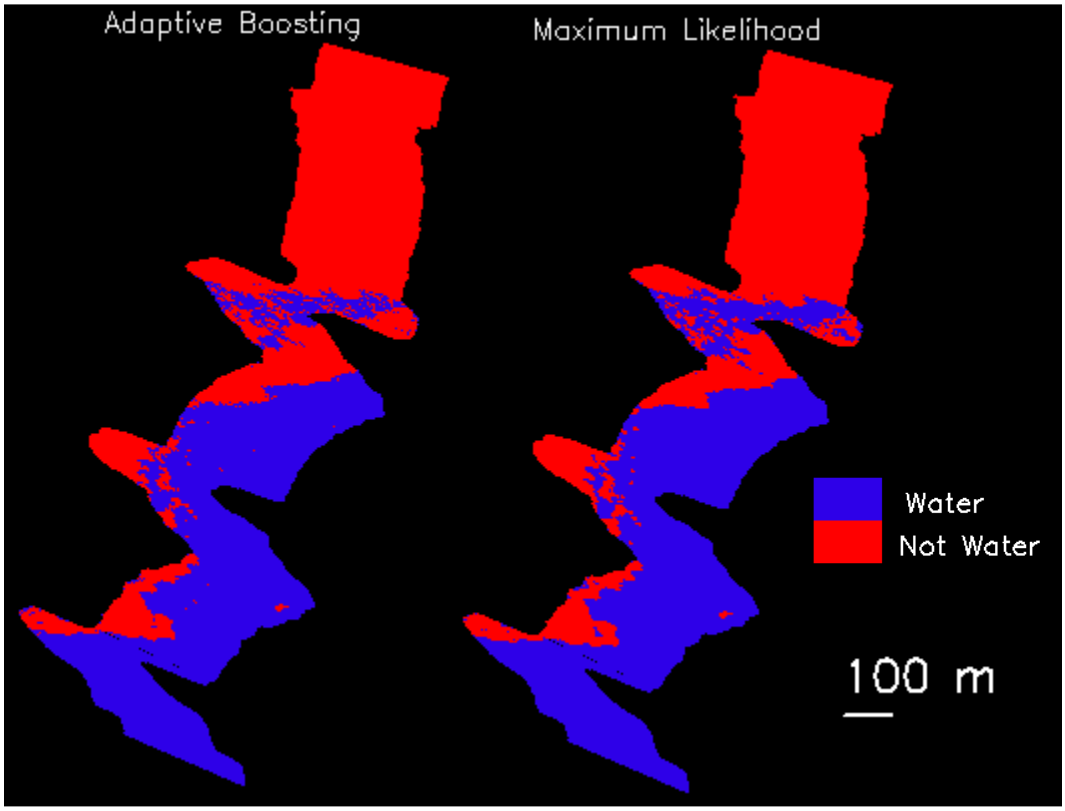

Figure 33: Results of adaptive boosting and maximum likelihood with additional training data.

The results of the classification analysis on all lake images are summarized in table 11. This includes MUSCOX data set nine with the modified training data to the supervised algorithms.

Table 11: Summary of classification of filled lake images

Data Set	Water Area (m^2)			Water Area % Difference from ISODATA	
	ISODATA	Adaptive Boosting	Maximum Likelihood	Adaptive Boosting	Maximum Likelihood
MUSCOX 9	27831.20	24722.71	24896.49	11.83%	11.13%
MUSCOX 10	166912.86	166209.33	165332.12	0.42%	0.95%
MUSCOX 11	61644.56	73764.63	71957.43	17.90%	15.44%
MUSCOX 16	58770.29	69429.98	69702.28	16.63%	17.02%
MUSCOX 17	57374.089	72776.67	71994.42	23.67%	22.60%
Landsat 1	$3.93 \cdot 10^6$	$3.05 \cdot 10^6$	$4.16 \cdot 10^6$	25.21%	5.69%
Landsat 2	$6.38 \cdot 10^6$	$4.91 \cdot 10^6$	$6.18 \cdot 10^6$	26.04%	3.18%

1. Comparison of Filled Lake Location with Landsat

In figure 34, the MUSCOX lake areas are overlaid on the two Landsat images of the same lake for location comparison. The lake locations for this figure were created using the maximum likelihood algorithm. Between July 3 and July 19, the area in the image which is covered by water increased by $1.86 \cdot 10^6$ m^2, as observed by Landsat 7 and determined based on the results of the maximum likelihood algorithm. The five MUSCOX observations in question took place between July 17 and July 19, meaning that the lake boundaries in the MUSCOX images should and do coincide more accurately with the July 19th Landsat image.

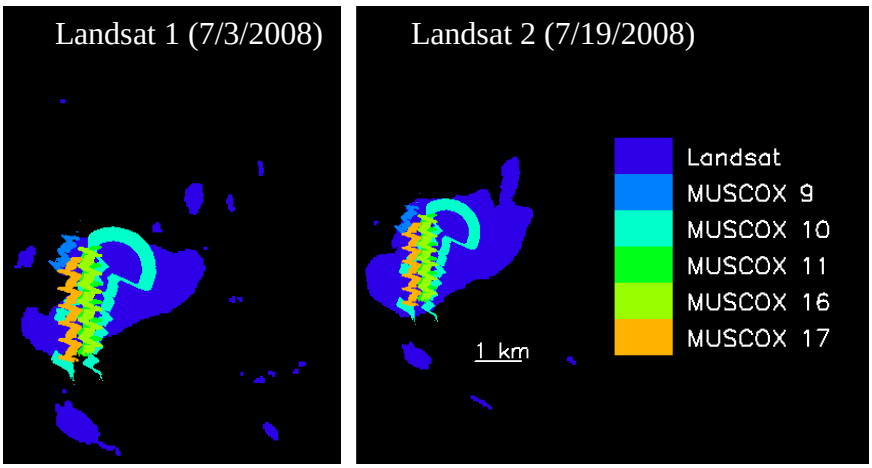

Figure 34: Overlaid MUSCOX and Landsat filled lake locations using maximum likelihood.

Taking a closer look at the lake boundaries in the Landsat and MUSCOX images, figure 35 gives the Landsat image from July 19th with the lake boundaries from both Landsat and MUSCOX highlighted. The lake pixels were found using adaptive boosting and maximum likelihood, and the lake boundaries were found by searching for pixels which were classified as different ground types from their neighbors.

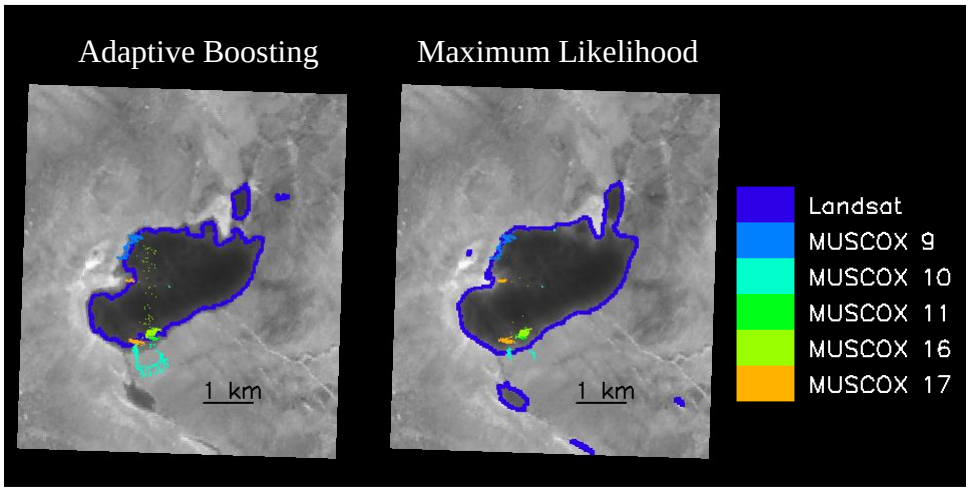

Figure 35: Boundaries of the supraglacial lake as found by adaptive boosting and maximum likelihood. The Landsat image is from July 19th.

Figure 36 gives the distribution of errors in location between the lake boundary pixels detected using adaptive boosting on the MUSCOX images and their nearest neighbor in the Landsat image detected using the same method. The distances were found using the great circle calculation discussed above, which yields only positive distance results.

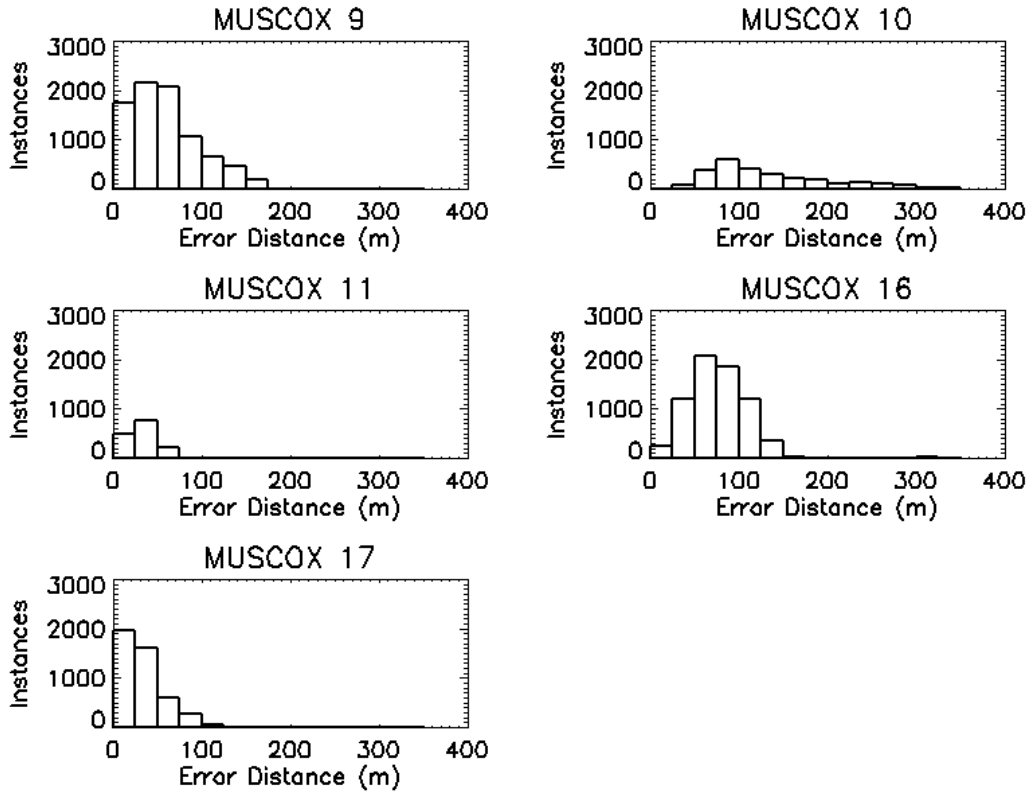

Figure 36: Distribution of errors in the lake boundary locations as found using adaptive boosting, comparing MUSCOX to Landsat on July 19th.

The distribution of errors in location between the lake boundary pixels found using maximum likelihood are shown in figure 37.

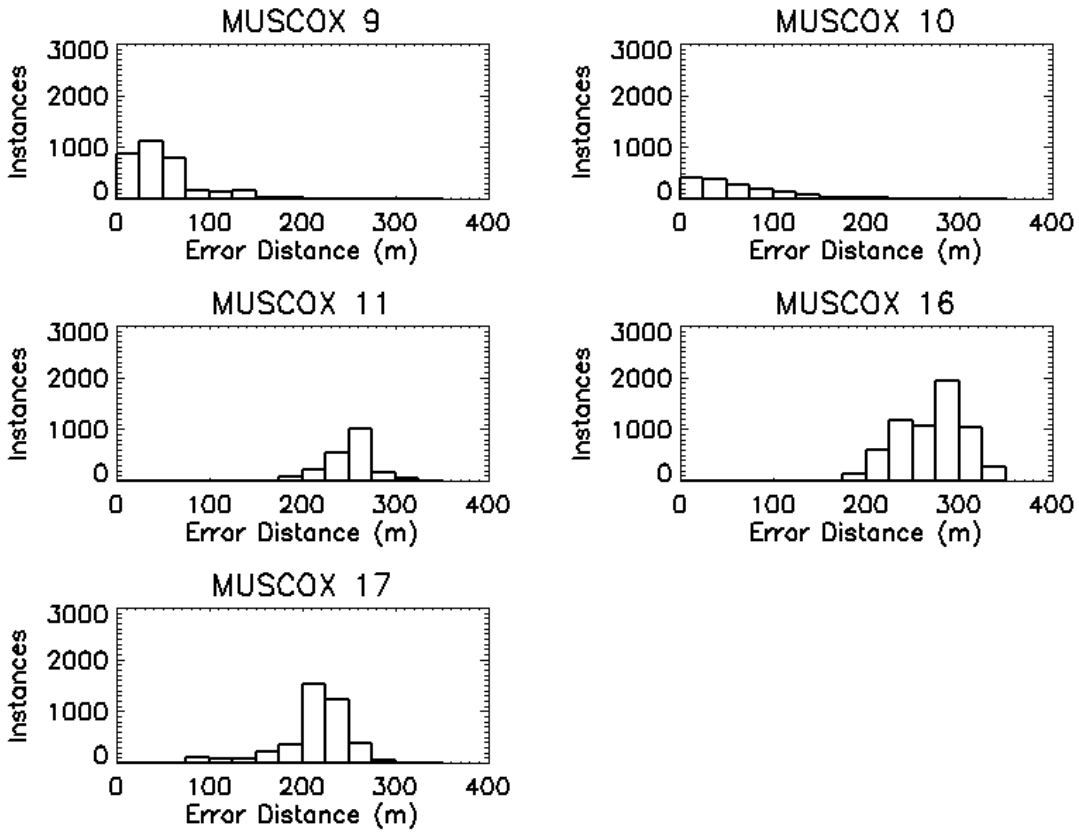

Figure 37: Distribution of errors in the lake boundary locations as found using maximum likelihood, comparing MUSCOX to Landsat on July 19th.

Table 12 gives the mean and standard deviation of the errors in the boundaries of the large center lake, comparing the five MUSCOX images with liquid water to the Landsat image from July 3rd.

Table 12: Mean and standard deviation of the lake boundary locations in the MUSCOX images compared to the Landsat image from July 3rd.

MUSCOX Image	Method	Mean (m)	Standard Deviation (m)
9	Adaptive Boosting	144.42	56.17
	Maximum Likelihood	114.23	58.51
10	Adaptive Boosting	486.64	255.32
	Maximum Likelihood	360.72	79.75
11	Adaptive Boosting	255.32	13.22
	Maximum Likelihood	88.22	21.08
16	Adaptive Boosting	136.20	28.90
	Maximum Likelihood	46.87	26.19
17	Adaptive Boosting	275.81	36.59
	Maximum Likelihood	146.01	40.50

Table 13 gives the mean and standard deviations of the errors in the boundary locations, comparing the MUSCOX images to the Landsat image from July 19th.

Table 13: Mean and standard deviation of the lake boundary locations in the MUSCOX images compared to the Landsat image from July 19th.

MUSCOX Image	Method	Mean (m)	Standard Deviation (m)
9	Adaptive Boosting	59.58	37.85
	Maximum Likelihood	49.37	35.74
10	Adaptive Boosting	223.68	178.98
	Maximum Likelihood	64.45	71.99
11	Adaptive Boosting	32.66	15.40
	Maximum Likelihood	250.85	24.18
16	Adaptive Boosting	79.15	42.83
	Maximum Likelihood	271.24	36.43
17	Adaptive Boosting	33.88	23.64
	Maximum Likelihood	231.42	38.52

Comparison of tables 12 and 13 indicates that the MUSCOX images match slightly more accurately with the Landsat image from July 19th and that the results of maximum likelihood are more accurate than the results of adaptive boosting except in the cases of data sets 11, 16, and 17, where the exact boundary between shallow water and bare ice is in dispute. Additionally, though many of the errors in location seem unacceptably large, it is important to note that the MUSCOX data was compared to the center of the Landsat pixels, and with Landsat's 30 meter resolution, an error of 300 meters is only ten pixels in the cross or along track directions in the Landsat data or slightly more than seven pixels at a 45° angle to the cross or along track directions.

In all of the analyzed images, ten pixels is a reasonable error because of the effect of mixed type pixels, which cause uncertainty in the true boundary between water and ice, and because of the possibility that the exact boundaries of the lake can change between observations.

To test the hypothesis that the boundary error results will improve with improved spatial resolution, figure 38 shows the distribution of boundary error distances from MUSCOX data sets six and eleven, which overlap significantly, with the boundaries found using adaptive boosting and maximum likelihood. Using adaptive boosting, the average error in edge location is 49.23 m and the standard deviation is 22.22 m. Using maximum likelihood the average error in edge location is 15.64 m and the standard deviation is 12.74 m. This is significantly reduced from the errors calculated by comparing MUSCOX to Landsat, indicating that a significant part of the errors in the earlier calculation simply comes from the larger spatial resolution of the Landsat data, coupled with the fact that the lake boundaries are constantly changing.

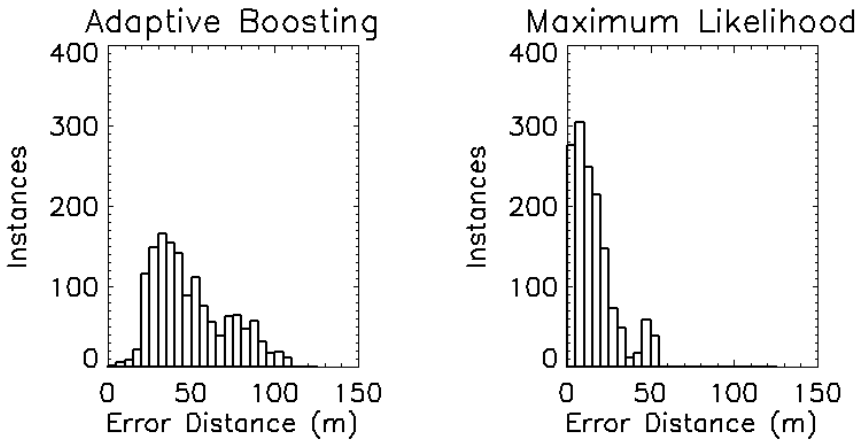

Figure 38: Error in lake boundary locations using overlapping MUSCOX observations six and eleven.

In spite of these rationales, enough error in these results remains to prove that, in ground type detection, none of the algorithms used are an accurate substitute for a visual study by a skilled analyst.

B. Volume of Supraglacial Lakes

As seen above, MUSCOX data set nine encompasses the northern edge of a supraglacial lake and has a total area of 44509.82 m^2. Adaptive boosting determined that the lake area in this image is 24722.71 m^2 and maximum likelihood determined that the lake area is 24896.49 m^2. Calculating the water depth of each lake pixel requires application of the preprocessing and method algorithms above, which has the largest effect on the incident radiation, lake bottom reflectance, and path length used in the analysis.

Incident radiation and lake bottom reflectance are both unknown physical properties of the scene. With the assumption that the lake bottom reflectance is constant for the entire lake, the observed radiance from the very shallowest lake

pixels can be said to account for both incident radiation and lake bottom reflectance. As discussed above, this method was used successfully in an analysis of imagery of melt ponds on the Greenland Ice Sheet gathered by the Advanced Spaceborne Thermal Emission and Reflection Radiometer (ASTER) as described in *Sneed and Hamilton* (2007). For this analysis, the pixels chosen to represent shallow water will be judged visually. Figure 39 shows the pixels selected to represent shallow water in MUSCOX data set nine and their average return for each band.

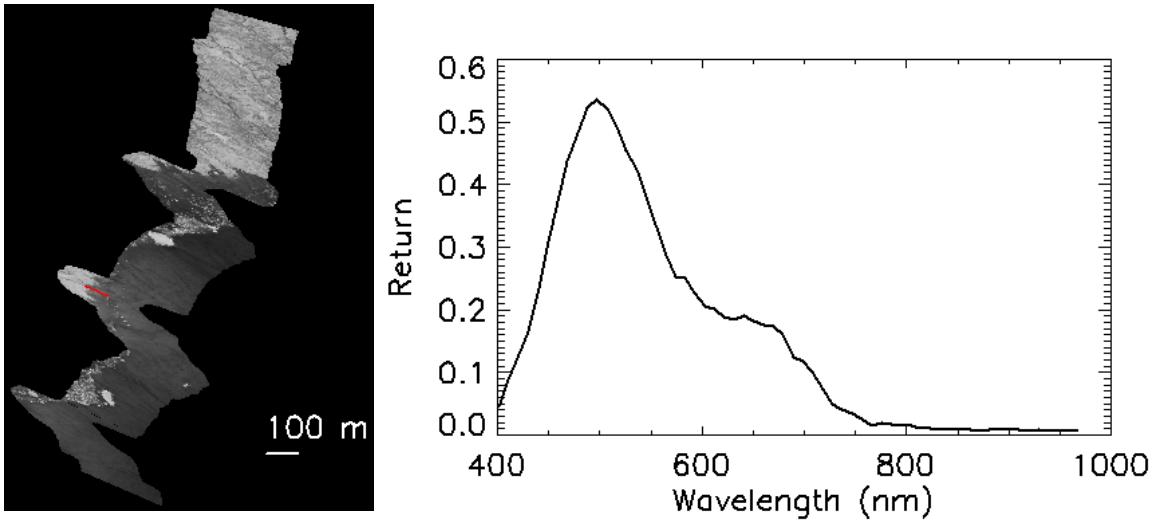

Figure 39: MUSCOX data set nine with shallow water pixels highlighted and the average spectral signature of the shallow water pixels.

The second consideration for the calculation of lake depth is the path length through the water. Ordinarily, the path length calculation would include off-vertical paths for both upwelling and downwelling radiance. However, as discussed in the preprocessing section, data set nine was observed when the sun had a zenith angle of 89.61^{o}, which, according to the Fresnel relations of an air to water interface, means that only 3.99% of the light penetrated the water and the rest was reflected by the

surface. As a result, the majority of the light which actually penetrates the surface of the water was in fact scattered at least once by the atmosphere and arrived at the air to water interface at a different angle from the light which traveled directly from the sun. Attempting to approximate the amount of light which comes from all visible parts of the atmosphere, the amount of light which penetrates the air to water interface, and the resulting angle the light is refracted to would overly complicate the problem. Therefore, for the MUSCOX data sets, the path that the light takes downward through the water will be assumed to be equal to the water depth. The path the light takes upward through the water will not be assumed equal to the water depth because the angle between each detector in the imager and the nadir direction is known, as is the effect of refraction at the water to air interface.

With all parameters in the depth calculation equations accounted for, the equations can be applied, with the results shown in figure 40, using the results of the maximum likelihood algorithm for the locations of the water pixels. In this figure, data from channel 26 with a center wavelength of 641.21 nm was used for the calculation data and the method used was the unaltered Beer's Law. The average depth in this image is 1.86 m, the maximum depth is 5.65 m, and the total water volume is 46122.45 m^3.

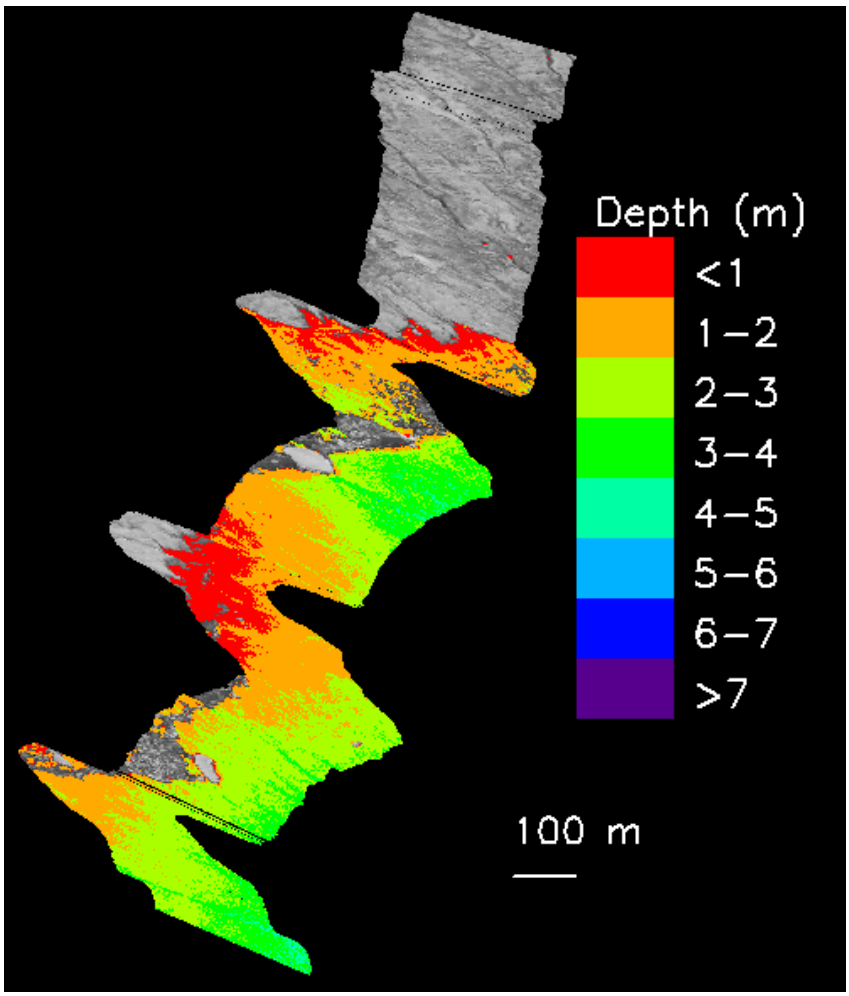

Figure 40: Results of depth calculation of MUSCOX data set nine using maximum likelihood and Beer's Law, applied to channel 26.

These results match well with the known typical depths of supraglacial lakes: less than approximately 10 or 20 meters (*Sneed and Hamilton*, 2007). However, the use of a different observing channel in the calculations yields an entirely different result, as indicated in figure 41, which is identical to figure 40 but uses channel 16 with a center wavelength of 545.21 nm for the calculation. The results of this calculation indicate that the average depth is 3.8 m, the maximum depth is 11.26 m,

and the total volume is 94100.61 m^3. Clearly, these results cannot both be correct.

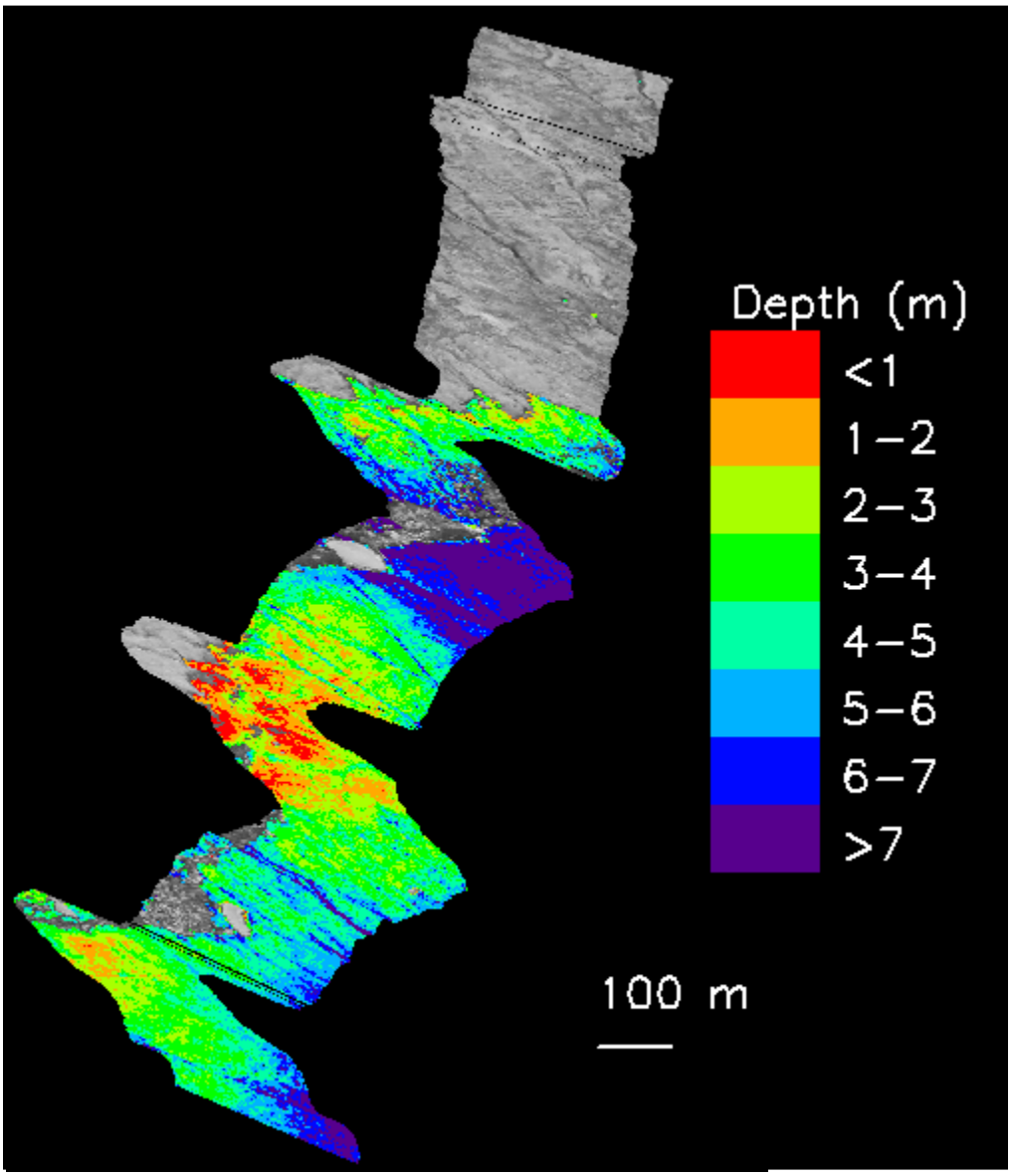

Figure 41: Results of depth calculation of MUSCOX data set nine using maximum likelihood and Beer's Law, applied to channel 16.

The most likely reason for the discrepancy in the calculated depths is a wavelength dependent property of the water which was not previously accounted for. The most likely source of error is the presence of particles which are suspended in the

water, influencing the attenuation coefficient, and settled on the lake bottom, changing the reflectivity. As mentioned above, no information about the properties of the lake bottoms, including the presence or absence of settled particles, is available, therefore it is impossible to separate any attenuation in signal due to water depth from attenuation in signal due to changes in lake bottom reflectivity. However, the scattering properties of different wavelengths of light due to particles of different sizes are well known and can be investigated. Toward that end, figure 41 shows the calculated depths for a sampling of typical water pixels at all observation wavelengths. As figure 42 indicates, the largest depths are calculated using the smallest wavelengths and at wavelengths longer than about 700 nm the calculated lake depth is practically zero.

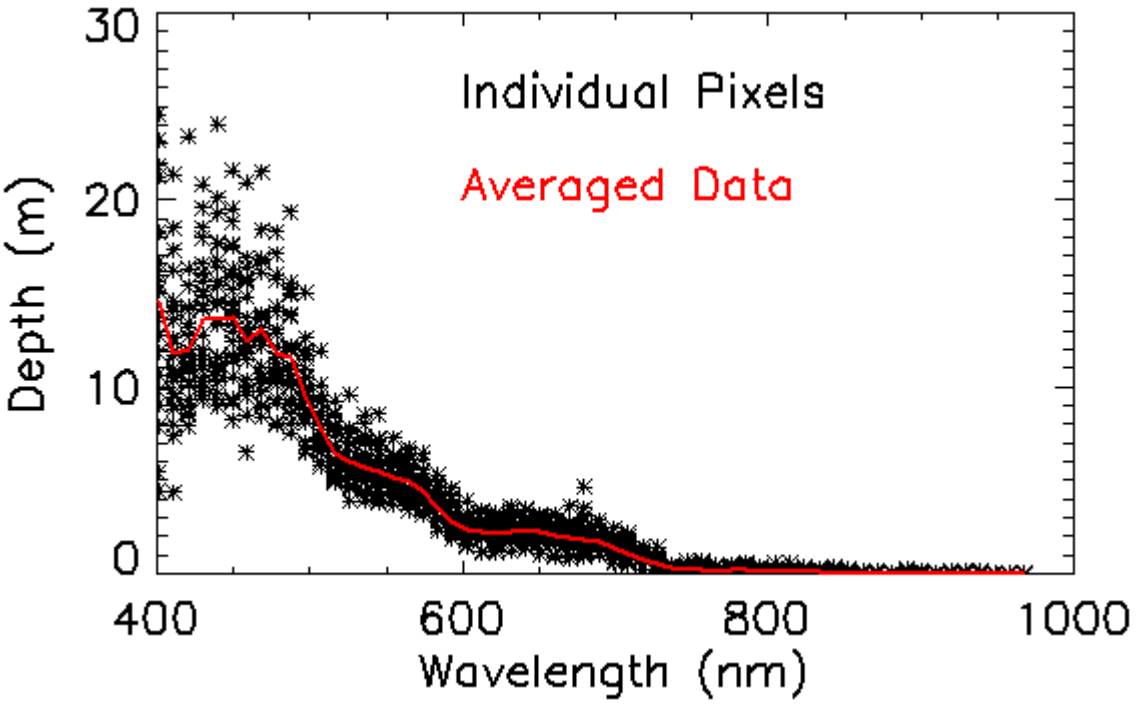

Figure 42: Calculated depths at various wavelengths.

Figure 43 gives the results of arbitrarily setting the depth of a single pixel to its average value over all wavelengths and solving for the absorption coefficient with the actual absorption coefficient of clear water overlaid. It should be noted that based on this figure and others, the MUSCOX data gathered at wavelengths above approximately 750 nm is so low that it should not and will not be used for depth calculations. Figure 43 indicates that the calculated attenuation coefficient is higher than the actual attenuation coefficient at short wavelengths and lower than the actual attenuation coefficient at longer wavelengths.

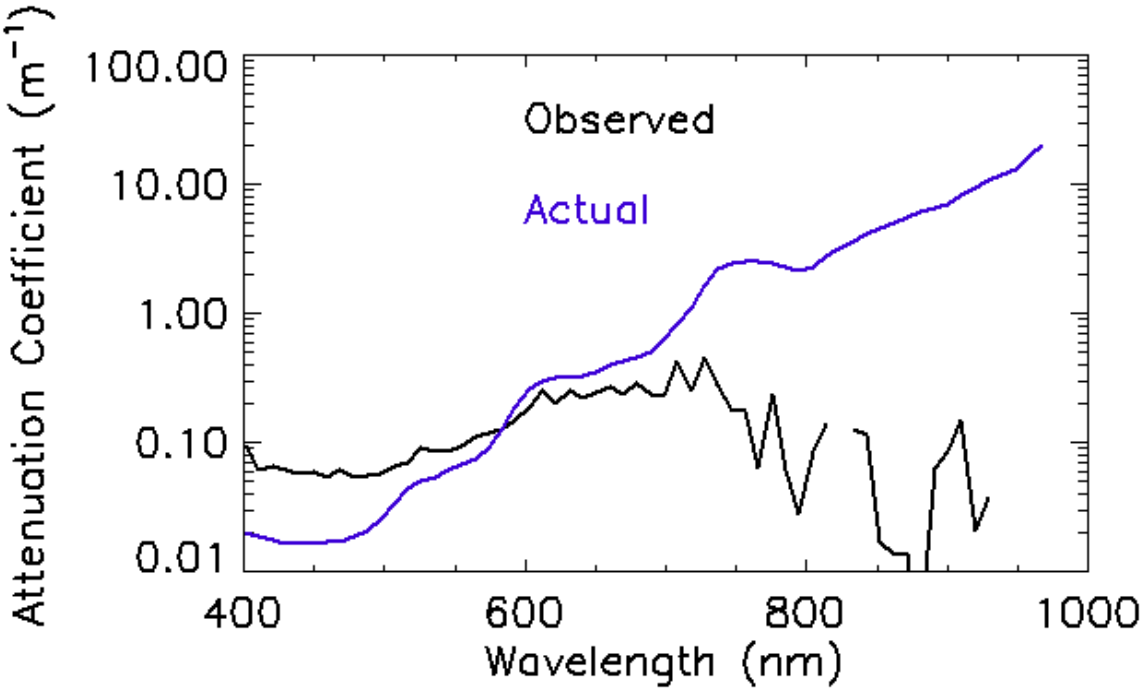

Figure 43: Calculated attenuation coefficient based on a constant lake depth and the actual attenuation coefficient.

A similar analysis on the other input to the depth calculations, the incident radiation and bottom reflectivity term, is shown in figure 44. This figure was created

by assuming an arbitrary constant depth and calculating the incident radiation times the bottom reflectivity using the published attenuation coefficient. These results indicate that, while not identical, the calculated and actual incident radiation and reflectivity term are very similar at wavelengths below 575 nm. Above 575 nm, the calculated term increases unrealistically, most likely because of data which is unreliable because of low light levels at long wavelengths. These results indicate that channels above 575 nm should not be used in the calculation. This also hints at the possibility that the deep water pixels may have lower bottom reflectivities than shallow water pixels, since the observed and actual reflectance time incident radiation are more similar at short wavelengths, but this cannot be determined with certainty without knowing the actual water depth.

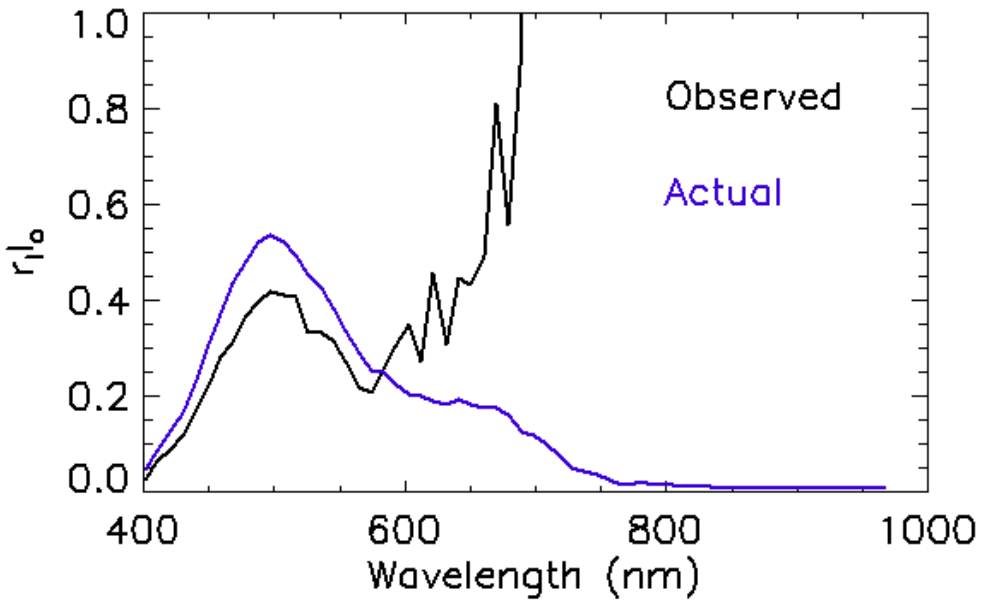

Figure 44: Calculated incident radiation times bottom reflectivity using a constant water depth.

The fact that the calculated attenuation coefficient is lower than the actual attenuation at some wavelengths is contrary to common sense, which would indicate that the addition of suspended particles to a medium could not reduce the attenuation coefficient of the medium. Several factors combine to create an explanation for this effect. The first factor is the incoming radiation, which, as discussed previously, must have been scattered at least once by the atmosphere in order to reach the lake surface at an angle which allows it to change mediums. Rayleigh scattering is the primary scattering mechanism in the atmosphere because air molecules are much smaller than the wavelength of light in the visible regime. This scattering mechanism is wavelength dependent, preferentially scattering light with shorter wavelengths. Therefore, the light which penetrates the surface of the water will be primarily at the blue end of the spectrum. Additionally, water preferentially absorbs light with longer wavelengths, meaning that the signal in the longer wavelength channels is rapidly diminished when traveling through the water. These two properties of light manifest themselves in the data with extremely low signal levels in all channels at approximately 700 nm and above. Therefore, these long wavelength channels should not be used for depth calculations. In the case of observations where the observing channel has a wavelength of less than 700 nm but the calculated depth is still unreasonably low, the most likely explanation is the presence of suspended sediments or perhaps floating ice crystals which are of such a size or have optical properties which would cause the light to be reflected back to the instrument before reaching the lake bottom. This is also consistent with the properties of Rayleigh scattering which

scatters light approximately equally in the forward and backward directions.

Operating now with the hypothesis that Rayleigh scattering is occurring for long observation wavelengths above 700 nm, what is the explanation for the vastly larger calculated depths at the short observation wavelengths? Assuming that the radius of the suspected suspended particles is constant and much smaller than 700 nm, decreasing the observation wavelength will change the scattering properties because the wavelength and particle radius will become more similar in magnitude. This means that there is a potential for a transition from Rayleigh scattering at long wavelengths to scattering which is described by Mie theory for the short wavelength observation bands. This is significant because Mie theory describes scattering preferentially in the forward direction, meaning that the attenuation coefficient used in the depth calculations could be overestimating the amount of radiation which is scattered out of the path (*Petty*, 2006). Additionally, Mie theory describes the extinction efficiency of spheres based on the ratio of the particle size to the wavelength. For a constant and small particle size, near the transition between scattering described by Rayleigh and Mie theories, decreasing the wavelength increases the extinction efficiency. This matches exactly with the attenuation coefficient results shown in figure 42, where the calculated attenuation coefficient is lower than the attenuation coefficient of pure water at long wavelengths and higher than the attenuation coefficient of pure water at short wavelengths. If the hypothesis that suspended particles in the lake are causing Mie theory scattering is correct, then at the short observation wavelengths for any given water depth the signal received by

the instrument will be stronger than it would be otherwise because of increased forward scattering, but will be subject to increased extinction efficiency which will decrease the signal strength. Which of these properties dominates is a question which cannot be answered without additional knowledge of the scatterers themselves.

What, then, is the correct observing channel to use in the calculations to gain the most accurate depth results? Unfortunately, lacking both measurements of the actual lake depth at the time of the observations and information about the presence, absence, concentration, or size of any suspended particles in the lake, it is impossible to determine with certainty which observing wavelengths give the most accurate depths or to account for the additional scattering effects of the suspected suspended particles. Instead, this analysis will attempt to solve the problem by using the observing channel which the hypothesis described above indicates should give the most accurate results. Therefore, Beer's law will be applied to two separate observation channels: a short wavelength band which could have increased forward scattering but also increased extinction due to particles which are of comparable size to the wavelength, and a long wavelength band which could have lower extinction efficiency and more closely resemble Rayleigh scattering. However, consideration should also be given to the planned comparisons with Landsat data, which has a more coarse spectral resolution. Thus, MUSCOX channel nine at 478.01 nm, which corresponds to the center of Landsat channel one at 441 to 514 nm and MUSCOX channel 18 at 564.41 nm, which corresponds to the center of Landsat channel two at 519 to 601 nm, will be used for this analysis. However, as mentioned, the accuracy

of these results cannot be confirmed without knowing the real lake depths, therefore, while the results in this analysis will be internally comparable, they cannot be taken as representative of the actual lake properties. Additionally, comparison of these results with the results of other studies, (*McMillan et. al.*, 2007) and (*Sneed and Hamilton*, 2006), indicates that the depths calculated using channel nine are a gross overestimation of the actual depths of lakes on the Greenland ice shelf.

Figure 45 gives the results of the depth calculation using channel nine. The maximum calculated depth in this image is 28.83 m, the average depth is 7.57 m, and the total volume is 178253.06 m^3.

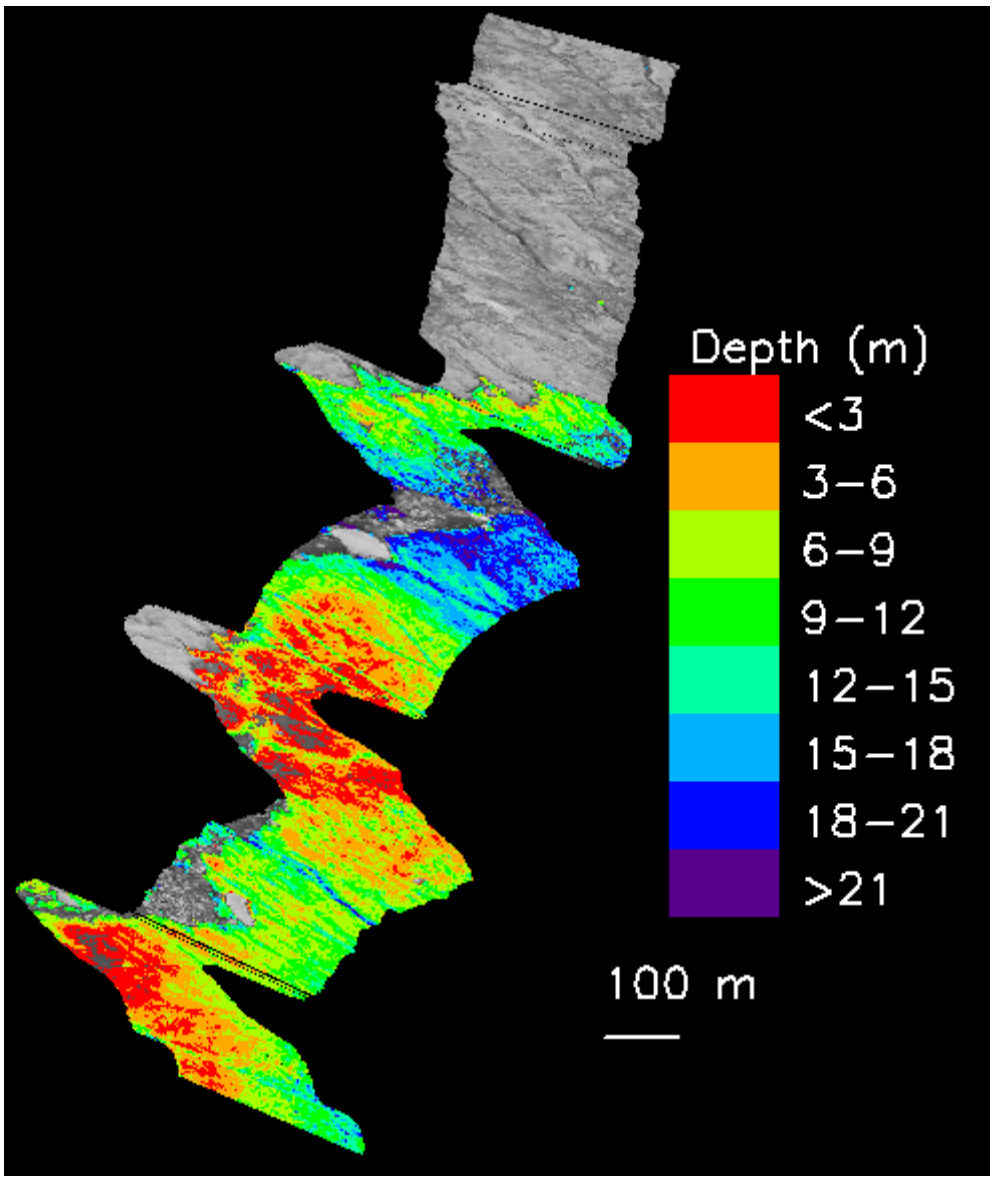

Figure 45: Results of Beer's Law calculation for water depth, using MUSCOX channel nine.

The results of the depth calculation using channel 18 are shown in figure 46. These results indicate that the maximum depth in the image is 10.15 m, the average depth is 3.54 m, and the total volume is 87810.79 m^3.

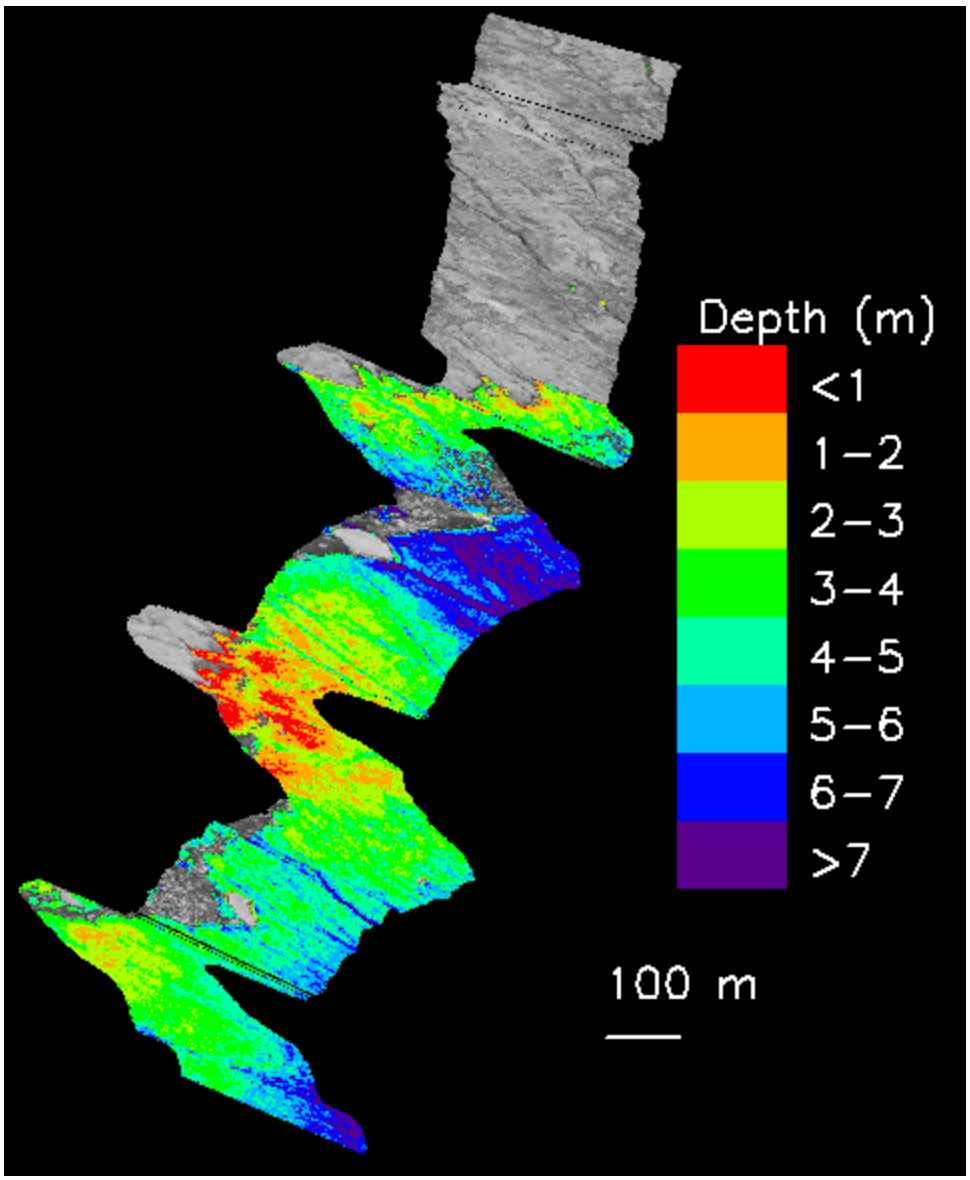

Figure 46: Results of Beer's Law calculation for water depth, using MUSCOX channel 18.

Figure 47 shows the results of calculating the lake depth using the ratio method calculated using MUSCOX channels nine and eighteen, which correspond to the center of Landsat channels one and two. The ratio method indicates that the maximum depth in the image is 7.63 m and the average depth is 2.39 m, for a total

volume of 58892.04 m^3. Clearly, the lake depth values here are quite different from the results from using Beer's Law on a short wavelength channel and far more similar to Beer's Law on a long wavelength channel. Additionally, assuming that the lake bottom reflectance equivalency assumption in the ratio method derivation has not been violated, the results of the ratio method are likely to be more accurate than the results from the unaltered Beer's law, because this method has the additional benefit of being unaffected by changes to water quality as long as the relative attenuation coefficient between the two calculation bands is constant. The possibility that these results are more accurate is also supported by comparison with the published results from other studies, which indicate that the maximum lake depth should not be deeper than 10 or 20 meters.

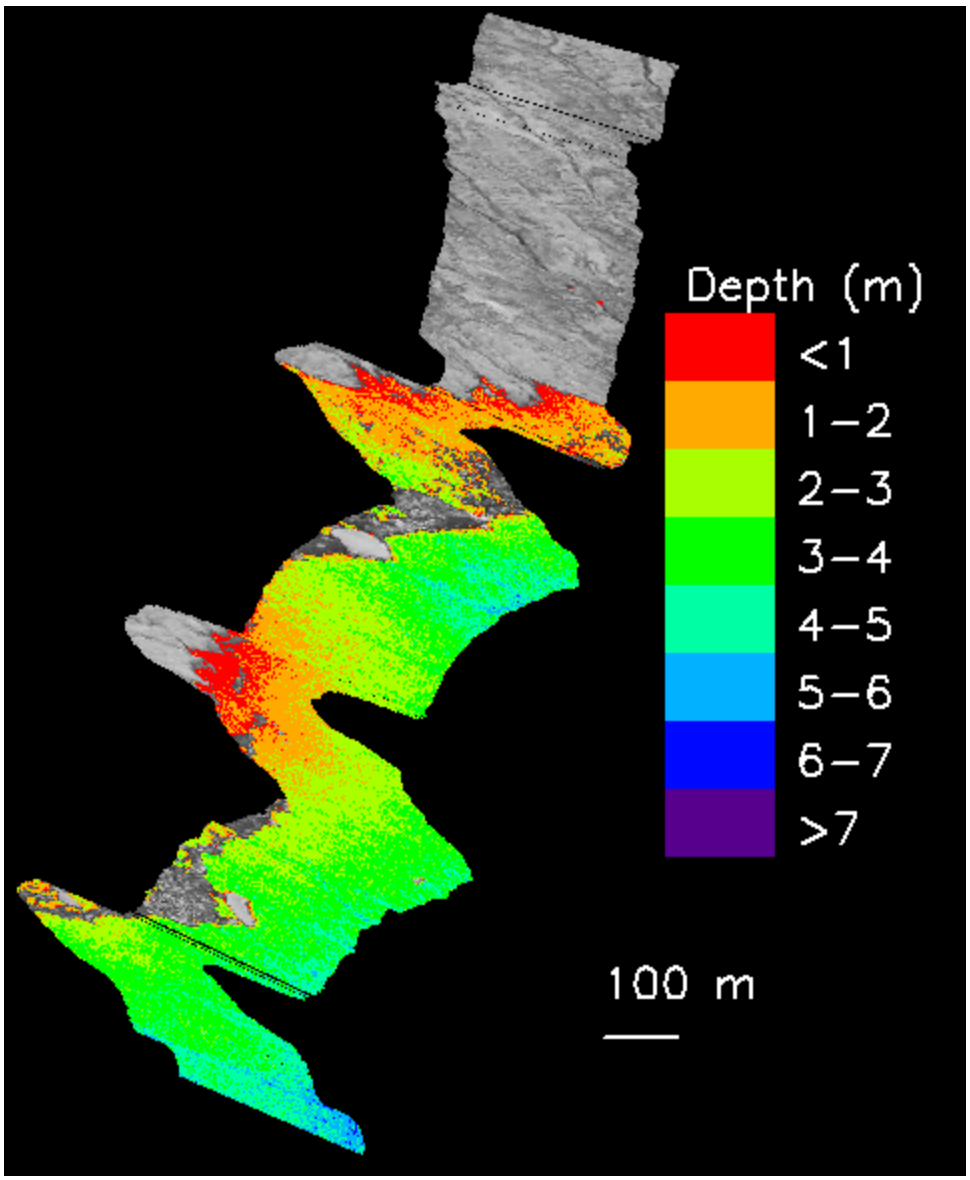

Figure 47: Results of lake depth calculations using the ratio method with channels nine and eighteen.

An additional analysis of the Beer's law and ratio methods of determining lake depth reveals that the ratio method is much more stable. Using a sample of typical water pixels from data set nine, applying Beer's Law to channel nine, the average of the depth results decreases by 4.76% when the attenuation coefficient is

increased by 5% and the average depth increases by 11.06% when the incident radiation and bottom reflectance term is increased by 5%. Meanwhile, using the ratio method the average depth also decreases by 4.76% when the attenuation coefficient in both bands is increased by 5% and the average depth is unaltered by a 5% increase in the incident radiation and bottom reflectance term in both bands. Increasing the attenuation coefficient of only one calculation band by 5% increases the average depth by 1.65% and increasing the incident radiation and bottom reflectance in one calculation band by 5% decreases the average depth by 15.91%. This last error, which is significantly higher than the other changes in depth may be caused because altering only one bottom reflectance value violates the underlying assumption in the derivation of the ratio method.

V. Results and Discussion

The following section will expand on the analysis by applying the methods described there to all of the relevant data sets and discuss the results.

A. Volume of Supraglacial Lakes

Table 14 gives the numerical results of the depth lake analysis on all lake images. For simplicity, only the lake location results from the maximum likelihood algorithm are shown here. The MUSCOX calculations were made using channel nine and the Landsat calculations where made using the 441-514 nm band.

Table 14: Quantitative comparison of lake depth data using Beer's Law on MUSCOX channel nine and Landsat channel one.

Data Set	Maximum Depth (m)	Average Depth (m)	Total Volume (m^3)
MUSCOX 9	28.83	7.57	178253.06
MUSCOX 10	38.20	13.19	2173136.6
MUSCOX 11	31.05	5.40	334104.22
MUSCOX 16	28.82	4.30	223463.74
MUSCOX 17	36.62	9.97	692662.29
Landsat 1	18.53	6.73	$2.69 \cdot 10^7$
Landsat 2	16.96	8.08	$4.73 \cdot 10^7$

Table 15 gives the results of Beer's Law on the longer observation channels.

Table 15: Quantitative comparison of lake depth data using Beer's Law on MUSCOX channel eighteen and Landsat channel two.

Data Set	Maximum Depth (m)	Average Depth (m)	Total Volume (m^3)
MUSCOX 9	10.15	3.54	87810.79
MUSCOX 10	19.67	7.90	1142137.4
MUSCOX 11	13.05	4.48	311544.90
MUSCOX 16	11.98	3.52	227981.28
MUSCOX 17	14.45	4.54	318872.82
Landsat 1	7.10	3.47	$1.43 \cdot 10^7$
Landsat 2	7.78	4.64	$2.82 \cdot 10^7$

The numerical results of the ratio method analysis are given in table 16 for all lake data sets.

Table 16: Quantitative comparison of lake depth using the ratio method.

Data Set	Maximum Depth (m)	Average Depth (m)	Total Volume (m^3)
MUSCOX 9	7.63	2.39	58892.04
MUSCOX 10	16.41	6.20	1022349.3
MUSCOX 11	9.88	4.35	307968.47
MUSCOX 16	10.10	3.39	237934.13
MUSCOX 17	9.42	2.87	198123.39
Landsat 1	5.04	2.57	$1.06 \cdot 10^7$
Landsat 2	5.89	3.69	$2.28 \cdot 10^7$

All five MUSCOX lake depth images, as calculated using Beer's Law and data from channel nine, are overlaid on the Landsat image from July 19 in figure 48. Since all six data sets are graphed using the same color scheme, the MUSCOX images are marked with white boxes to show their boundaries. An examination of figure 48 shows that the magnitude of the depth results in the MUSCOX images generally follows the trends in the Landsat image.

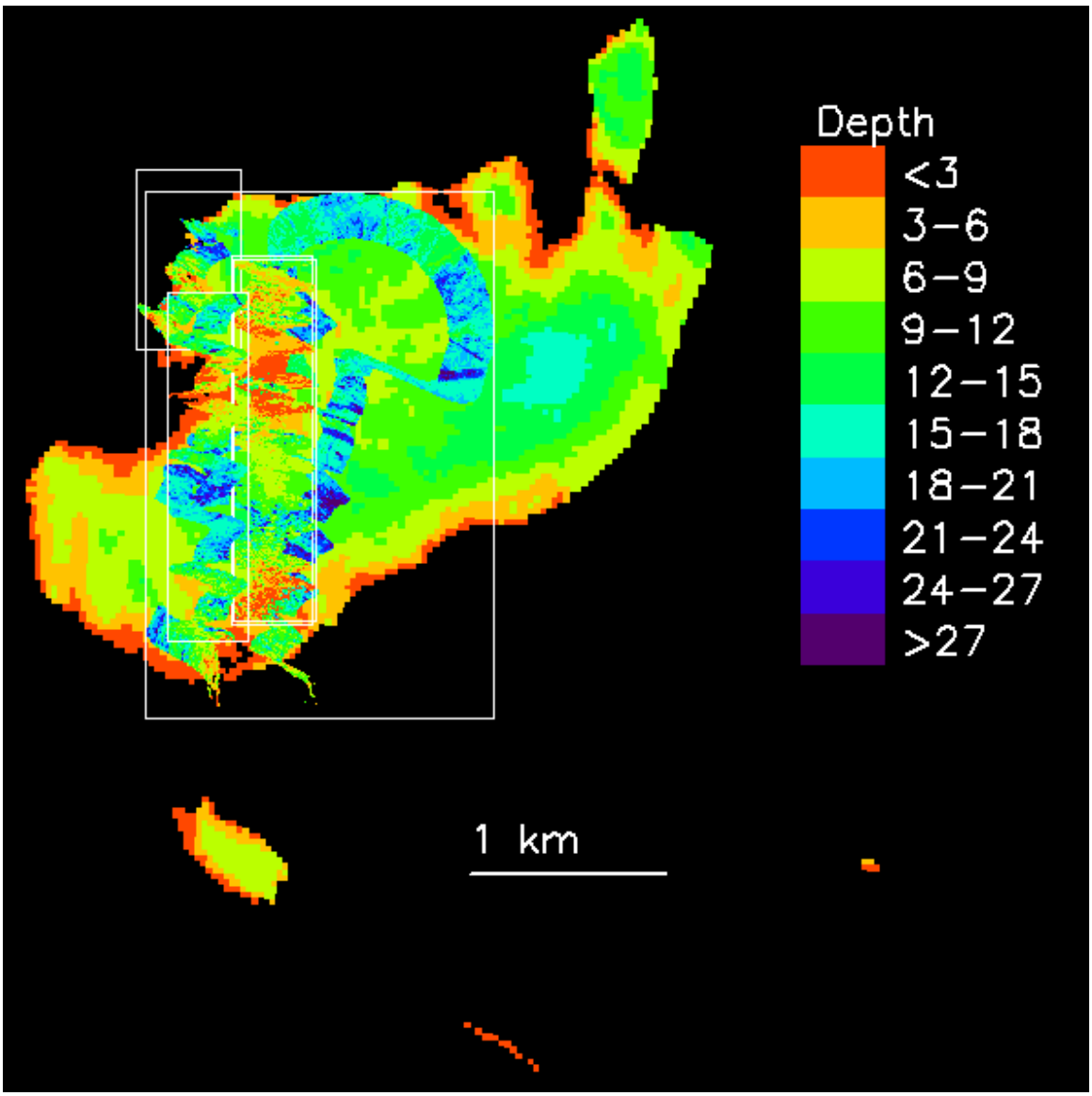

Figure 48: Overlaid lake depth calculations using Beer's Law on channel nine.

The precision of the lake depth results from Beer's law are investigated in figure 49, which shows a histogram of the differences between arbitrarily selected depth results in the MUSCOX images and the average of the depth results of the surrounding pixels in the Landsat image. This figure indicates that the differences between the depth results from MUSCOX and Landsat varied widely. Additionally,

the depth error was calculated as the MUSCOX results minus the Landsat results, so the prevalence of positive depth errors indicates that the depths calculated using the MUSCOX images were generally larger than the Landsat depths, or that the actual volume of the lake was reduced between when it was imaged by MUSCOX and when it was imaged by Landsat.

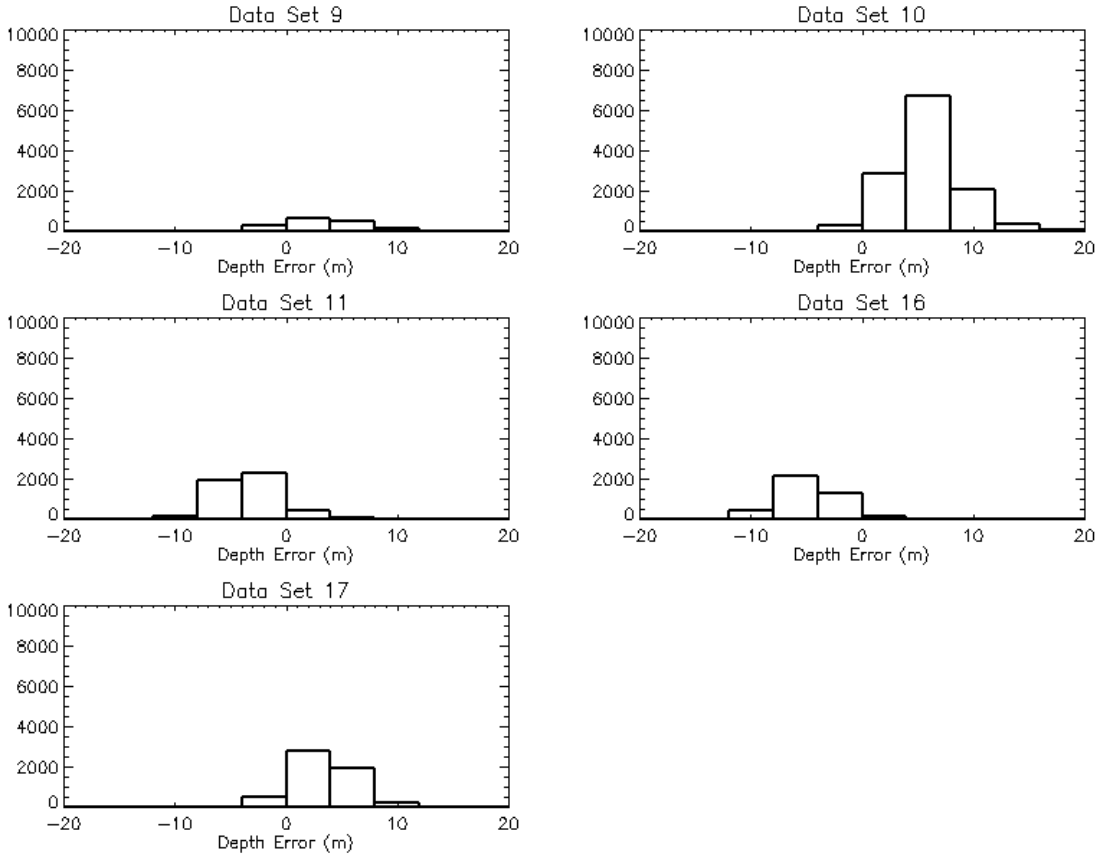

Figure 49: Histogram of the differences between the MUSCOX depth results and the corresponding Landsat depth results using Beer's Law on channel nine.

Table 17 gives the average and standard deviation of the depth errors shown in figure 49.

Table 17: Average and standard deviation of the errors in depth calculations using Beer's Law.

Data Set	Average Error (m)	Standard Deviation of Error (m)
9	3.56	3.62
10	5.83	3.04
11	-3.34	2.76
16	-4.75	2.78
17	3.41	2.63

Figure 50 shows the lake depths as imaged by Landsat on July 19th, and the MUSCOX mission, calculated using Beer's Law on channel 18.

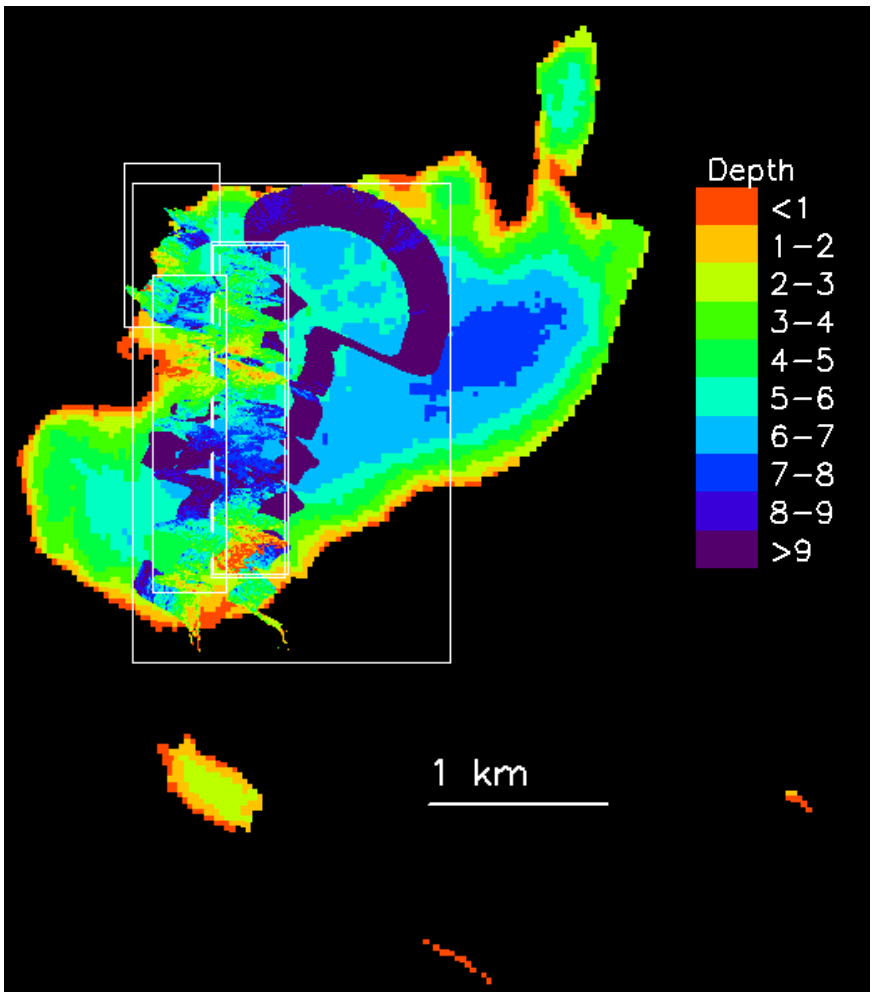

Figure 50: Overlaid depth calculations using Beer's Law on channel 18.

Figure 51 shows the histograms of the error in depth between arbitrarily selected water pixels in the MUSCOX images and the nearby pixels in the Landsat image.

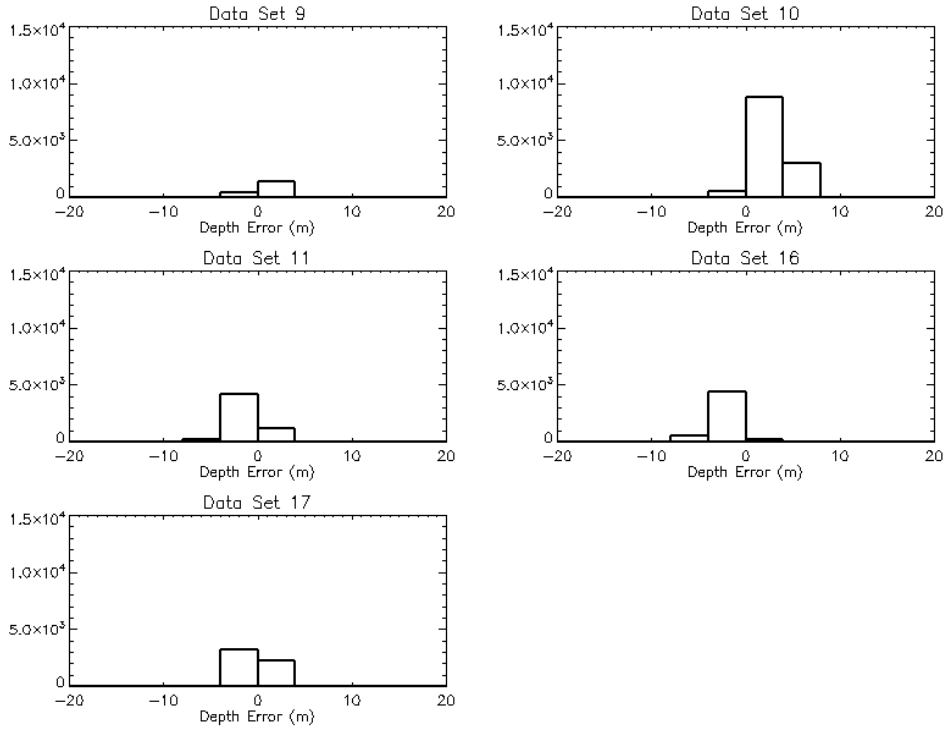

Figure 51: Histogram of errors in depth results as calculation using Beer's Law on channel 18.

Table 18 gives the average and standard deviation in the errors in depth shown in figure 51.

Table 18: Average and standard deviation of errors in depth results as calculated using Beer's Law on channel 18.

Data Set	Average Error (m)	Standard Deviation of Error (m)
9	0.87	1.24
10	2.94	1.57
11	-1.15	1.42
16	-2.18	1.35
17	-0.33	1.37

The depths of the lake imaged by the MUSCOX mission and Landsat 7 on July 19th, calculated using the ratio method, are shown in figure 52.

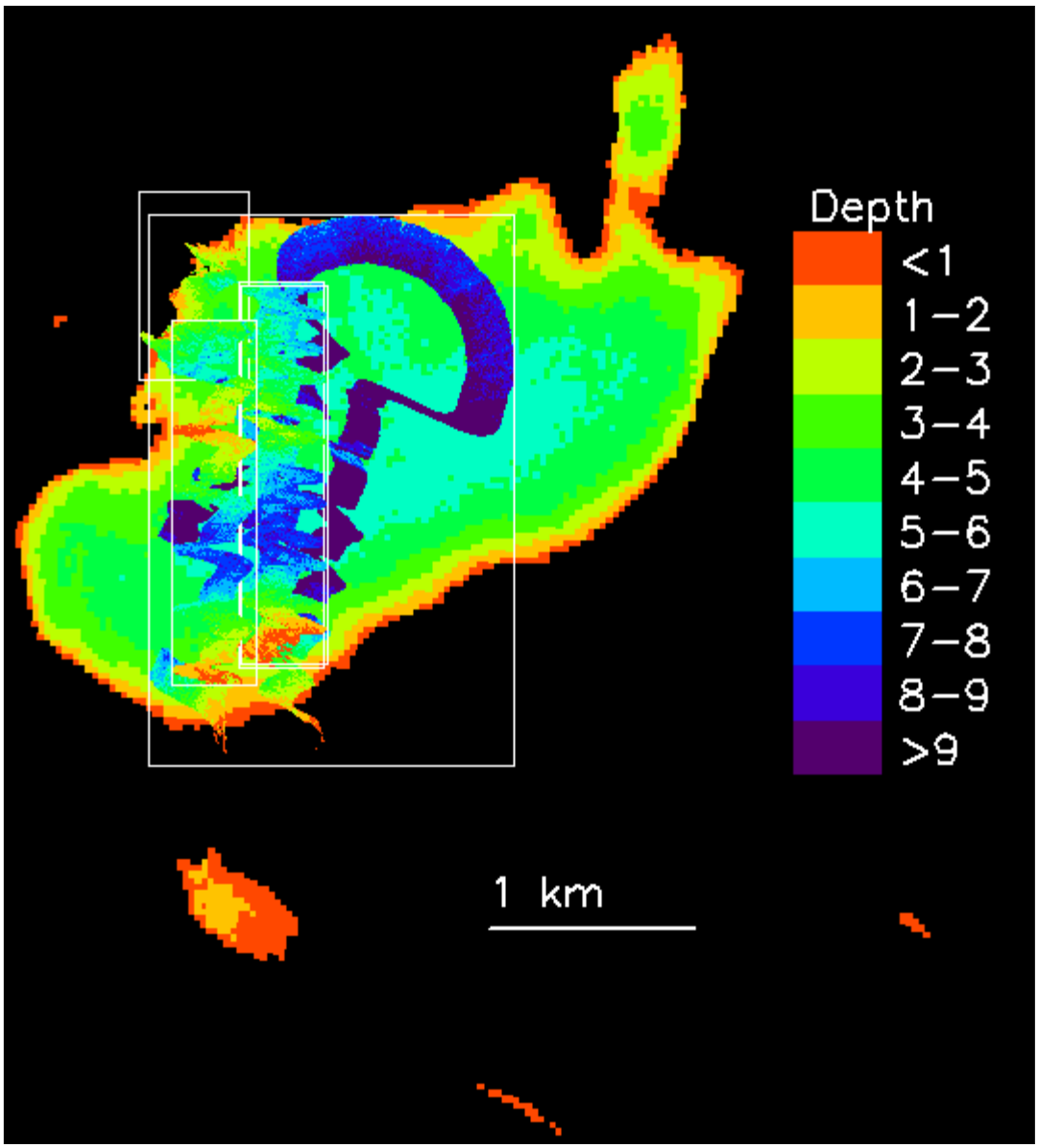

Figure 52: Results of depth calculation using the ratio method.

The histogram of the errors between the MUSCOX lake depths and the Landsat lake depths are given in figure 53.

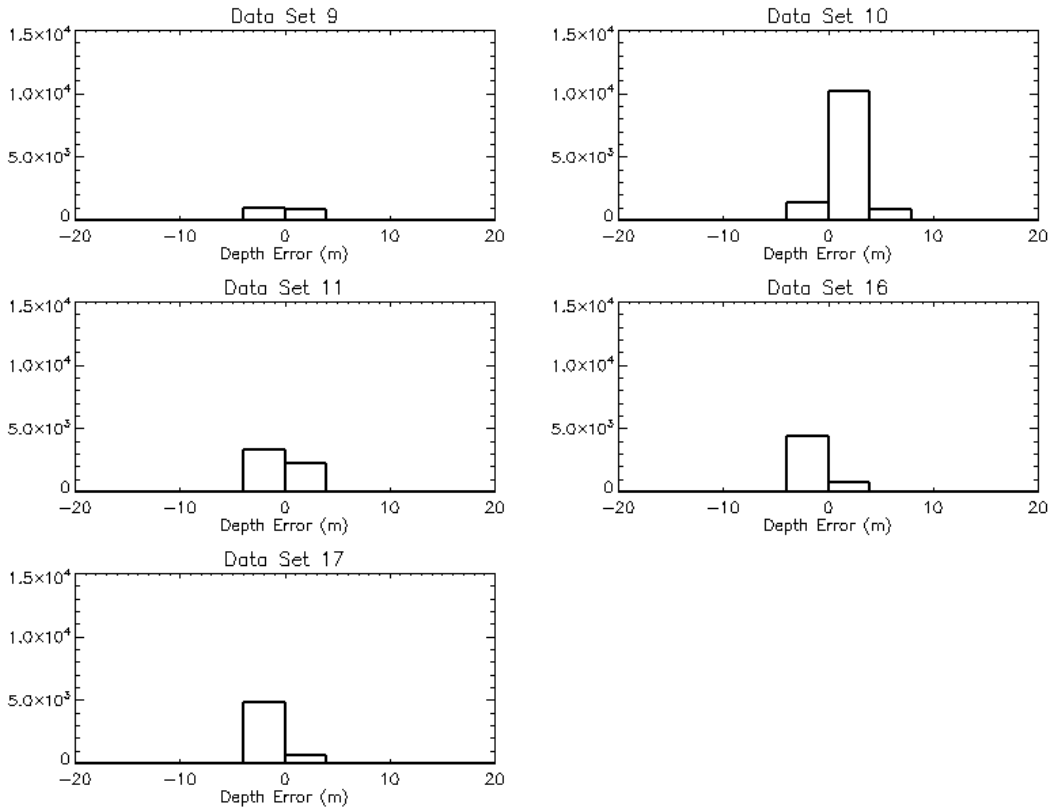

Figure 53: Histogram of errors in depth using the ratio method.

Table 19 gives the average and standard deviation of the errors in figure 53. These results indicate that the ratio method is significantly more precise than Beer's law when calculating lake depth in these images, though the question of which method is more accurate remains unanswered.

Table 19: Average and standard deviation in the errors in lake depth using the ratio method.

Data Set	Average Error (m)	Standard Deviation of Error (m)
9	-0.049	0.86
10	1.93	1.45
11	-0.43	1.25
16	-1.27	1.20
17	-1.55	1.18

B. Detection of Drained Supraglacial Lakes

The effort to detect drained supraglacial lakes begins with two images, taken by Landsat sixteen days apart. In the earlier image, taken on July 3, 2008 and shown with a depth map in figure 54, there are two visible supraglacial lakes. In the later image, taken on July 19, 2008, those lakes have drained. The average depth in the earlier image is 4.52 m, the maximum depth is 9.12 m, and the total volume of both lakes is $2.22 \cdot 10^7$ m^3, as calculated using Beer's law on the longer wavelength channel. It should be explained that the black lines which cross these images diagonally are strips of missing data due to the scan line corrector failure in the ETM+ instrument. No effort was made to interpolate across the gaps in the data left by the scan line corrector failure, so the area and volume results are slight underestimations of the actual areas and volumes of the lakes.

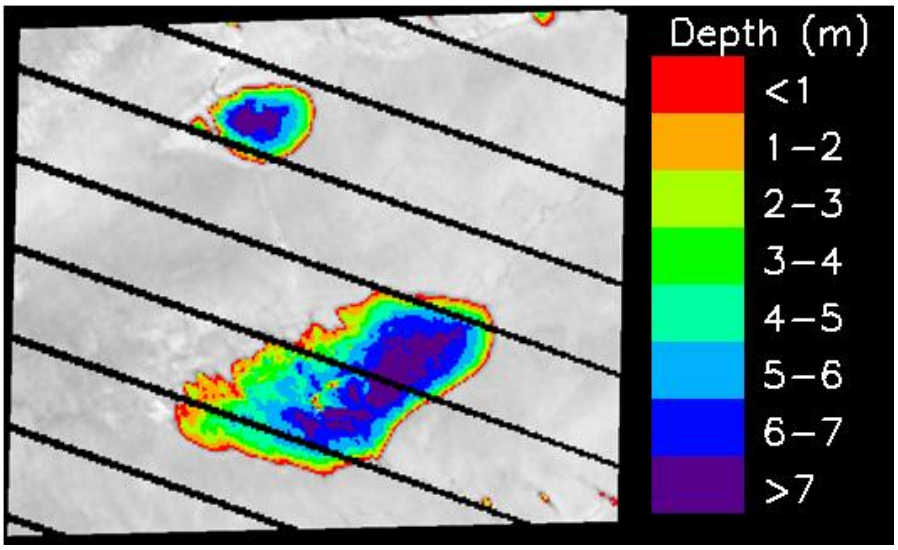

Figure 54: July 3rd image of the lakes which would drain by July 17th with calculated depths using Beer's law on channel 2 overlaid.

Applying the same classification algorithms used on the filled lake above to both images gives the results shown in figure 55.

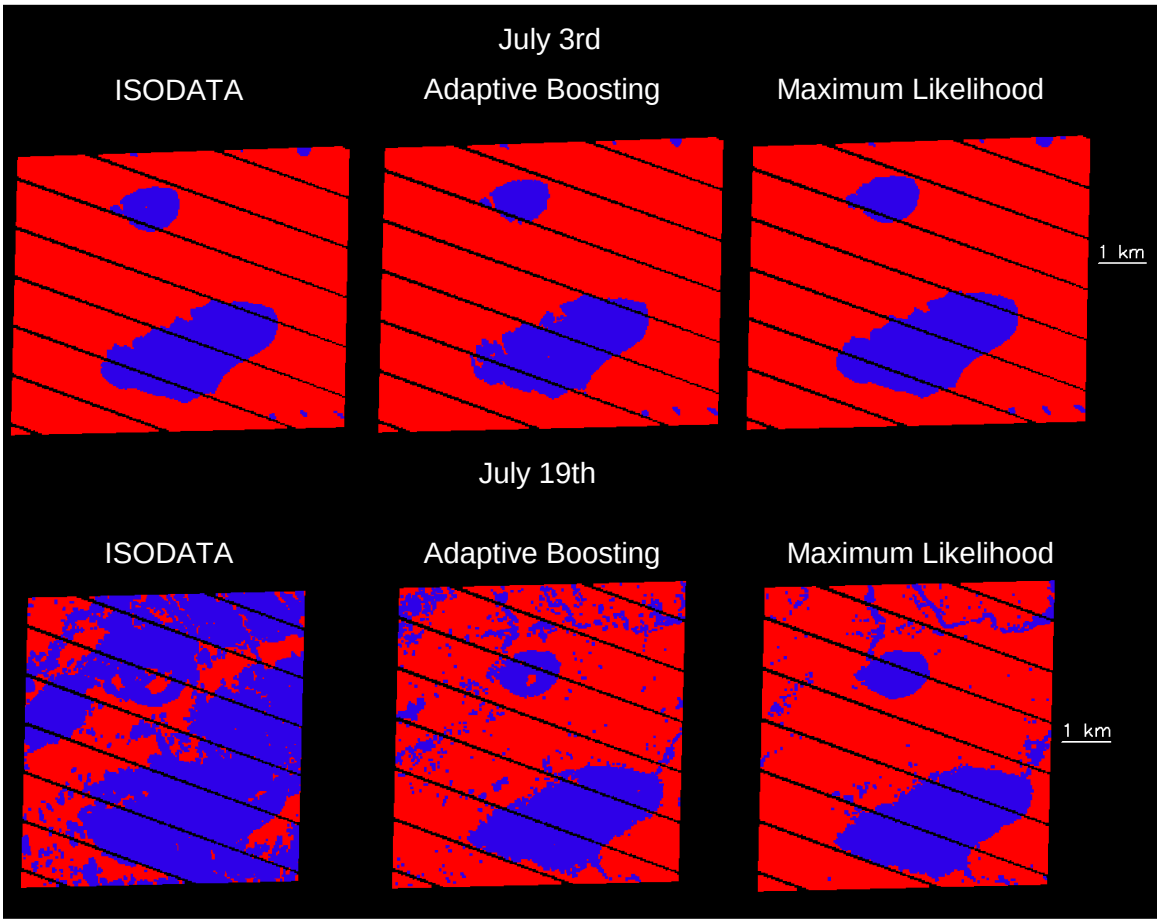

Figure 55: Results of classification algorithms on the same two lakes before and after they drained.

The quantitative results of the different classification algorithms are given in table 20. Clearly, in the case of the drained lakes, large differences exist between the results of the unsupervised algorithm, ISODATA, and the supervised algorithms, adaptive boosting and maximum likelihood. This is indicative of a failure in the ISODATA algorithm to isolate former lake pixels from the rest of the scene. The

other two algorithms, however, give lake areas which are comparable to the lake areas found with water present. The lake area found using adaptive boosting had a 34.27 % difference between the two images and the lake area found using maximum likelihood had a 19.91% difference between the two areas. These percent differences could be large enough to indicate a lack of accuracy in the drained lake results, however, the fact that the drained lake areas are also consistently larger than the filled lake areas could be an indication that the areas of the lakes had already contracted from their maximum values by the time the July 3rd image was taken, or that the classification algorithms detected supraglacial streams in addition to the lakes.

Table 20: Filled and drained lake areas from Landsat imagery.

Date	Lake Area (m^2)			% Difference from ISODATA	
	ISODATA	Adaptive Boosting	Maximum Likelihood	Adaptive Boosting	Maximum Likelihood
July 3	$5.04 \cdot 10^6$	$4.74 \cdot 10^6$	$5.33 \cdot 10^6$	6.11%	5.56%
July 19	$1.99 \cdot 10^7$	$6.70 \cdot 10^6$	$6.51 \cdot 10^6$	99.32%	101.54%

The most obvious question to ask next is what features the supervised algorithms discovered in their training data which allowed them to successfully distinguish between former lake locations and locations where there had never been a supraglacial lake. Since the maximum likelihood algorithm classifies data by grouping pixels with similar spectral signatures together, its classification rules contain only limited information about the specific features of the spectral signatures that caused it to place a pixel in one class or another. Adaptive boosting, however, functions by determining a series of thresholds in the spectral data which it uses to classify the data. These thresholds are shown in figure 56 along with the observed

spectral values of the two ground types. Averaging together the various thresholds for each observing channel, adaptive boosting determined that a pixel is the location of a former lake if the value in channel 1 is above 0.86, channel 2 is above 0.75, channel 3 is below 0.78, channel 4 is below 0.39, channel 5 is above 0.05, and channel 6 is above 0.04. This summary is not exact because it ignores the input of multiple thresholds with different weights applied to the same channel, but it shows that, in general, adaptive boosting determined that pixels where water used to be located is more reflective in short and long wavelengths (below 601 nm and above 1550 nm) and less reflective in the mid wavelengths than locations where there was never liquid water.

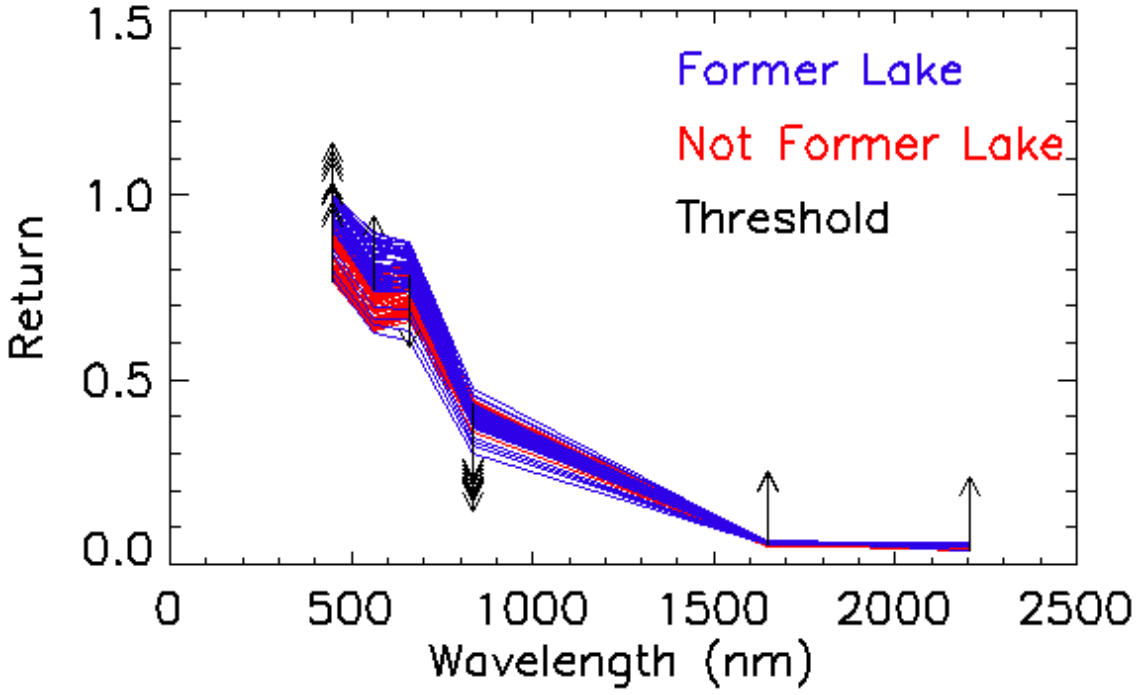

Figure 56: Sample former lake and not former lake spectral signatures and threshold values as determined by adaptive boosting.

To test the usefulness of the trends found in figure 56, figure 57 shows grayscale images of the drained lake scene using ratios of bands one through four with the hypothesis that the relative reflectivities of the pixels which have and have not been the site of liquid water can be used to determine the locations of former lakes. Inclusion of the (channel 1)/(channel 4) and (channel 4)/(channel 2) ratios in the training data given to adaptive boosting changes the result slightly, reducing the estimated lake area to $6.27 \cdot 10^6$ m^2, which is a percent difference of 27.74% from the adaptive boosting classification results of the image with filled lakes, an improvement of 6.53% from the adaptive boosting results without the ratio data.

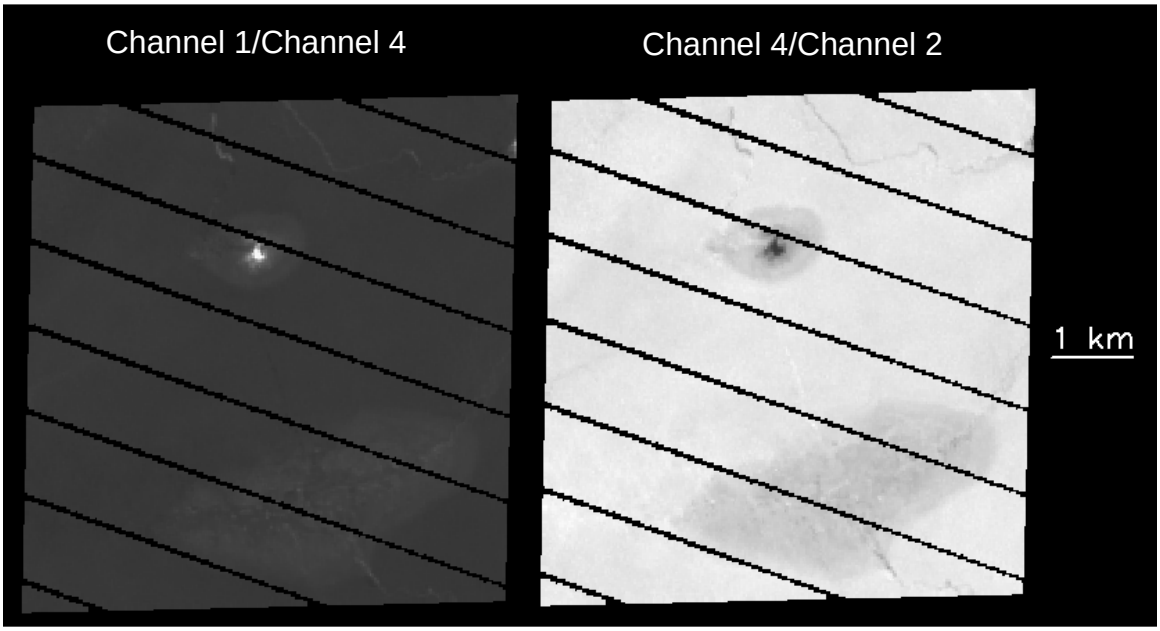

Figure 57: Drained lake images plotting using ratios of spectral data.

Figure 58 shows the spectral data from the drained lake image versus the depth data from the filled lake image which corresponds in location. Clearly, there is not a strong correlation between the reflectivity of the ice at the location of a drained

lake and the depth of the former lake. This is confirmed in table 21, which gives the correlation coefficient between depth and the spectral data of former lake pixels, including the two band ratios investigated in figure 58.

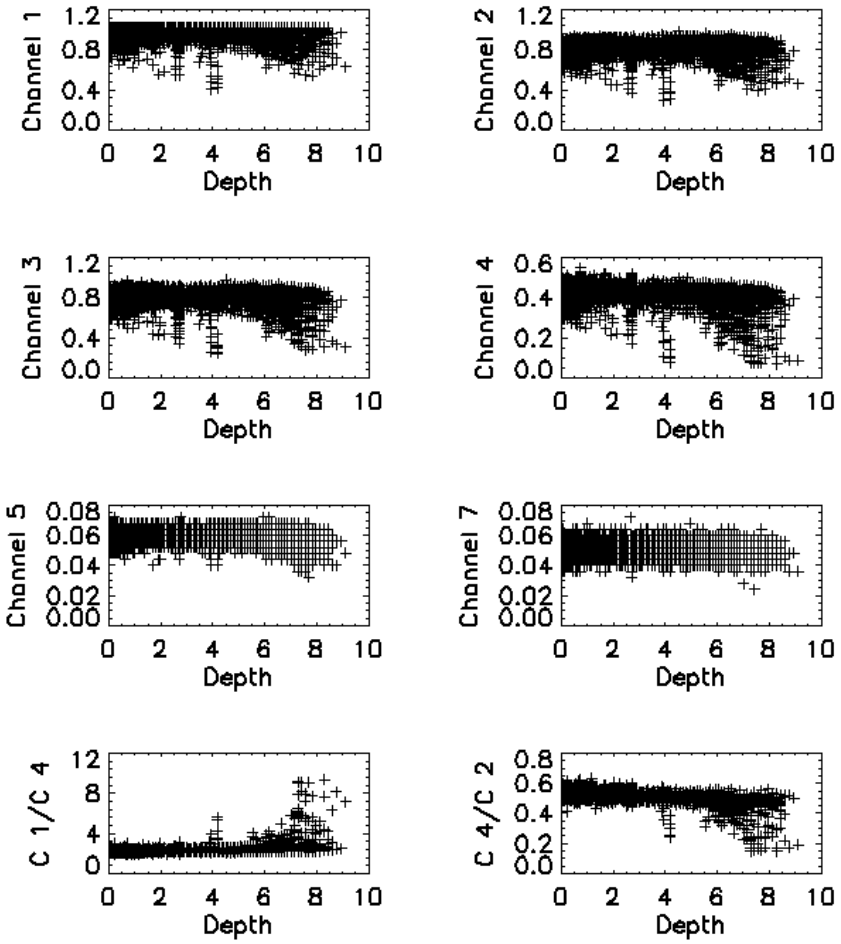

Figure 58: Scatterplot of drained lake spectral data versus filled lake depth.

In table 21, the strongest correlations are indicated between depth and the band ratios; however, investigation of figure 58 shows that there is only a large difference in the band ratios at the largest depths. Thus, these band ratios could be of

possible use in locating former lakes, but would be less valuable in determining the extent of the lakes.

Table 21: Correlation between filled lake depth and drained lake spectral data.

Channel	Correlation Coefficient
1	0.17
2	0.15
3	-0.028
4	-0.24
5	0.00046
7	-0.014
1/4	0.33
4/2	-0.58

There is the additional possibility that the presence of liquid water on top of an ice shelf will affect other parameters than reflectivity. As discussed above, liquid water has a lower albedo than ice, meaning that it absorbs more incident radiation, which increases its temperature. Since nature seeks equilibrium, this increase in heat is transferred from the water to the surrounding ice through convection and conduction, which will increase the temperature of the ice and cause it to melt. The ice which is left behind after the surrounding ice is melted due to contact with liquid water could have a different texture than ice which has not melted since its formation, a possibility which will be investigated using three images gathered by the MUSCOX mission, shown in figure 59. These images correspond to data sets 20, 21, and 22 as given in table 23 and are located in the middle of a drained glacial lake, on unaltered ice, and on the edge of a drained glacial lake, containing both drained lake and bare ice pixels, respectively.

Data Set 20

Data Set 21

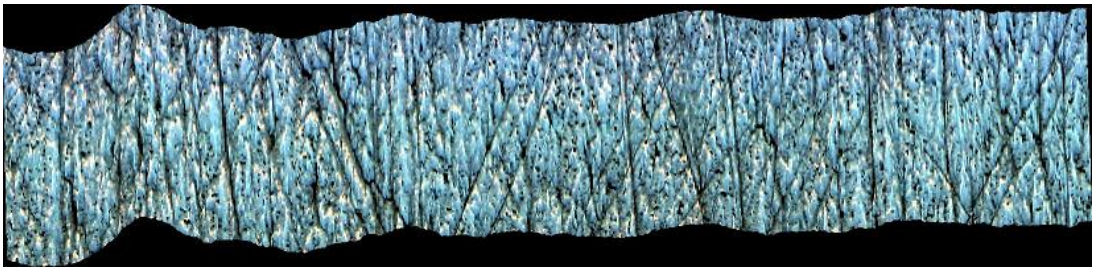

Data Set 23

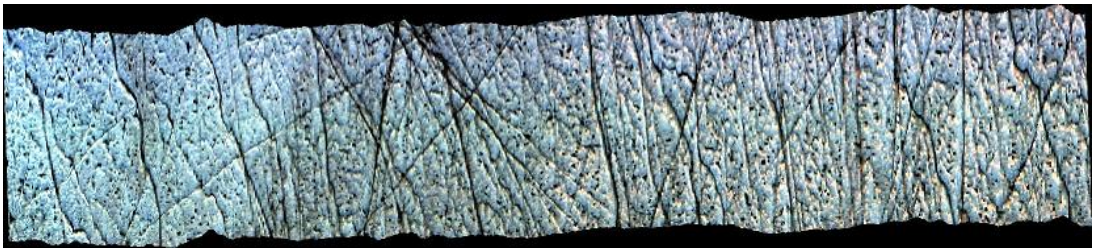

Figure 59: Drained lake, bare ice, and combination MUSCOX data sets.

The notion that the presence of water changes the texture of the ice on which it is located is confirmed in figure 60 which shows the results of a co-occurrence analysis on data set 23. The co-occurrence analysis used a shifting three by three matrix of pixels to compute several statistical parameters. The output parameters of variance, contrast, and dissimilarity were chosen to be shown here because they show the largest differences between drained lake pixels and bare ice pixels. As figure 60 indicates, the presence of water does change the texture of the ice which is left behind

when it drains, slightly decreasing the variance, contrast, and dissimilarity of the ice at wavelengths between approximately 600 and 800 nm.

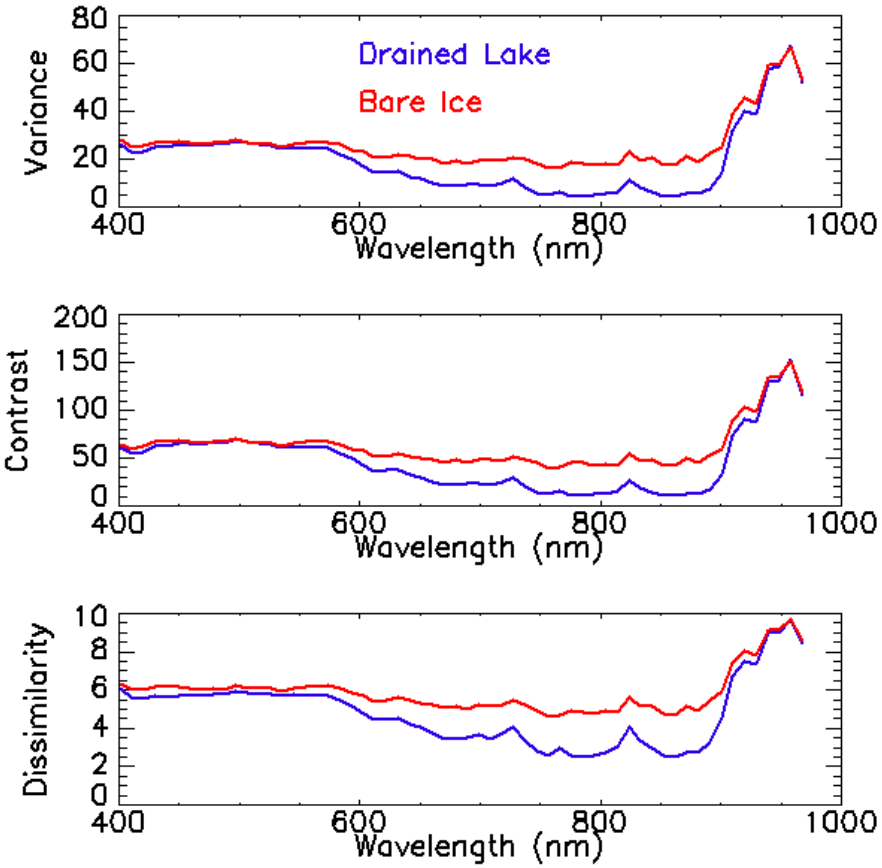

Figure 60: Results of a co-occurrence analysis on data set 23.

Figure 61 shows the results of applying maximum likelihood to the raw spectral data and to the texture data in MUSCOX data set 23. As this figure shows, the results from the texture analysis found a larger former lake area and has more clearly marked boundaries between former lake and unaltered ice. It is unknown which result is more accurate. The results from the raw data appear to match better with the lake boundaries in the July 3rd Landsat image, but it is possible that the

Landsat image was taken after the size of the lake had contracted from its maximum value.

Maximum likelihood on raw data

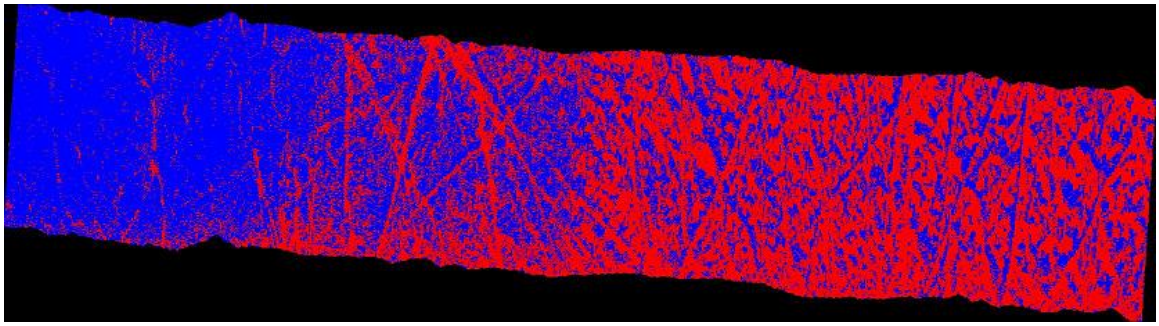

Maximum likelihood on texture data

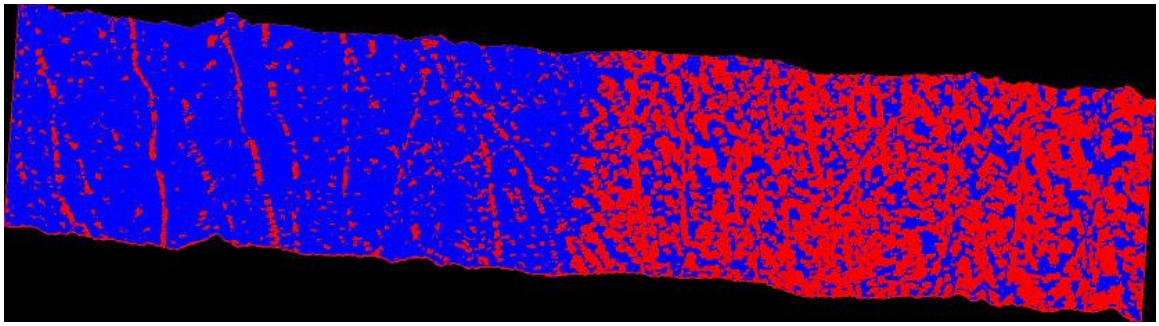

Figure 61: Results of applying maximum likelihood to the raw data and the texture data of MUSCOX data set 23.

The trend that the presence of liquid water on an ice shelf changes the texture of the ice is continued in figure 62, which shows the results of an identical co-occurrence analysis on MUSCOX data set 20, which is located entirely within a drained supraglacial lake, and data set 21, which consists of unaltered ice. Comparison of figures 60 and 62 indicates that the exact nature of the texture of the unaltered ice and the way that the texture is modified by the presence of liquid water is not constant, but the texture of ice is nevertheless changed by melt ponds, and that

change is detectable. The most likely reason for the lack of absolute "texture signatures" in the data is the fact that ice is a natural ground type, subject to variations due to various factors, such as wind during its formation and movement of the ice itself.

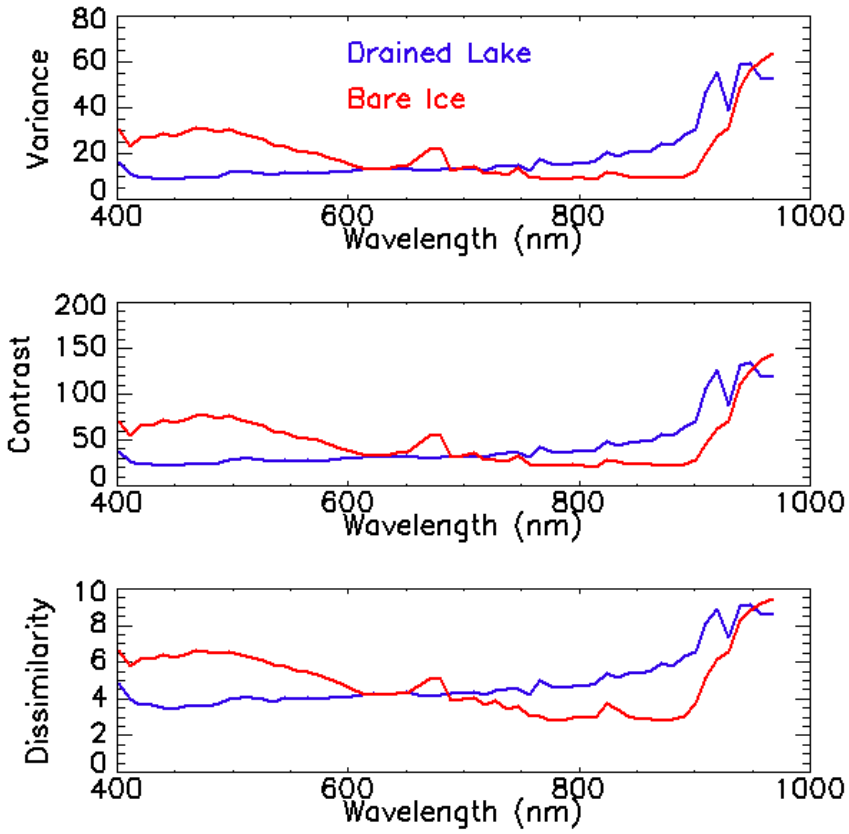

Figure 62: Results of a co-occurrence analysis on data sets 20 and 21.

C. Frequency of Supraglacial Lake Occurrence

Landsat 7 images of the Greenland Ice Sheet during the melt seasons of 2007, 2008, and 2009 are shown in figure 63. These images were selected from all the data gathered between April and October of those years for lack of cloud cover. They were also subsetted to include only the center strip of the images, attempting to avoid

gaps in the data due to the scan line corrector failure.

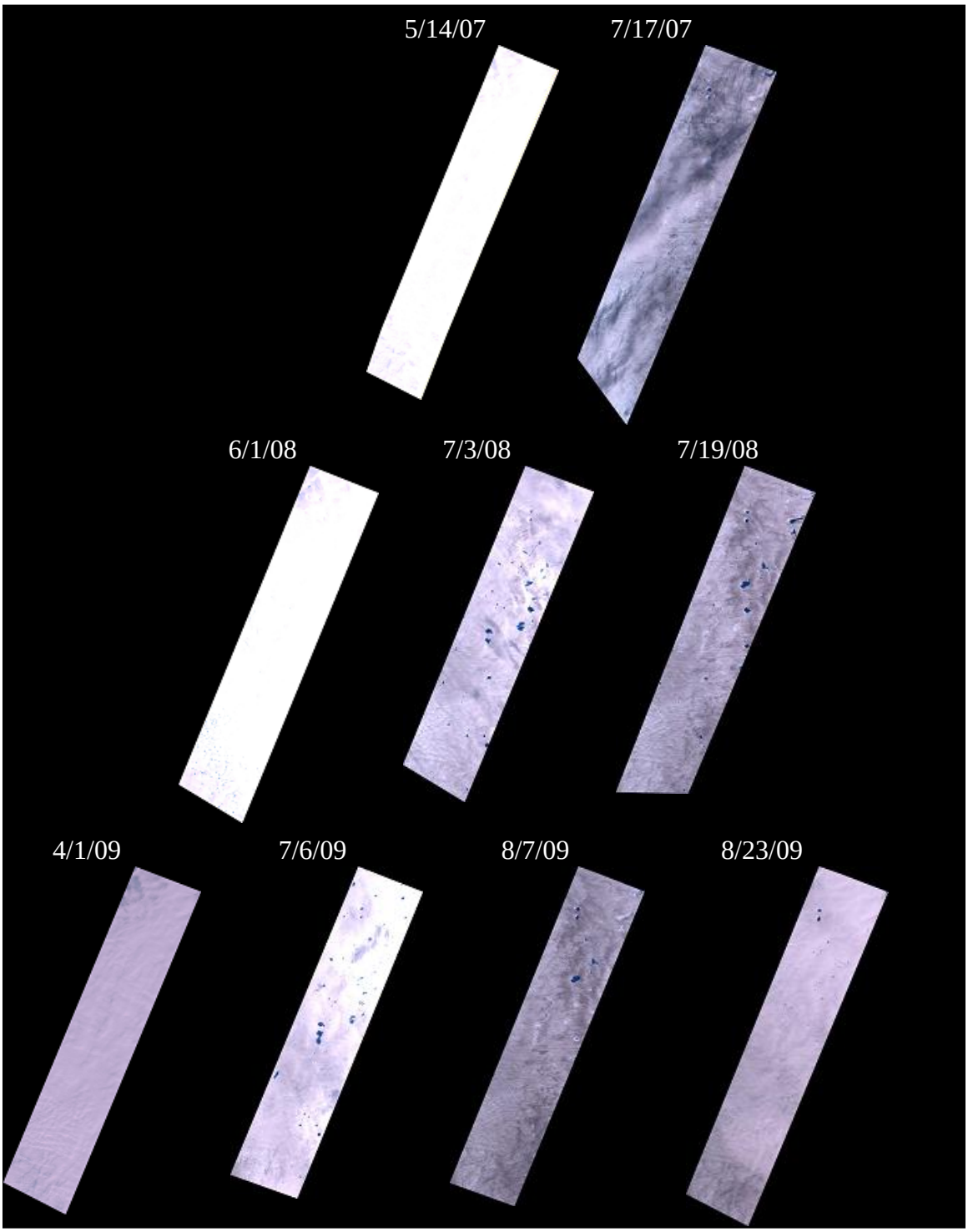

Figure 63: True color Landsat 7 images of the Greenland Ice Sheet in 2007, 2008, and 2009.

Figure 64 gives the results of ground classification through maximum likelihood for the same data sets. Data sets which did not include any supraglacial lakes were not included in this figure.

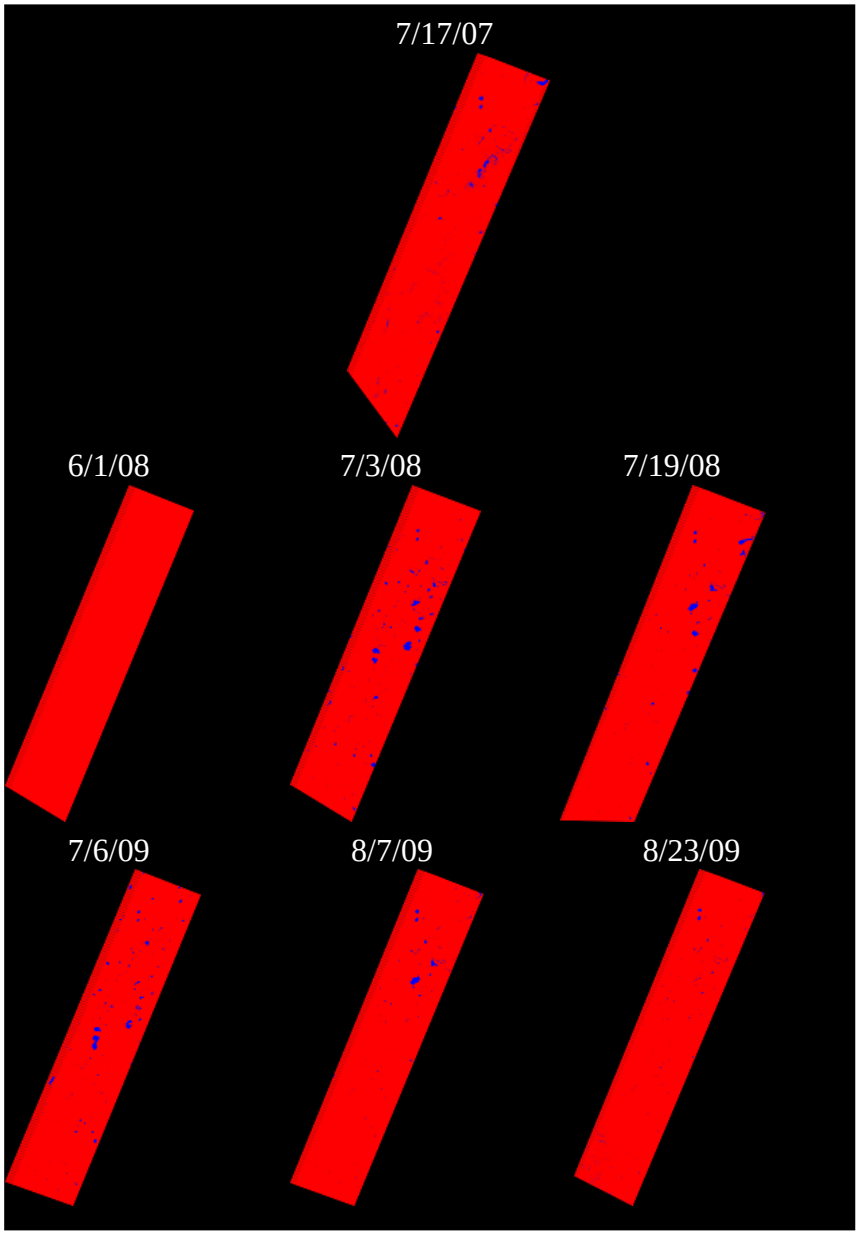

Figure 64: Results of maximum likelihood classification on Landsat images of the Greenland Ice Sheet from 2007, 2008, and 2009.

The total area of each image and the area of the image where liquid water was located are given in table 22, along with an approximate tally of the number of individual lakes. Efforts to calculate the depths of the lakes using Beer's law and the ratio method used above produced an excessive number of invalid results, meaning negative calculated depth results, indicating that the assumptions discussed in the preprocessing section, while valid for a small region of an image, begin to break down for the larger areas in the images discussed here. Thus, no lake depths will be reported here and the task of calculating lake depth over a wide area of the Greenland Ice Sheet will be left for future work.

Table 22: Quantitative results of maximum likelihood on Landsat images of the Greenland Ice Sheet from 2007, 2008, and 2009.

Date	Image Area (km^2)	Lake Area (km^2)	% Lake Area (%)	Number of Lakes
5/14/07	2913.99	0	0	0
7/17/07	3397.35	37.38	1.10	18
6/1/08	3176.18	0	0	0
7/3/08	2935.95	47.44	1.62	42
7/19/08	3013.27	31.57	1.05	21
4/1/09	3208.69	0	0	0
7/6/09	3083.02	40.63	1.32	32
8/7/09	3160.96	22.08	0.70	8
8/23/09	3114.57	12.88	0.41	3

The number of lakes and percentage of image area covered in lakes over time is shown in figure 65, combining data from all three study years. These results echo the findings of *Sundal et. al.* (2009) which found that supraglacial lake coverage in Greenland tends to peak between the 180th and 220th day of the year (June 29th to August 8th in non-leap years).

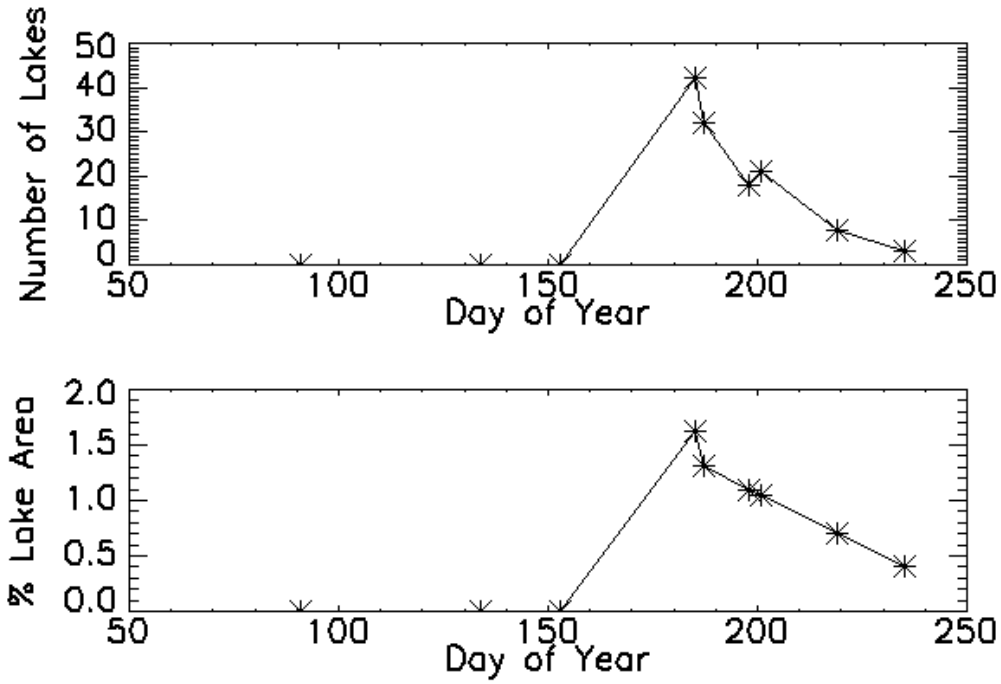

Figure 65: Number of lakes and percent lake area versus time.

Figure 66 was produced by adding the band math channels of band one over band four and band four over band two to the raw data in the Landsat images and using maximum likelihood to determine the locations of the filled and drained lakes. Only images which were likely to contain drained lakes were included in this analysis. The criterion used to determine which images were likely to include drained lakes were time of year and whether or not an image which was recorded earlier in that same year contained filled lakes. Though these results contain several obvious places where the predicted drained lake has a much larger area than might be expected, the drained lake results also highlight many former lakes and streams, providing a level of detail which was not possible in the raw data analysis alone.

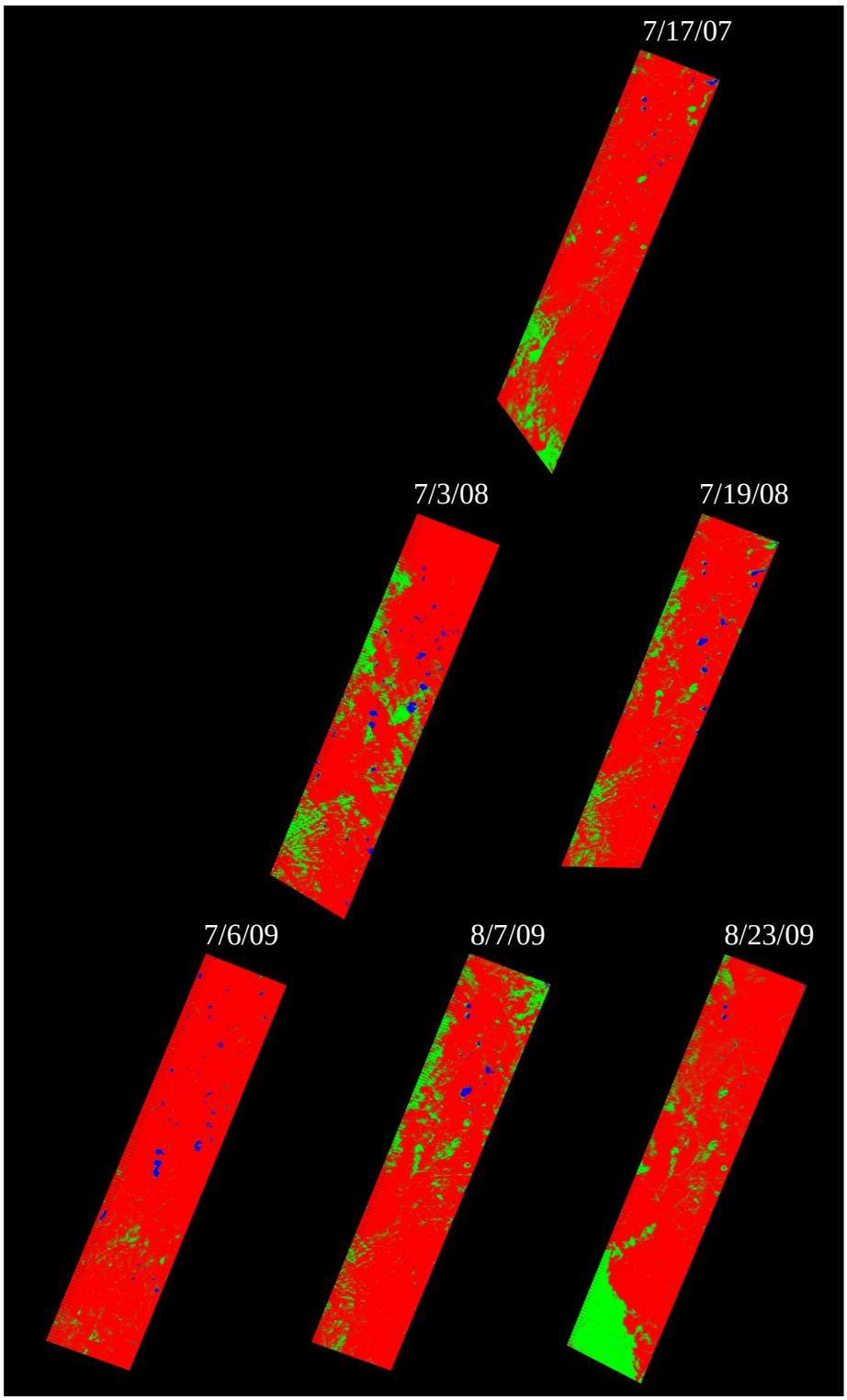

Figure 66: Results of the maximum likelihood algorithm applied to the raw and band math data from Landsat 7 in 2007, 2008, and 2009, searching for filled and drained lakes.

Table 23 gives the quantitative filled and drained lake areas in these images. The use of additional training data for the drained lakes changed the filled lake results as well as adding the drained lake results. This is because the additional training data changes the parameters of the discriminant function in the maximum likelihood algorithm.

Table 23: Quantitative results of maximum likelihood on Landsat images including band math, searching for filled and drained lakes.

Date	Image Area (km^2)	Filled Lake Area (km^2)	% Filled Lake Area (%)	Drained Lake Area (km^2)	% Drained Lake Area (%)
5/14/07	2913.99	0	0	0	0
7/17/07	3397.35	17.71	0.52	338.35	9.96
6/1/08	3176.18	0	0	0	0
7/3/08	2935.95	48.64	1.66	422.44	14.39
7/19/08	3013.27	32.10	1.07	307.35	10.20
4/1/09	3208.69	0	0	0	0
7/6/09	3083.02	36.82	1.19	79.15	2.57
8/7/09	3160.96	22.15	0.70	402.11	12.72
8/23/09	3114.57	8.88	0.29	574.14	18.43

The change in filled and drained lake area versus day of year for all images is given in figure 67. As this figure indicates, though there is a significant amount of uncertainty in the drained lake results, the general trend that the percent of total area covered by drained lakes increases throughout the melt season is consistent with the fact that lakes fill then drain throughout the summer.

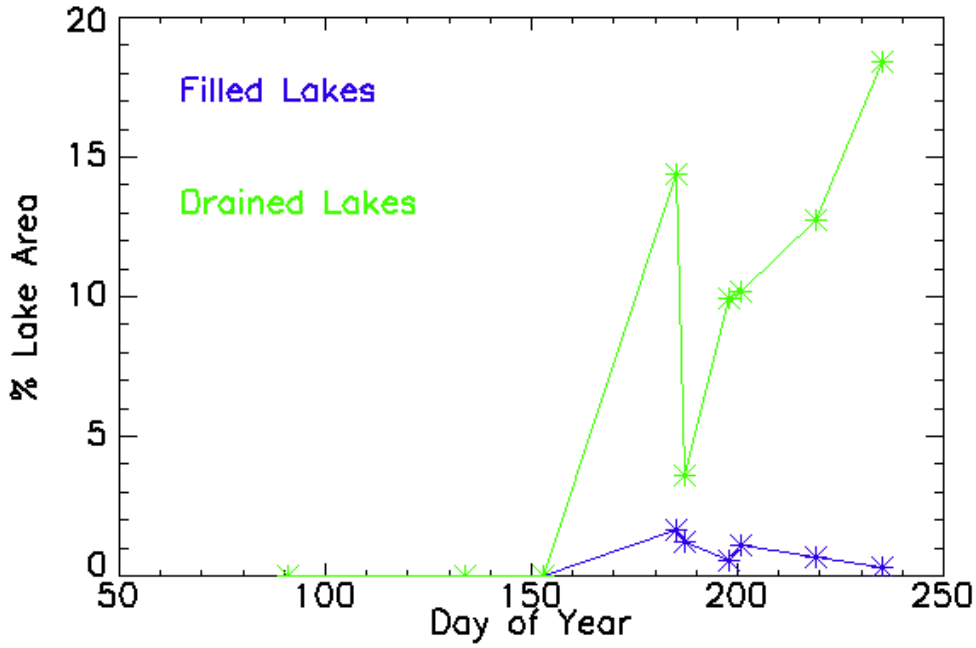

Figure 67: Percent filled and drained lake area over time.

Expanding the texture analysis performed on former lake images from the MUSOX mission above, figure 68 shows the results of a texture analysis on a former lake in the Landsat image from July 19, 2008 along with an analysis of the raw data in the image for comparison. Clearly, any modifications which liquid water makes to the texture of the surrounding ice is not visible in this Landsat 7 data.

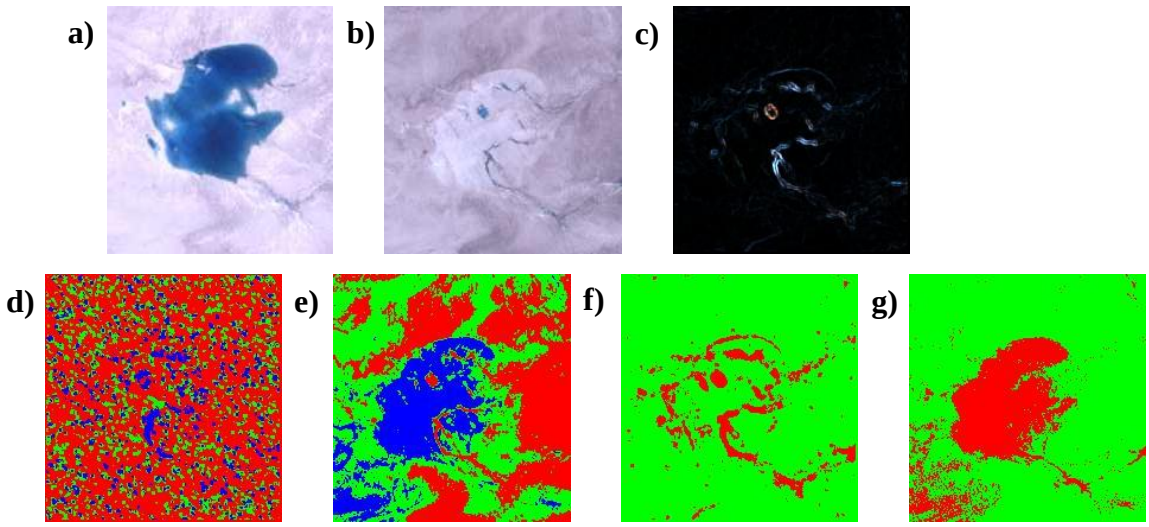

Figure 68: Texture analysis of a drained lake imaged by Landsat 7. a) The lake on July 3, 2008, before it drained. b) The same location on July 19, 2008, after it had drained. c) The variance in bands one (blue), two (green), and three (red). d) The results of ISODATA on the variance, contrast, and dissimilarity texture data. e) The results of ISODATA on the raw data. f) The results of maximum likelihood on the texture data. g) The results of maximum likelihood on the raw data.

The lack of accurate results from the texture analysis is in contrast to the outcome of investigation on texture in the MUSCOX images of drained lakes, which showed that there are visible differences in variance, contrast, and dissimilarity between drained lake ice and unaltered ice. The most likely reason for this is the differences in the spatial resolutions of the two instruments. The spatial resolution of the MUSCOX instrument depends upon the altitude of the UAV, but is generally approximately 30 cm for the ice observations, whereas the resolution of the ETM+ is 30 meters in the observing bands used for this analysis. It is possible that any modifications that liquid water makes to the texture of ice is on so fine a scale as to make it undetectable by an instrument with 30 meter spatial resolution. The prudent next step would be to attempt to confirm or refute this hypothesis through lab or field

experiments, but that effort is left up to future researchers.

VI. Conclusion

The volume and frequency of supraglacial lakes are affected by incoming radiation from the sun and the temperature of the ice on which they form. The occurrence of glacial lakes can lead to additional lakes because of a positive feedback loop created because water absorbs more radiation than ice. As a result, an increased frequency of and volume glacial lakes can be a symptom of global climate change. The lakes are a valuable parameter in the mass budget of the cryosphere and a useful proxy for measuring climate change. Therefore, monitoring glacial lakes with high spatial and temporal resolution is important to increasing scientific understanding of the cryosphere and the Earth climate system as a whole.

This report documented the analysis of hyperspectral data with very high spatial resolution of melt ponds on a glacier near the southwest coast of Greenland. The data were mined for the locations of the ponds using three different algorithms: Iterative Self-Organizing Data Analysis Technique, adaptive boosting, and the maximum likelihood algorithm. Once the water pixels were located, the depth of the water was calculated using Beer's Law and a modification of Beer's law using two observing bands, and the volume of the lakes was determined.

Examination of the results of the ground categorization algorithms showed that the accuracy of the outcome is highly dependent upon the quality of the input data. This fact dictates that training data for the adaptive boosting and maximum likelihood algorithms must be chosen to represent all subtypes of data within each

data class, so that the algorithm will, for example, classify shallow water as water instead of ice. It also casts doubt upon the accuracy of the unsupervised algorithm ISODATA, which can only be modified through statistical thresholds. As a result, ISODATA was used only for comparison with the other two algorithms. Contrasting the lake boundaries found when the two supervised algorithms were applied to MUSCOX data to the results of the same ground classification techniques on coincident data gathered by Landsat 7 showed that the results are generally accurate, with the boundaries matching to within about 300 meters, which is an acceptable level of error considering that the observations were not coincident in time and the boundaries of supraglacial lakes can change rapidly, and given that the Landsat data has 30 meter resolution.

Attempts to determine the depths of the lakes were complicated by a wavelength dependent attribute of the water or lake bottom which the simple attenuation coefficient of pure water does not account for. As a result, the depth calculations produced different results depending upon which observing channel was used in the calculation. This effect was particularly prevalent in the depths found using Beer's law; the ratio method was slightly more stable. Analysis of Landsat data from July 19, 2008, using the ratio method, indicates that the filled lake had a volume of $2.28 \cdot 10^7$ m^3. Though the ratio method is less sensitive to variations in lake bottom reflectivity and attenuation coefficient and therefore likely to be more accurate than Beer's law, the absolute accuracy of these results is unknown.

The analysis then moved to the images of drained supraglacial lakes which

were imaged by both MUSCOX and Landsat 7. Investigation into this data revealed minimal differences in the spectral data between ice which had been the location of a supraglacial lake and unaltered ice, but slight changes in the texture of the ice was detected in the MUSCOX data. An identical texture analysis on the Landsat data did not reveal the same changes, indicating that the alterations to the texture of the ice are not visible to instruments with a 30 meter spatial resolution. Further analysis is required to determine if texture analysis is a viable method of determining the locations of drained supraglacial lakes and whether the texture data can be used to determine the depth of the former lake and how long before the observation the lake drained. Analysis also showed that adding band ratio data to the ground classification algorithms can improve the estimates of supraglacial lake locations, but no significant correlation between spectral or band ratio data and former lake depth was detected. However, both texture analysis and band ratio analysis have the potential to provide a useful supplement to the change detection method of locating drained supraglacial lakes because they could be used to find drained lakes even if the lake was never imaged while full.

Finally, a low level analysis on Landsat data during the summers of 2007, 2008, and 2009 showed the seasonal trends in lake occurrence, indicating that the number and total areas of lakes on the Greenland Ice Sheet increase until approximately midsummer then begin to drain or freeze as winter approaches. The sample size in the analysis was not large enough to draw any conclusions about year to year trends in the frequency or size of supraglacial lakes.

A. *Advantages and Disadvantages of Imagery Recorded by a UAV*

Since the MUSCOX mission was a proof of concept for the use of UAVs in imaging the ice sheet, this section will list some advantages and disadvantages of the practice, from the perspective of the individual analyzing the data.

Some of the advantages of working with the MUSCOX data are as follows:

- The very high spatial resolution imagery allowed for very accurate results in calculated lake area and volume.
- The high spatial resolution allowed for texture analysis which was not possible in lower resolution data.
- The high spectral resolution allows for more accurate matching of spectral signatures.

Some of the disadvantages of working with the MUSCOX data are as follows:

- No single data set imaged an entire lake.
- The maneuvers of the aircraft meant that the spatial resolution of each pixel had to be calculated separately.
- No single data set included both lake data and the deep water data useful in calculating water depth.

B. *Avenues for Future Work*

There are several ways in which this project could be expanded and continued, such as the following:

- Classify the images using an algorithm which uses the fact that neighboring pixels are statistically more likely to have the same ground type.

- Perform laboratory or field experiments on the effect of liquid water on ice, paying particular attention to the changes in reflectivity and texture.
- Investigate the possibility of suspended or settled sediment in supraglacial lakes affecting the depth calculations by taking samples of actual lakes in Greenland and testing the attenuation coefficient of that water.
- Investigate the effect of ice crystals on lakes to determine if their presence changes the reflectivity of the lake in a way that alters the results of depth calculations by performing laboratory experiments.
- Repeat the experiment with in situ depth measurements of the lakes that are imaged by the UAV.
- Expand the analysis of the long term data of the Greenland Ice Sheet, looking for information about the water budget of the area, which can be added to the climate model of the Earth and provide valuable information concerning the theory of global climate change.

VII. Bibliography

Bindschadler, R.A., Scambos, T.A., Choi, H., Haran, T.M. "Ice sheet change detection by satellite image differencing." *Remote Sensing of Environment*, Vol. 114, No. 7, pp. 1353-1362, 15 July 2010.

Boulton, G.S. "Glaciers and their coupling with hydraulic and sedimentary processes." *Glacier Science and Environmental Change*, edited by Peter G. Knight. Black Science Ltd., Carlton, Victoria, Australia, 2006, pp. 3-22.

Box, J.E., and Ski, K. "Remote sounding of Greenland supraglacial melt lakes: implications for subglacial hydraulics." *Journal of Glaciology*, Vol. 53, No. 181, pp. 257-265, 2007.

CRC Handbook of Chemistry and Physics, 91st Edition, Internet Version 2011. Ed. W.M. Haynes. [online resource]. URL: http://www.hbcpnetbase.com [cited: 14 February 2011].

Das, S.B., Joughin, I., Behn, M.D., Howal, I.M, King, M.A., Lizarralde, D., and Bhatia, M.P. "Fracture Propagation to the Base of the Greenland Ice Sheet During Supraglacial Lake Drainage." *Science*, Vol. 320, No. 5877, pp. 778-781, 9 May 2008. URL: http://www.sciencemag.org/content/320/5877/778.full
doi: 10.1126

Earth Observing System Data and Information System (EOSDIS). 2009. Earth Observing System ClearingHOuse (ECHO) / Warehouse Inventory Search Tool (WIST) Version 10.X [online application]. Greenbelt, MD: EOSDIS, Goddard Space Flight Center (GSFC) National Aeronautics and Space Administration (NASA). URL: https://wist.echo.nasa.gov/api/

Eicken, H., Grenfell, T.C., Perovich, D.K., Richter-Menge, J.A., Frey, K. "Hydraulic controls of summer Arctic pack ice albedo." *Journal of Geophysical Research*, Vol. 109, No. C8, 15 August 2004.
doi: 10.1029

Freund, Y. and Schapire, R.E. "A Decision-Theoretic Generalization of On-Line Learning and an Application to Boosting." *Journal of Computer and System Sciences*, Vol. 55, pp. 119-139, August 1997.
Article no. SS971504

Georgiou, S., Shepherd, A., McMillan, M., Nienow, P. "Seasonal evolution of supraglacial lake volume from ASTER imagery." *Annals of Glaciology*, Vol. 50, No. 52, pp. 95-100, October 2009.

Greuell, W., de Ruyter de Wildt, M. "Anisotropic Reflection by Melting Glacier Ice: Measurements and Parametrizations in Landsat TM Bands 2 and 4." *Remote Sensing of the Environment*, Vol. 70, pp. 265-277, December 1999.

Landsat data available from the U.S. Geological Survey.

Lyzenga, David R. "Passive remote sensing techniques for mapping water depth and bottom features." *Applied Optics*, Vol. 17, No. 3, pp. 379-383, 1 February 1978.

McMillan, M., Nienow, P., Shepherd, A., Benham, T., Sole, A. "Seasonal evolution of supra-glacial lakes on the Greenland Ice Sheet." *Earth and Planetary Science Letters*, Vol. 262, No. 3-4, pp. 484-492, 30 Oct. 2007.

Meeus, Jean. *Astronomical Formulae for Calculators*, 2nd ed. Willmann-Bell, Inc., Richmond, Virginia, 1982.

NASA: Landsat 7 Science Data Users Handbook [online reference]. 12 March 2009. URL: http://landsathandbook.gsfc.nasa. gov/handbook/handbook_toc.html [cited: 29 November 2010].

Nishii, R. and Eguchi, S. "Supervised Image Classification of Multi-Spectral Images Based on Statistical Machine Learning." *Image Processing for Remote Sensing*, edited by C.H. Chen. Taylor & Francis Group, Boca Raton, FL, pp. 79-105, 2008.

Painter, T.H., Dozier, J. "Measurements of the hemispherical-directional reflectance of snow at fine spectral and angular resolution." *Journal of Geophysical Research*, Vol. 109, No. D18, pp. 27, 27 September 2004
doi:10.1029.

Perovich, D.K., Tucker III, W.B., and Ligett, K.A. "Aerial observations of the evolution of ice surface conditions during summer." *Journal of Geophysical Research*, Vol. 107, No. C10, 26 October 2002
doi: 10.1029

Petty, G.W. *A First Course in Atmospheric Radiation*, 2nd Ed. United States of America, 2006.

Richards, J.A., Jia, X. *Remote Sensing Digital Image Analysis An Introduction*, 4th ed. Springer-Verlage Berlin Heidelberg, Germany, chap. 8, 2006.

Satterwhite, M.B., Mitchell, H., Hemmer, T., Leckie, J.D. "Field Spectral Signatures of Snow, Ice, and Water." *Proceedings of the SPIE-The International Society for Optical Engineering*, Vol. 5093, No. 1, pp. 528-537, 2003.

Scaramuzza, P.L., Markham, B.L., Barsi, J.A., Kaita, E. "Landsat-7 ETM+ On-Orbit Reflective-Band Radiometric Characterization." *IEEE Transactions on Geoscience and Remote Sensing,* Vol. 42, No. 12, December 2004.

Sinnott, R.W. "Virtues of the Haversine." *Sky and Telescope,* Vol. 68, No. 2, pp. 159, 1984.

Smith, R.C., and Baker, K.S. "Optical properties of the clearest natural waters (200-800 nm)." *Applied Optics*, Vol. 20, No. 2, pp. 177-184, 15 January 1981.

Sneed, W.A., and Hamilton, G.S. "Evolution of melt pond volume on the surface of the Greenland Ice Sheet." *Geophysical Research Letters*, Vol. 34, No. 3, pp. 1-4, 16 February 2007.

"Solar Calculation Details." *Earth System Research Laboratory Global Monitoring Division* [online resource]. URL: http://www.esrl.noaa.gov/gmd/grad/solcalc/calcdetails.html [cited: 26 January 2011]

Stroeve, J., Nolin, A., Steffen, K. "Comparison of AVHRR-Derived and In Situ Surface Albedo over the Greenland Ice Sheet." *Remote Sensing of the Environment*, Vol. 62, pp. 262-276, December 1997.

Sundal, A.V., Shepherd, A., Nienow, P., Hanna, E., Palmer, S., Huybrechts, P. "Evolution of supra-glacial lakes across the Greenland Ice Sheet." *Remote Sensing of Environment*, Vol. 113, No. 10, pp. 2164-2171, 30 October 2007.

Tou, J.T., and Gonzalez, R.C. *Pattern Recognition Principles*. Addison-Wesley Publishing Company, Inc., United States of America, 1974.

Zwally, H.J., Abdalati, W., Herring, T., Larson, K., Saba, J., and Steffen, K. "Surface Melt-Induced Acceleration of Greenland Ice-Sheet Flow." *Science*, Vol. 297, pp. 218-222, 12 July 2002.

VIII. Appendix

a. Nomenclature

a	=	Absorption coefficient	(unitless)
b	=	Backscatter coefficient	(unitless)
$\hat{b}$	=	Aircraft body frame	(unitless)
c_p	=	Specific heat capacity	(J/g/K)
D	=	Distance	(m)
d	=	Thickness	(m)
f	=	Slant angle correction	(unitless)
g	=	Acceleration due to gravity	(m/s^2)
g_j	=	Discriminant function	(unitless)
I	=	Irradiance	(W/m^2)
k	=	Radiative transfer constant	(W/m^2)
m	=	Ratio of indices of refraction	(unitless)
m_j	=	Average of data in class j	(unitless)
N	=	Real index of refraction	(unitless)
n_i	=	Imaginary index of refraction	(unitless)
$p()$	=	Probability of belonging to a data class	(unitless)
R_E	=	Radius of earth	(m)
r	=	Reflectivity	(unitless)
s	=	Path length	(m)
sza	=	Solar zenith angle	(degrees)

t	=	Transmittance	(unitless)
X’	=	Resolution of ground pixel	(m)
x	=	Depth	(m)
$\vec{x}$	=	Spectral data	(unitless)
$\vec{z}$	=	Slant direction to ground pixel	(unitless)
α	=	Surface slope angle	(degrees)
β	=	Total absorption coefficient	(m^{-1})
γ	=	Longitude	(degrees)
ΔH_{fus}	=	Heat of fusion	(kJ/kg)
ΔT	=	Change in temperature	(K)
Δt	=	Change in time	(seconds)
δ	=	Angle of ground pixel	(degrees)
λ	=	Wavelength	(nm, m)
ρ	=	Density	(g/m^3)
Σ_j	=	Covariance matrix	(unitless)
θ	=	Pitch angle	(degrees)
θ_o	=	Angle of incidence	(degrees)
θ_r	=	Angular resolution	(degrees)
θ_t	=	Angle of transmittance	(degrees)
τ	=	Shear Stress	(kPa)
φ	=	Roll angle	(degrees)
ψ	=	Latitude	(degrees)

ω_j	=	Data class	(unitless)

Subscripts

a	=	Absorbed
i	=	Ice
j	=	Data class
l	=	Lake bottom
o	=	Incident
s	=	Optically deep
w	=	Water
1	=	Irradiance subscript, medium, band, location
2	=	Irradiance subscript, medium, band, location
3	=	Irradiance subscript
↑	=	Upwelling
↓	=	Downwelling

b. MUSCOX Data Information

Table 24: MUSCOX data sets.

Data Set	Start Date and Time (GMT)	Duration (sec)	Target	Center Location	Nadir Spatial Resolution (cm)
1	7/9/08 00:03:54.24	9.55	Runway	69°14’33.66” N 51°3’30.05” W	6.06
2	7/9/08 00:05:39.24	10.68	Runway	69°14’33.39” N 51°3’30.29” W	6.06
3	7/9/08 00:07:24.25	9.55	Runway	69°14’33.37” N 51°3’30.73” W	6.06
4	7/9/08 00:09:09.24	11.01	Runway	69°14’32.98” N 51°3’31.02” W	6.06
5	7/9/08 00:10:51.24	13.49	Runway	69°14’35.14” N 51°3’40.10” W	4.48
6	7/16/08 01:08:06.49	4.96	Outflow Region	69°9’31.67” N 50°51’20.16” W	10.08
7	7/16/08 01:16:12.49	5.94	Outflow Region	69°9’31.91” N 50°51’20.06” W	10.08
8	7/17/08 02:56:26.44	123.11	Drained Lake 1	68°44’49.11” N 49°31’43.72” W	29.2642
9	7/17/08 03:09:11.44	37.00	Filled Lake	68°43’6.90” N 49°2’3.68” W	32.75
10	7/17/08 03:11:29.44	140.13	Filled Lake	68°42’29.33” N 49°1’21.61” W	32.75
11	7/18/08 01:41:19.49	62.05	Filled Lake	68°42’35.54” N 49°1’31.00” W	32.75
12	7/18/08 02:22:49.49	3.95	Drained Lake 1	68°45’7.50” N 49°30’59.68” W	29.26
13	7/18/08 02:24:40.50	2.94	Drained Lake 2	68°43’28.84” N 49°30’59.99” W	29.26
14	7/18/08 02:33:44.21	7.93	Drained Lake 2	68°43’42.20” N 49°31’57.43” W	Unknown
15	7/18/08 02:34:05.28	6.95	Drained Lake 2	68°43’24.15” N 49°31’57.11” W	Unknown
16	7/19/08 02:04:38.04	62.04	Filled Lake	68°42’35.33” N 49°1’31.36” W	32.75
17	7/19/08 02:08:02.04	65.05	Filled Lake	68°42’29.47” N 49°1’57.45” W	32.75
18	7/19/08 02:56:38.04	22.99	Drained Lake 2	68°42’59.71” N 49°30’13.49” W	29.26

Table 24 continued: MUSCOX data sets.

Data Set	Start Date and Time (GMT)	Duration (sec)	Target	Center Location	Nadir Spatial Resolution (cm)
19	7/19/08 02:59:50.04	24.00	Drained Lake 2	68°43’20.46” N 49°30’1.00” W	29.26
20	7/19/08 03:02:47.04	22.99	Drained Lake 2	68°43’39.68” N 49°30’14.26” W	29.27
21	7/19/08 03:08:56.04	22.99	Between Drained Lakes	68°44’19.68” N 49°30’16.12” W	29.26
22	7/19/08 03:12:05.05	23.97	Between Drained Lakes	68°44’49.50” N 49°30’2.56” W	29.26
23	7/19/08 03:15:05.05	23.97	Drained Lake 1	68°44’59.69” N 49°30’16.87” W	29.26
24	7/19/08 04:25:38.09	9.65	Runway	69°14’41.97” N 51°3’45.48” W	7.75
25	7/19/08 04:26:32.09	18.63	Runway	69°14’26.21” N 51°3’45.46” W	7.66
26	7/19/08 04:28:20.09	15.09	Runway	69°14’28.77” N 51°3’39.37” W	7.67

Table 25: MUSCOX channels.

Band	Central Wavelength (nm)	Band	Central Wavelength (nm)	Band	Central Wavelength (nm)
1	401.21	21	593.21	41	785.21
2	410.81	22	602.81	42	794.81
3	420.41	23	612.41	43	804.41
4	430.01	24	622.01	44	814.01
5	439.61	25	631.61	45	823.61
6	449.21	26	641.21	46	833.21
7	458.81	27	650.81	47	842.81
8	468.41	28	660.41	48	852.41
9	478.01	29	670.01	49	862.01
10	487.61	30	679.61	50	871.61
11	497.21	31	689.21	51	881.21
12	506.81	32	698.81	52	890.81
13	516.41	33	708.41	53	900.41
14	526.01	34	718.01	54	910.01
15	535.61	35	727.61	55	919.61
16	545.21	36	737.21	56	929.21
17	554.81	37	746.81	57	938.81
18	564.41	38	756.41	58	948.41
19	574.01	39	766.01	59	958.01
20	583.61	40	775.61	60	967.61